Analysis of Sunyaev-Zel'dovich Decrements

Rhiju Das

Astrophysics Group, Cavendish Laboratory, Madingley Road, Cambridge CB3 0HE
and
Trinity College, Cambridge

A thesis submitted for the degree of Master of Philosophy in the University of Cambridge

August 30, 1999

PREFACE

This thesis is the result of work undertaken in the Astrophysics Group at the Cavendish Laboratory between October 1998 and August 1999, and includes nothing which is the outcome of work done in collaboration. It has not, nor has any similar thesis, been submitted for a degree, diploma or other qualification at this, or any other, university. This thesis does not exceed 15,000 words in length, exclusive of tables, captions, bibliography, and footnotes.

CONTENTS

ABSTRACT

The Sunyaev–Zel'dovich (S–Z) shadows of twenty galaxy clusters have been imaged by creating and by applying a new, systematic method to fit and to remove radio sources from Ryle Telescope (RT) data. The radio source environment is found to be complex, with 4 to 6 times as many point sources in these rich cluster regions than are found in non-cluster space. In addition, most of the hot, dynamic clusters studied here are found to have extended radio sources near the cluster centre, which may be gravitationally-lensed radio rings, merger-induced radio halos, "mini-halos" associated with cluster gas cooling flows, or combinations of these phenomena. A method to separate this extended flux from the S–Z shadow is applied to eight clusters, with z ranging from 0.14 to 0.55. The resulting images are combined with X-ray measurements of the cluster gas to obtain a value of the Hubble constant: H_0 = 56–72 $\mathrm{km\,s^{-1}Mpc^{-1}}$, with the range reflecting systematic uncertainties in modelling the gas temperatures of these dynamic clusters, plus a further statistical error of 11%. Finally, recent searches by the RT of S–Z effects from high-redshift clusters are summarized. These include the discovery of two new clusters, TEXOXL20 and TEXOXL21, associated with aggregates of radio sources, as well as possible evidence for extended super-structure in the S–Z images of CL0016+16 and MS1137+6625, which appear only as faint, round sources in X-ray maps.

1. INTRODUCTION

1.1 The Sunyaev-Zel'dovich Effect: The Shadows of Galaxy Clusters

Galactic clusters are the largest gravitationally-bound structures in the universe, with the richest containing thousands of galaxies spread over several millions of light years. Surprisingly, the galaxies themselves comprise only around 5% of each cluster's mass, which totals 10^{15} solar masses in the biggest clusters. Another 10% of the mass takes the form of a plasma spread throughout the cluster, with maximum densities of several thousand particles per cubic metre. See, e.g., the lectures in [Minnesota 1988] and the catalogues of Abell and Zwicky [Abell 1989] [Zwicky 1961]. This hot gas gains its temperature — up to 10^8 K — by falling into the cluster's gravitational potential well, and is visible by the X-rays it produces as thermal bremsstrahlung; see, e.g., [Sarazin 1986]. The vast majority of a cluster's mass is in the form of inert, mysterious dark matter, which makes its presence known by providing a gravitational potential that binds the cluster and lenses the light of background galaxies. See, e.g., [Turner & Tyson 1999] and [White 1993].

The physics of the megaparsec length scales and the billion-year time scales that characterize a cluster's life can be dynamic. On one hand, many hot clusters are the result of recent or on-going mergers, processes in which large clusters engulf other ones, often producing shocks and strong magnetic fields that can accelerate particles in the intra-cluster plasma; see, e.g., [Tribble 1993]. On the other hand, "relaxed" (non-merging) clusters also contain interesting dynamics, including cooling flows, where the dense centre of the intra-cluster gas is compressed inwards as it gets quickly cooled by X-ray emission [Fabian 1994].

The thermal Sunyaev-Zel'dovich (S–Z) effect, proposed in the early 1970s [Sunyaev & Zel'dovich 1972], is an unique method for looking at galactic clusters. Rather than relying on the cluster's own radiation, one looks for the cluster's effect on a primal light source, the 2.7 K cosmic microwave background (CMB) left over from the early universe. Electrons in a hot cluster's plasma inverse-Compton-scatter CMB photons up to higher energy, causing a depletion in the CMB intensity at radio frequencies lower than 200 GHz, as shown in Figure 1.1. In the low-frequency (Rayleigh–Jeans) region, the temperature decrement of this "shadow", or "hole", is proportional to the effective number of electron scatterers along the line-of-sight, given by the electron density n_e times the Thompson cross section ($\sigma_T = 0.665 \times 10^{-28}\,\mathrm{m}^2$) for electron-photon scattering, integrated along the line-of-sight, as well as to the fractional kinetic energy available per scatterer, proportional to the temperature $k_\mathrm{B}T_e$ over the

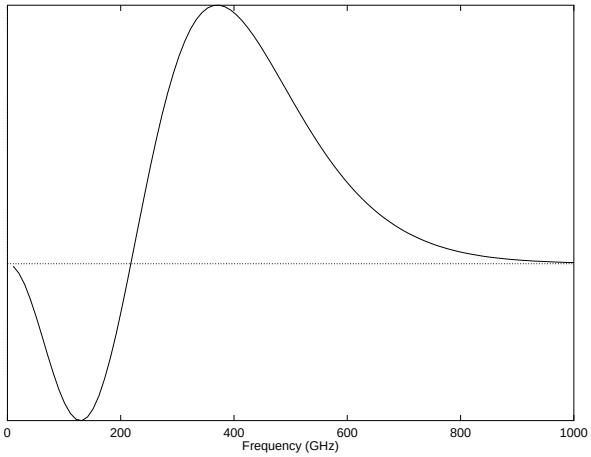

Fig. 1.1: The S–Z effect as a function of radio frequency. The *y*-axis shows the S–Z surface brightness in arbitrary units, and is dependent on the properties of the galaxy cluster; figure is from [Grainge 1996]. At the Ryle Telescope's observing frequency, 15 GHz, the surface brightness is expected to be negative, approximately $-1\,\mathrm{mJy\,arcminute}^{-2}$ for a rich cluster.

rest energy $m_e c^2$:

$$\Delta T_{SZ}/T_{CMB} = -\frac{2k_{\mathrm{B}}\sigma_T}{m_e c^2}.\int n_e T_e\, dl, \tag{1.1}$$

For a rich cluster with $T_e = 10^8\,\mathrm{K}$, $n_e = 10^4\,\mathrm{m}^{-3}$, and a diameter of a few hundred kiloparsecs, the S–Z effect is small, $\Delta T_{SZ} \approx 1\,\mathrm{mK}$, corresponding to a fractional change $\Delta T_{SZ}/T_{CMB}$ in the CMB intensity of a little over 10^{-4}, but it is an order of magnitude larger than any other possible effects producing arcminute-scale negative features in the CMB, such as intrinsic primordial anisotropies. See [Birkinshaw 1998] for a full review of other effects producing holes. Despite its small magnitude, successful measurements of S–Z distortions have been made with a wide variety of telescopes since the first 1–dimensional radiometer scans through the cluster Abell 2218 in the mid-1980s [Uson 1984] [Birkinshaw 1984]. The first 2–dimensional image of a cluster's S–Z effect was obtained for Abell 2218 in 1993 by the Ryle Telescope (RT) at the Cavendish [Jones 1993]. Imaging of such S–Z effects with the Ryle Telescope and the OVRO/BIMA arrays is now routine; see recent measurements reported in [Grainge 1999], [Saunders 1999], and [Carlstrom 1999].

Perhaps the most remarkable thing about the S–Z effect is implicit in equation (1.1) — the observed temperature decrement is independent of the cluster's redshift. An Earth-bound telescope sees a far-away light-emitting object as having an effective temperature (proportional to the surface brightness, as well as the energy density, of the detected photons) that is smaller than the emitted temperature by a factor $(1+z)^{-4}$, where z is the redshift, due to the effects of the universe's expansion on the photon energy and arrival frequency, and on the object's apparent angular scale. The S–Z effect, however, gets around this inherent limitation: the energy density of the illuminating CMB photon source is larger in the past, by a perfectly compensating factor $(1+z)^4$. Measurements of the S–Z effect promises to be a powerful probe of the large-scale structure of the high-redshift universe; in

particular, they will strongly constrain the rate of galaxy (proto)cluster formation, which is highly sensitive to cosmological parameters like the universe's mass density Ω_m [Bahcall 1997].

Quantitatively, a Rayleigh-Jones temperature deficit of $-1\,\mathrm{mK}$ corresponds to a surface brightness of about $-1\,\mathrm{mJy\,arcminute^{-2}}$, using the formula

$$\mathrm{Surface\,brightness} \equiv \frac{2k_\mathrm{B}T_{\mathrm{R-J}}}{\lambda^2}. \tag{1.2}$$

Clusters beyond $z = 0.2$ have apparent sizes of a few arcminutes, and thus produce holes with total negative flux on the order of $-10\,\mathrm{mJy}$.[1] Thus, unlike searches for optical/X-ray/radio *emission* of distant clusters, looking for S–Z *shadows* of clusters is just as easy at $z = 5$ — if rich clusters exist that far in the past — as it is at $z < 0.5$. One purpose of this thesis is to summarize recent discoveries by the Ryle Telescope of high-redshift (proto)clusters.

The main objective of this thesis is to illustrate a fast, systematic way in which contaminating radio sources can be removed from S–Z maps. The resulting images, when combined with X-ray information, can then yield a measurement of the Hubble constant H_0, the current rate of expansion of the universe [Cavaliere 1979]. The idea is simple: a cluster's X-ray luminosity L_X is proportional to $\int n_e^2 T_e^{1/2} dl$, while the depth of its S–Z hole ΔT_SZ is proportional to $\int n_e T_e dl$. Constraining the electron gas temperature from X-ray spectra, and guessing a 3-D model of the gas shape, one can then estimate the length through the cluster, proportional to $\Delta T_\mathrm{SZ}^2 / L_\mathrm{X}$. Comparing this length to the cluster's angular size yields the angular-size distance to the cluster. This then calibrates the universe's angular-size distance vs. redshift curve, giving the value of H_0. The main advantage of this technique is its independence of the assumptions used to calibrate the cosmological distance-ladder, which have prompted quite a bit of controversy over discrepancies between various recent H_0 measurements. These measurements ranged from $50\,\mathrm{km\,s^{-1}Mpc^{-1}}$ up to $80\,\mathrm{km\,s^{-1}Mpc^{-1}}$ as recently as two years ago, but now appear to be converging towards a tighter range of values, $65 - 75\,\mathrm{km\,s^{-1}Mpc^{-1}}$, as systematic errors in the different experiments are better understood; see, e.g., [Freedman 1999].

The S–Z/X-ray method to determine H_0 is subject in practice to random and systematic errors, with the largest ones being the mismatch between the cluster gas temperature appropriate to the S–Z effect and that actually measured in X-ray observations, assumptions about the shape of the gas, and effects of the contaminating radio sources near the cluster; see, e.g., [Grainge 1999]. The work presented in this thesis details a complete method to deal not only with point-like radio sources but also with extended cluster centre "halos" that obscure the Sunyaev-Zel'dovich shadow. This method is applied to the Ryle Telescope's observations to produce images of the S–Z holes of twenty clusters. Eight of the S–Z detections are then combined with X-ray information to yield an estimate of H_0.

[1] Naively, one might expect that more distant clusters would appear smaller in the sky, in inverse proportion to their distance/redshift, so that their total flux would be reduced dramatically with distance, as $1/\mathrm{distance}^2$. However, due to the universe's expansion, the angular diameter of an object is given by $D_\theta = z(1+z)^{-2}H_0^{-1} \approx 1\mathrm{Mpc\,arcminute^{-1}z}(1+\mathrm{z})^{-2}$, up to corrections of order $q_0 z^2$ [Weinberg 1972]. Because of the $(1+z)^{-2}$ factor, the angular-distance flattens to a maximum of approximately $300\mathrm{kpcarcminute}^{-1}$ at $z = 1.25$ for $q_0 = \frac{1}{2}$ and $\Lambda = 0$, instead of increasing indefinitely with redshift.

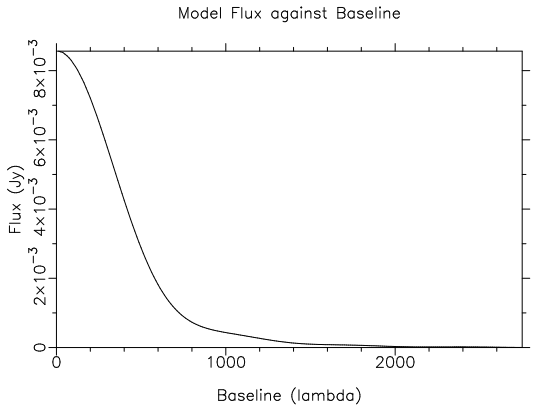

Fig. 1.2: Absolute value of simulated S–Z flux as a function of interferometer baseline for rich cluster Abell 2218; figure is from [Grainge 1996]. Note that the RT's shortest baseline is 900λ, just short enough to catch 10% of the flux.

1.2 Radio Interferometry, and the Ryle Telescope

The technique of aperture-synthesis radio interferometry, developed at the Cavendish Laboratory by Ryle [Ryle 1972], allows the imaging of a wide variety of angular scales of the radio sky. An interferometer consists of a number of radio aerial dishes tracking a particular region of the sky. Each pair of dishes constitutes a single interferometer "baseline"; the outputs of each receiver in a pair are correlated, directly measuring a particular spatial Fourier component of the radio intensity $S(\mathbf{x})$) of the sky, a complex *visibility*:

$$\mathrm{Vis}(\mathbf{u}) = \int \mathrm{e}^{\mathrm{i}2\pi\mathbf{u}\cdot\mathbf{x}} \mathrm{S}(\mathbf{x})\,\mathrm{B}(\mathbf{x})\,\mathrm{d}^2\mathbf{x}, \tag{1.3}$$

where $\mathbf{u} = (u, v)$ is the baseline, the separation vector between two aerials measured in radio wavelengths (λ) projected onto the sky; $\mathbf{x}$ are the coordinates of the sky, measured in radians; and $B(\mathbf{x})$ is the primary beam pattern, an envelope function determining the telescope's field-of-view, whose location on the sky is set by the aerials' pointing direction. Because the interferometer measures the correlated power of particular Fourier components of patches of the sky (and not the total power), it avoids several systematic errors of single-dish radio experiments. In particular, the interferometer "resolves" out the constant 2.7 K cosmic background, as well as any atmospheric emission (which is at large angular scales), and thus measures only anisotropies in the CMB selected out by the Fourier components corresponding to the interferometer baselines. In addition, the celestial radio emission of interest moves across the sky, producing a tell-tale time variation, the "fringe rate", in the correlated input. Filtering for this fringe rate allows for additional suppression of any background radio noise — such as interference — not intrinsic to the aerial receivers themselves; see, e.g., [Thomson 1986].

The S–Z shadows of galactic clusters are generally of angular sizes of several arcminutes. The interferometer baselines required to see such features would ideally need to be less than 1 kλ, as can

Configuration	Ae 1	Ae 2	Ae 3	Ae 4	Baselines Available
Ca	12	9	7	4	2,3,3,4,5,5,7,8,9,12
Cb	12	10	8	4	2,2,4,4,4,6,8,8,10,12
Cc	16	12	8	4	4,4,4,4,8,8,8,12,12,16
Cd	32	24	16	10	6,8,8,10,14,16,16,22,24,32

Tab. 1.1: Compact configurations of the Ryle Telescope. RT antennas 1–4 are mounted on an east-west railway track; their positions are listed relative to (fixed) aerial 5, in units of 8.93 m, corresponding to 450λ at 15 GHz.

be seen from the simulated flux vs. baseline of cluster Abell 2218, shown in Figure 1.2. Most of the world's sensitive radio telescopes have been designed with large baselines — from many metres to intercontinental distances — to look at sub-arcsecond structures, like active galactic nuclei, and do not have short enough baselines to see S–Z structures. For example, the shortest baseline available to the Very Large Array (VLA) in New Mexico in its most compact configuration is 33 m, corresponding to about 2 kλ at the 15 GHz; see, e.g., [Partridge 1987].

Currently, the Ryle Telescope, observing at 15 GHz, and the OVRO/BIMA arrays, observing at 30 GHz, are the only interferometers with short enough aerial spacings (1 kλ and 1–2 kλ, respectively) to catch any of the S–Z effect. These baselines are still not ideally short enough, and detect only about 10–20% of the total S–Z flux of typical cluster targets. Designs for interferometers with shorter baselines devoted wholly to detection of the S–Z holes have been proposed, and hopefully will be built within the next few years. Until then, we rely on the Ryle Telescope for images of the S–Z effect.

To search for the S–Z effect, the Cavendish laboratory uses the five closest-spaced aerials of the Ryle Telescope, consisting the original seven 12.8-m Cassegrain-focus paraboloid dishes in Ryle's original 5-km Telescope [Ryle 1972] with an upgraded correlator; four of these aerials are moveable along an east-west railtrack. The RT operating frequency for S–Z searches is 15 GHz; it is a compromise between attempting to reduce contamination of the S–Z effect by radio sources, whose intensities generally fall with frequency [Windhorst 1993], and avoiding strong atmospheric interference, which becomes strong in the rainy Cambridge telescope site at frequencies higher than 20 GHz. The telescope's total bandwidth of 350 MHz is divided up into 5 sub-bands of frequency ± 35 MHz; each sub-band is then divided into a further 7 sub-channels before correlation by an 8-lag Fourier Transform Spectrometer, to prevent chromatic aberration. The cooled receivers operate with a system temperature of 60 K, improved from 75 K after a 1994 upgrade, with some noise variation depending on the atmosphere's radio emission; after 12 hours of observation on a target, combined data from the 10 possible aerial pairings yield a map with an r.m.s. noise of 200 μJy, probing angular scales from a few arcseconds to an arcminute, corresponding to available baselines of 10 kλ down to 1 λ [Grainge 1996]. The primary beam has a full-width-to-half-maximum (FWHM) of 6 arcminutes. Further details of telescope operations and sub-sytems are available in [Jones 1990].

The baselines avaliable to the RT in various aerial configurations are listed in Table 1.1; an example of the *u-v* coverage of the baseline vectors, which sweep out semi-ellipses in the Fourier plane,

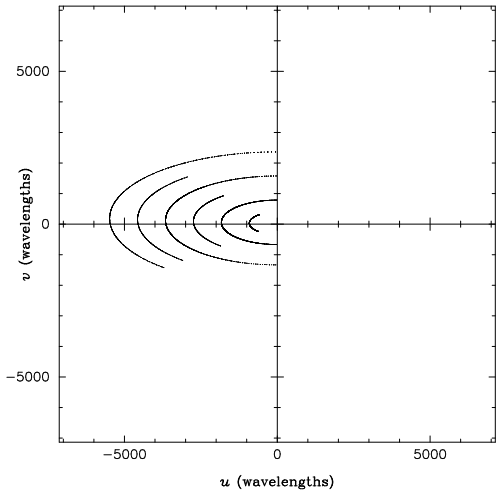

Fig. 1.3: The *u-v* coverage of the aperture plane, or Fourier plane, for observation of the cluster Abell 1413, at declination 23°, by the Ryle Telescope in Cb configuration. The missing portions of the semi-ellipses correspond to aerial pairings where one aerial dish shadows the other dish. Note that the visibilities in the right half of the Fourier plane are constrained by $\mathrm{Vis}(\mathbf{u}) = \mathrm{Vis}^*(-\mathbf{u})$, since the corresponding sky map is purely real.

or aperture plane, relative to the sky as the earth turns, is shown in Figure 1.3. For most cluster observations, the most compact Cb aerial configuration provides the best short-baseline data relevant for the S–Z effect; however, the other configurations are often used for low decrement targets, for which the closely spaced Cb aerials can actually shadow each other for long periods of time.

1.3 The Ryle Telescope S–Z Programme

Because of the faintness of the S–Z effect, it is not yet feasible to survey a large patch of the sky to search for distant galactic clusters; one needs clues as to where to point the Ryle Telescope. The targets of the Ryle Telescope S–Z programme are divided into two categories: medium-redshift clusters at $z \approx 0.2$ which allow the determination of the Hubble constant, and distant, high-redshift candidates at $z > 0.3$. The targets are listed in Table 1.3.

The set of "Hubble constant" clusters were initially selected in 1993 based on approximate depths of the S–Z effects of the rich clusters known then, most of which were compiled in the Abell and Zwicky catalogues. The expected S–Z fluxes were estimated from the X-ray luminosity and redshift information available at that time; clusters with redshifts less than about 0.1 were automatically ruled out because their large angular scales would be resolved out by the RT [Grainge 1996]. Maps of the hundred best cluster candidates were checked in the Green Bank 5 GHz All-Sky survey; regions with bright sources (greater than 20 mJy at 5 GHz) were thrown out. Furthermore, one-day maps of the remaining clusters were made with the RT, and clusters in regions containing sources greater than

5 mJy at 15 GHz were also removed from the target sample. Most candidates in the sample of forty candidates have been observed by the RT in the last six years for periods of time ranging from 6×12 hours for Abell 1246 up to 80×12 hours for both Abell 2218 and CL0016+16. The existence of public-domain X-ray maps, published X-ray temperatures, and sensitive VLA observations at lower frequencies (1.4 GHz, 5 GHz) has allowed for full source-subtraction and for Hubble-constant determination for eight of these clusters, including Abell 665, Abell 1413, and Abell 773. Details on these clusters' S–Z effects are presented in section 3.2.

The possible indicators currently used to look for rich, high-redshift clusters include galactic overdensities in the Hubble Space Telescope Medium Deep Survey; faint but extended X-ray sources; and clusters of bright radio sources. Further details on recent searches for distant clusters are presented in section 3.3.

Cluster Name	z	RA (B1950)	Dec (B1950)
A611	0.288	$07^h57^m43.4^s$	$36°11^m20^s$
A665	0.182	$08^h26^m25.6^s$	$66°01^m09^s$
A697	0.282	$08^h39^m46.4^s$	$36°32^m34^s$
A773	0.217	$09^h14^m22.4^s$	$51°56^m09^s$
A990	0.144	$10^h20^m34.5^s$	$49°23^m31^s$
A1246	0.216	$11^h21^m19.8^s$	$21°45^m37^s$
A1413	0.143	$11^h52^m44.0^s$	$23°41^m10^s$
A1423	0.213	$11^h54^m47.2^s$	$33°53^m38^s$
A1704	0.220	$13^h12^m36.0^s$	$64°50^m28^s$
A1722	0.328	$13^h18^m33.6^s$	$70°17^m38^s$
A1914	0.171	$14^h23^m59.1^s$	$38°02^m57^s$
A1995	0.318	$14^h51^m36.0^s$	$58°15^m05^s$
A2111	0.229	$15^h37^m46.2^s$	$34°34^m39^s$
A2218	0.171	$16^h35^m42.0^s$	$66°18^m47^s$
A2259	0.164	$17^h18^m08.3^s$	$27°43^m10^s$
Zw1883	0.194	$08^h39^m53.9^s$	$29°28^m48^s$
CL0016+16	0.546	$00^h15^m58.4^s$	$16°09^m42^s$
MS1137+662	0.78	$11^h37^m34.7^s$	$66°24^m52^s$
TEXOXL20		$02^h30^m22.8^s$	$30°08^m49^s$
TEXOXL21		$02^h30^m32.1^s$	$35°46^m17^s$

Tab. 1.2: RT Targets for S–Z detections.

2. SEEING THE S–Z EFFECT: METHODOLOGY

The major objective of this research has been to produce a quick, systematic method to remove contaminating radio sources from several years' worth of Ryle Telescope cluster observations allowing the imaging of the remaining S–Z shadows. The following section details a proposed replacement of the previously used methodology, which, being nascent, was labour-intensive and sometimes lacking in desired rigour [Grainge 1996].

2.1 Initial Steps

Because the S–Z decrements are faint, the RT has to be pointed at a particular cluster for a couple weeks (sometimes, for a couple months), producing a large amount of data. Each day's observations are filtered to throw away visibilities affected by dish shadowing or by weather, and are calibrated. The resulting data are outputted in the compact Flexible Image Transport System (FITS) format [Pooley 1999].

To make the data more amenable to FORTRAN manipulations, each FITS file is then converted to the simple *vis* format, a text file listing, for each 320–second packet of time and for each aerial pairing, the (u,v) baseline, the real and imaginary part of the visibility, and the estimated noise on the observation, usually about 7 mJy. Previously, the noise estimate was taken by re-weighting a nominal error based on a noise-injection estimator ("rain gauge") indicating the effect of weather on the telescope; this often underestimated errors by a factor of 1.5 to 2. Now, a better estimate for the r.m.s. error on each visibility is determined by looking at the intrinsic scatter of the 35 sub-frequency measurements that were combined into one visibility. The switch to the latter method does not affect the basic numbers and images in the data; it only improves the estimates of the error bars.

The one-day visibility files for a given cluster are then concatenated into one big *vis* file, whose contents are binned by cutting out $200\,\mathrm{k}\lambda$ square bins in the *u*-*v* plane, and by then averaging the data (weighted by $1/\mathrm{r.m.s.}^2$) in each of the square bins. The new binned *vis* file, called a *vbn* file, contains, for each non-empty bin of the *u*-*v* plane, the (u,v) of the weighted bin centre, and the appropriately combined visibility and r.m.s.. The big advantage of binning is the much improved speed at which sources in the data can be properly fitted. Of course, the averaging in the *u*-*v* plane throws away phase information relevant to sources greater than 10 arcmin from the RT pointing centre; however, the RT primary beam (whose first null occurs at 5 arcminutes from the centre) prevents anything that far

away from showing up in the observation.[1] Finally subtraction of contaminating radio point sources is carried out, and the resulting short-baseline decrements are analyzed; this general methodology is detailed below.

Although all the quantitative analysis is carried about by a fitting program, maps of the data are made as visual aids. A Fast Fourier Transform is applied to the interferometer visibilities to get an approximation to the actual radio sky; since the data do not have information about the full *u-v* (Fourier) plane, the resulting image is of the sky convolved with a synthesized beam pattern, i.e. sources are accompanied by "grating rings" that dirty up the map (see, e.g., Figure 2.1a). Previous analyses have usually extracted results on the sources as well as the S–Z decrement by using the nonlinear CLEAN algorithm to deconvolve the image, implemented as the APCLEAN task in the NRAO Astronomical Image Processing System (AIPS) package [AIPS 1999]. CLEANing, however, can sometimes produce spurious results if applied to maps based on visibility data with either sparse *u-v* coverage (especially on shortest baselines) or low signal-to-noise — the RT short-baseline S–Z data have both problems. In this thesis, CLEANed images of S–Z effects are shown for aesthetic pleasure, but all shapes, positions, and numbers relevant to the analysis are taken from fitting the *vis* files, with the *dirty* maps as visual guides.

2.2 Subtracton of Point Sources

For each pointing, there are usually two to six "bright" radio sources within the RT field-of-view, whose fluxes, ranging from 150 to 1500 μJy, contaminate the maps. Physically, these may be quasars or other active galactic nuclei, or star-forming galaxies, whose structures are generally smaller than a few arcseconds, and therefore appear point-like in current RT observations. Many are variable on timescales of days or months, but this does not affect RT data which has been averaged over the observing time.

Most other S–Z experiments attempt to subtract sources based on extrapolation of lower-frequency fluxes, taken from, e.g., VLA data. The great advantage of the Ryle Telescope is that its longer baselines, on which the S–Z effect is absent, can expose the locations and fluxes of contaminating radio sources, allowing for their removal from the shorter baselines. Because the shorter baseline data and longer baseline data are taken simultaneously, the RT source subtraction is not subject to the spectral and temporal uncertainties that plague other experiments. Indeed, the source subtraction does not significantly increase the short-baseline r.m.s. noise estimates in the *vis* files, since the errors on the source fluxes are generally less than half of the error on the S–Z decrements — the Ryle Telescope has roughly four times as many longer baselines($> 2\,\mathrm{k}\lambda$) as shorter baselines ($< 1\,\mathrm{k}\lambda$).

The source removal takes two steps: subtraction of the majority of the point source flux, followed by removal of any residual extended emission. As an example of a target requiring source subtraction,

[1] The Ryle Telescope has encountered one exception to this: the cluster MS1137+6625 (see following chapter) which is contaminated by a very bright 3C source 20 arcmin away from the centre; to analyze that cluster, the *u-v* bin sizes are reduced to $20\,\lambda$.

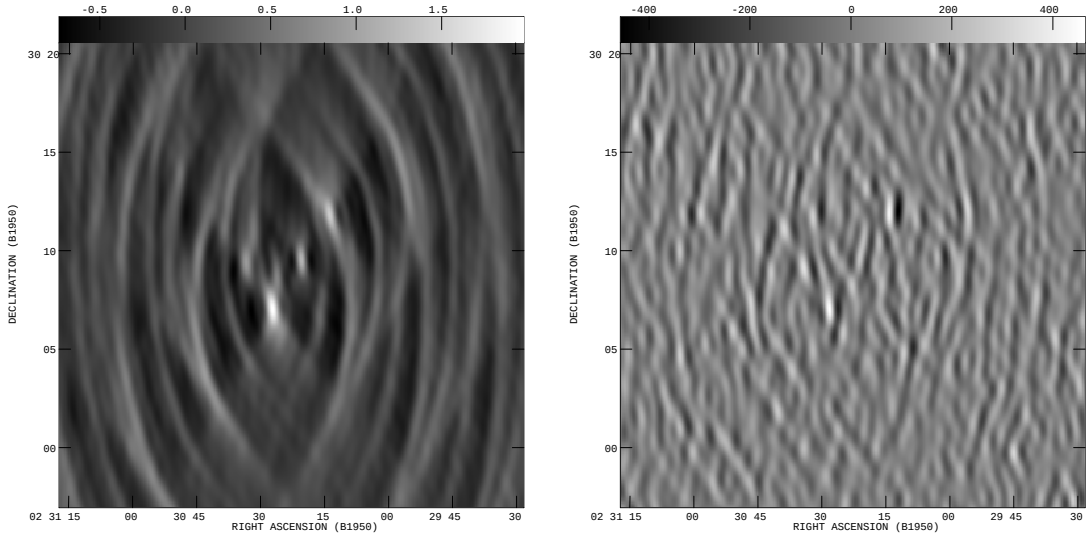

(a) (b)

Fig. 2.1: Demonstration of source subtraction for the TEXOXL20 region. (a) Map (not CLEANed) of all RT baselines showing several point sources in the field-of-view. (b) Long baseline ($> 2\,\mathrm{k}\lambda$) map after inital removal of NVSS-selected point sources, showing "residual" point sources.

Figure 2.1a shows the raw RT map, using all baseline information, of candidate high-z cluster region TEXOXL20. To find out if there really is a cluster there with accompanying S–Z shadow, one needs to remove the effects of the sources.

2.2.1 First Round of Subtraction: Points

I have written a program, called FLUXFITTER, to create a set of model visibilities of the radio sky, and compare it to the actual data by computing the χ^2 statistic for how well the model fits the data visibilities, given the errors expected for the visibilities σ_{Vis}:

$$\chi^2 \equiv \sum_{\text{visibilities}} \frac{\left|\mathrm{Vis}_{\mathrm{data}} - \mathrm{Vis}_{\mathrm{model}}\right|^2}{\sigma^2_{\mathrm{Vis}}}, \tag{2.1}$$

For data with Gaussian noise (as is the case for the interferometer visibilities), the χ^2 is equivalent to $-2\log(\mathrm{likelihood})$, up to an additive constant; thus, finding a model with minimum χ^2 is equivalent to maximizing the likelihood of the fit. If the model visibilities are parametrized by, for example, a set of fluxes and/or positions, the standard error, or 1–σ error, ellipsoid is then defined by those parameter values $\chi^2_{1-\sigma}$ which satisfy $\chi^2_{1-\sigma} = \chi^2_{\mathrm{min}} + 1$. In practice, the 1–$\sigma$ errors are estimated by finding how the χ^2 increases as each of the parameters is separately varied around the minimum, and then extrapolating to where χ^2 is expected to go up by 1.

First, a list of source candidates (usually 5 to 10 sources within 8 arcminutes of the RT pointing centre) is compiled from lower-frequency catalogues, like the VLA FIRST [White 1997] and VLA

NVSS surveys [Condon 1998] at 1.4 GHz, the WENSS survey at 330 MHz [Rengelink 1997], and in special cases, deep VLA images of the cluster region that have been obtained by the Cavendish group or others, e.g., [Moffet & Birkinshaw 1989]. These possible source locations are then fed into FLUXFITTER, which uses a simplex-minimization "amoeba" routine to find a best fit of point source fluxes at those locations in the RT data. The minimization routine is a straight-forward one, first setting up a polyhedron, or simplex, in the fit-parameter space and then allowing it to move around parameter space (via contractions, expansions, and inversions through one vertex) and to contract onto a global minimum of the χ^2; see [Num. Recipes 1992] for details. The minimization routine generally takes less than ten seconds to fit the fluxes; initial guesses for the fluxes are set to zero, to avoid sign bias. The χ^2 is computed using baselines 2–10 kλ; this avoids bias from the cluster's S–Z hole, which produces less than 10 μJy on those baselines (as is clear from Figure 1.2), which is far less than than the r.m.s. noise of 50–150 μJy typical of those baselines in the RT observations. Note that, because the fit is being done with all points simultaneously with *u-v* plane data, there is no need to further compensate for grating rings or sidelobesof the synthesized beam.

Initially, to prevent the routine from getting trapped in local minima of χ^2, the routine was run twice, using the best-fit of the first run (initialized with flux guesses of zero) as an initial guess of the second run. In all cases, the second run has been found to be unnecessary: the χ^2 statistic, taken as a function of the point source fluxes, has a well-defined minimum. The 1-σ errors predicted from the χ^2 analysis for each point source flux are checked to agree with each other and with the r.m.s. noise on (pre-CLEANed) maps made with the source-subtracted long baselines, which typically ranges from 40 μJy for a cluster observation with a large amount of data, like Abell 2218 with 80×12 hours, up to 120 μJy for shorter integrated observation times of 6×12 hours.

Most of the source candidates, taken from lower-frequency catalogues, have fitted fluxes which are of less than 2σ significance (usually corresponding to 200 μJy) in the RT data. This is expected, since candidate sources located more than a few arcminutes from the RT pointing centre will be attenuated by the RT primary beam, which has a half-power radius of 3 arcminutes. These "insignificant" source candidates are discarded. No attempt is made to subtract fluxes from their locations, though, even if some flux was removed, it would only slightly increase the noise to the data. In the dozens of clusters to which this method has been applied, never has a negative fitted flux had greater than 2σ significance — a good systematic check.

The locations of the remaining significant sources are then inputted again into FLUXFITTER; the resulting fluxes/errors are noted, and the sources are subtracted from the data visibilities. Typically, this re-fitting without the "insignificant" sources changes the fluxes by much less than the estimated 1-σ errors. In the particular case of TEXOXL20, the locations of seven point source candidates are taken from the VLA NVSS catalog, which has a flux limit of 2.5 mJy at 1.4 GHz; all of the candidates turn out to produce significant fluxes, ranging from 300 μJy up to 1800 μJy, in the RT field-of-view at 15 GHz. The map with these sources removed is shown in Figure 2.1b; source information is compiled in Table 3.4.

2.2.2 Second Round of Subtraction: Treatment of Residuals, Including Double Sources and Slightly Extended Sources

Occasionally, after the removal of point sources, especially of very bright ones, residual flux is left behind, either because an originally subtracted point source is slightly extended, or because the source candidate which appears in a lower-resolution lower-frequency catalog as one large source is resolved by the Ryle Telescope into two point sources.

To remove these residuals, both the locations and fluxes are fitted by FLUXFITTER, and subtracted, leading to an artefact-free long baseline map. In the TEXOXL20 data, this second round of subtraction removes four residual point sources with fluxes of 200–440 μJy, which are quite significant; the long baseline r.m.s. is 65 μJy. The removal of the residuals produces a long baseline map, Figure 2.2a, with peaks of $\pm 2.5\sigma$, consistent with noise. All four residual points are close (within 100 arcsec, and in two cases, within 20 asec) to point sources removed in the first round of subtraction; the NVSS map, which has a poor resolution (synthesized beam of FWHM 45 arcsec), shows them as "extensions" of the stronger sources. Note that when deeper VLA images are available, as is the case for the H_0 clusters presented in this thesis, all subtracted sources and residuals have clearly identifiable counterparts in the lower frequency maps.

In a few rare cases, including Abell 665 and CL0016+16, a bright source appears extended because it lies near the null of the primary beam, becoming highly susceptible to slight fluctuations in the telescope pointing. These apparently extended sources have caused problems in previous CLEAN-based analyses. But, by fitting for both the location and flux in FLUXFITTER, they are easily removed.

In all the clusters studied, the above methodology has yielded a long baseline ($> 2\,k\lambda$) map consistent with noise. In addition, several of the RT full cluster data sets, including the large sets for Abell 665, Abell 2218, and CL0016+16, have been previously analyzed by Grainge and Jones using a more labour-intensive CLEAN-based analysis [Grainge 1996] [Jones 1993]. The point source fluxes predicted by the current FLUXFITTER code agree well within 1-σ error bars with the results obtained in the previous analyses.

The S–Z decrement, if present, can now be seen on a short-baseline map. Mapping the shortest baselines 0–1 kλ usually provides the deepest hole, while mapping baselines 0–2 kλ can give better shape and positional information, if there is enough signal-to-noise. In the case of TEXOXL20, for example, after the initial removal of the seven NVSS-selected point sources based on long-baseline information, there is a significant decrement of $-400\,\mu$Jy beam^{-1} on the 0–1 kλ map, which is expected to have an r.m.s. noise of $80\,\mu$Jybeam^{-1}; see Figure 2.2b. After subtraction of the four residual sources, the 0–1 kλ decrement changes by 1σ, to $-320\,\mu$Jy beam^{-1} . Indeed this weak effect of the residuals is a general trend: for all of the cluster candidates, the subtraction of the weaker, residual point sources produces very little change in the fluxes of the short-baseline decrements.

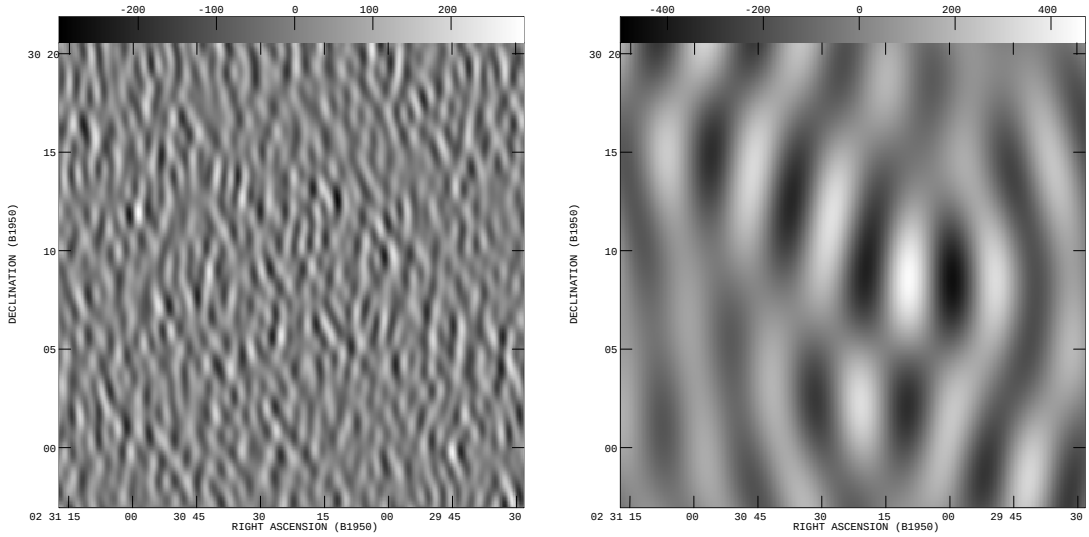

(a) (b)

Fig. 2.2: Demonstration of source subtraction for the TEXOXL20 region, continued. (a) Long baseline ($> 2\,k\lambda$, not CLEANed) map consistent with noise, after removal of "residual" point sources. (b) Short baseline ($< 1\,k\lambda$) map showing the S–Z hole at map centre, accompanied by the synthesized beam pattern.

2.3 Extended Sources at the Cluster Centre

So far, short-baseline maps of about twenty cluster regions show clear, significant S–Z decrements after point source subtraction. However, their centres are often different from the positions predicted from the centroid of the gas X-ray emission by up to an arcminute — a significant displacement, given pointing errors and statistical noise.[2] In addition, some have odd shapes, resembling tear-drops [see Abell 665, Figure 3.10] or triangles [see Abell 1914, Figure 3.21], which do not match the more circular/elliptical gas shapes seen on the corresponding X-ray maps, and statistically cannot be the result of interferometer noise; see section 3.2.1 for an in-depth discussion of the shape and position of the Abell 2218 decrement.

Further investigations of the radio environment around these clusters, using, for example, VLA maps, show the strong possibility that extended, contaminating radio sources exist in the Ryle Telescope's field-of-view and would not be visible in the long-baselines. Quite often, the extended sources lie near the centres of these clusters and happen to have angular scales similar to those of the S–Z shadow, producing distortions of the S–Z shapes. Evidence for these extended sources is detailed

[2] Inaccurate pointings could be a possible cause the positional offsets. However, random errors on the Ryle Telescope's positional calibration, usually induced by momentary, slight displacements (< 30 arcsec) of radio aerials by the wind, are reduced after several days of data-taking to under a few arcseconds, as is evidenced by the agreement of radio source locations to those in existing catalogues. Also, while the X-ray satellites can have larger pointing errors (5 arcsec for ROSAT HRI; 15 arcsec for ROSAT PSPC), the positions are re-calibrated by matching X-ray point sources to known stars or AGNs. Positional errors in both the radio and X-ray maps are further discussed in section 3.2.1.

for each cluster in Chapter 3. In some cases, the extended flux appears to be directly associated with bright point sources; but often, the flux is extended over the central one or two arcminutes of the cluster, without proximity to any point sources. What is producing these cluster centre "halos"? Three possible cluster-associated physical phenomena that can produce this kind of extended radio emission are now summarized:

2.3.1 Aggregates of low-flux radio sources

Source surveys have shown that galaxy clusters are associated with a higher density of sources than is characteristic of inter-cluster space. For example, cross-correlation of the 1.4 GHz VLA FIRST radio survey and the Abell catalog shows that the density of radio sources within a few arcminutes of an Abell cluster is at least twice the density in non-cluster regions [Cress 1996]. Moreover, a survey of 50 cluster regions targeted for the S–Z effect at 28.5 GHz shows the density of radio sources within 4 arcminutes of these very rich clusters to be 4–7 times the density in non-cluster regions [Cooray 1998]; the source counts in the current RT sample show a similar trend, discussed in detail in section 3.1. The overdensity of radio sources near clusters is, of course, expected; since the density of galaxies is higher in a cluster, there is a larger *ab initio* chance of having an AGN or star-forming galaxy in the field-of-view. Moreover, cluster mergers may possibly trigger AGN formation as well as star formation; also, radio emission of AGNs can be more luminous as AGN jets crash into the intracluster plasma [Clusters 1994]. Finally, the cluster can gravitationally lense background radio sources, increasing the fluxes of sources in a ring around the cluster centre, with a radius corresponding to the Einstein angle ($\alpha \approx 30''$) [Loeb 1997].

A group of many low-level sources may conspire to produce a seemingly "diffuse" source that is not properly isolated in the VLA catalogues. For example, the NVSS VLA 1.4 GHz map of Abell 773, shows three or four compact features embedded in a diffuse ring in the cluster centre. Deeper VLA data, with better resolution, confirms this structure; see Figure 3.15. Analysis of the S–Z effect in the RT data, however, is not seriously impaired by this kind of multi-component source; the RT long baselines resolve the "ring" into ten compact sources with separate fluxes of 150–200 μJy (3–4 σ in this case) in the longer baseline map; see further discussion in section 3.2.4.

2.3.2 Radio halos induced by cluster mergers

Cluster mergers can easily amplify magnetic fields and accelerate particles to the point that synchrotron emission, spread throughout the impact region, can be observed at radio frequencies ; see, e.g, [Giovannini 1999]. Among the catalogue of known galaxy clusters, such bright radio "halos" are rare, in accordance with the physical picture that they are essentially transient phenomena. The time between mergers is estimated to be a few 10^9 years; the particles accelerated in a merger lose their energy through inverse-Compton losses and synchrotron emission on shorter time scales of 10^8 years [Tribble 1993]. The best studied halos — e.g., the ones in Coma, Abell 2255, and Abell 2256 — appear in clusters with strongly distorted X-ray gas distributions, as would be expected of recently

merged clusters. The observed halos generally have the steep spectral indices $\alpha > 1$, defined by $S \propto \nu^{-\alpha}$, where S is the source flux, an ν is the frequency. Such indices are expected of synchrotron emission of particles which have stopped being accelerated and have been losing energy for at least 10^7 years. However there is evidence that the central regions of the halos may have a "younger" component with $\alpha \approx 0.8$, which has more recently been accelerated by AGNs in the cluster; see, e.g, the study of the Coma cluster halo in [Deiss 1997]. Despited the reputed rarity of merger halos, a search for strong S–Z effects strongly biases the targeted clusters to be hot and big — exactly the kind that may have recently undergone mergers and may contain these kinds of halos.

2.3.3 Cooling-flow "mini-halos"

Finally, non-merging clusters may house extended radio sources at their centres in the forms of cooling-flow "mini-halos". For example, the Perseus cluster has a radio-emitting galaxy 3C84 at its centre which is associated with amorphous radio emission extended up to 100 kpc away from the centre, over the whole cooling-flow region. A likely explanation for the extended emission is that the inward cooling flow of the hot gas, easily visible in the X-rays map of Perseus, compresses the magnetic field and re-enhances fast particle energies (which had fallen after initial acceleration in a merger) in the central region, re-inducing detectable synchrotron radiation [Burns 1992]. Such amorphous emission has been sensitively observed in several nearby ($z \approx 0.05$) cooling-flow clusters, with a radio luminosity at 5 GHz of up to $10^{23} h^{-2}\,\mathrm{W\,Hz^{-1}}$, and spectral indices of $\alpha \approx 1 - 1.4$, between 1.4 GHz and 5 GHz; see, e.g, [Burns 1990]. Thus a cooling-flow cluster targeted for S–Z detection, at redshift $z \approx 2$, may have an amorphous mini-halo with a flux of up to 1 mJy at 15 GHz. The RT deep map of Abell 1413 appears to show such emission, spread over the cooling flow region.

A note on semantics: the term "radio-halo" has been used in the literature to describe several kinds of objects, ranging from unresolved complexes of radio sources [Moffet & Birkinshaw 1989] to any extended radio structures not clearly associated with a particular galaxy [Deiss 1997]. In this thesis, the word "halo" will be used to generically describe any radio source extended over at least 30 arcseconds lying near the cluster centre; it is not meant to imply that a particular mechanism (e.g., merger-induced synchrotron radiation) is responsible for the emission.

Because the halo and the S–Z effect in a given cluster have similar angular scales as well as similar positions at the cluster centre, removal of the halos requires modelling of both the expected negative S–Z hole and the positive radio halo. For the eight H_0 clusters, X-ray maps as well as deep lower-frequency radio data are available to assist in such modelling; a method to effect the hole/halo separation is described below. For the other clusters, such additional X-ray and radio information is not available yet. Instead the error induced on the S–Z detection by un-subtracted extended flux must be assessed on a case-by-case basis; see Chapter 3 for details on this error assessment.

2.4 Estimating the Hubble Constant

To estimate the Hubble constant from a given cluster it is first necessary to constrain its gas temperature and its 3-dimensional density distribution. I take the gas temperature to be constant, independent of radius, which is consistent with a gas distribution described by the isothermal β-model, or King profile:

$$n_e(r) = n_0 \left[1 + \left(\frac{r}{r_c} \right)^2 \right]^{-3\beta/2}, \tag{2.2}$$

where n_0 is the central gas density, r_c is the core radius (around 200 kpc, corresponding to an arcminute, for most of the clusters considered here), and β has been measured to be 0.65 for a large selection of clusters [Jones & Forman 1984]. For relaxed clusters, the above isothermal description has been shown to be a good approximation to the actual temperature and density distributions for $r < 3r_c$; see, e.g, [Markevitch 1998]. Since many of the clusters appear to have elliptical shapes, with axis ratios of up to 1.5, a scaled/rotated modification of the spherical profile (2.2) is actually used, allowing for different core radii along the major/minor axes of the ellipsoid; two of the axes are assumed to be perpendicular to the line-of-sight, while the core radius along the third axis (along the line-of-sight) is assumed to be the geometric mean of the other two. Systematic errors produced by these assumptions about geometry and isothermality are discussed in detail in Section 4.1.

The parameters from the X-ray fits are summarized in Table 2.1. They have been determined with the PROFILE package, written by Grainge and Jones, which uses a simplex minimization routine to fit an ellipsoidal King profiles (plus constant backgrounds) to ROSAT images.[3] Uncertainties in these X-ray fits induce very little error in the expected S–Z distribution; see, e.g., [Birkinshaw & Hughes 1994]. Systematic checks on X-ray fit uncertainities have been carried out, comparing results of fitting HRI and PSPC maps of the same cluster as well as comparing models obtained by including and excluding cooling-flow regions. The alternative fits, also compiled in Table 2.1, yield an estimated systematic uncertainty on the predicted central S–Z decrements to be much smaller than uncertainties induced by, for example, the errors on the X-ray temperatures.

Having a model of the gas from the X-rays then allows for a prediction of the shape and depth of the S–Z shadow, if the distance scale, or, equivalently, H_0, is known; otherwise, only the combination n_0^2/H_0 is properly constrained. To separate out n_0 and H_0 using the S–Z measurement (proportional to n_0/H_0), PROFILE simulates a set of visibilities that the RT would see if H_0 were 50 $\mathrm{km\,s^{-1}Mpc^{-1}}$. Then, by fitting for r_{50}, the scale factor by which the simulation hole needs to be multiplied to fit the RT data, PROFILE finds the true Hubble constant as $\frac{50}{r_{50}^2}\,\mathrm{km\,s^{-1}Mpc^{-1}}$.

The presence of extended cluster-centre sources complicates things, however. I have written a modification of the PROFILE code to fit the point-source-subtracted RT visibilities to a model with both a scaled version of the X-ray-predicted hole and a circular gaussian extended "halo" source .

[3] I have made use of maps taken from the ROSAT Data Archive of the Max-Planck-Institut fur extraterrestrische Physik (MPE) at Garching, Germany.

To encode possible prior knowledge from, for example, lower frequency VLA maps, about the flux, width, and location of the halo, quadratic terms are included in the χ^2 to provide (generally very loose) constraints on the halo parameters. The attempt to fit the halo clearly increases the H_0 measurement's systematic error, which must be estimated by marginalizing over the halo fit variables.[4] In practice, both the halo and the Hubble constant are constrained moderately well in cases where the halo has smaller angular scales than the S–Z effect and/or a substantially off-centre location. In most clusters, uncertainties in the halo flux subtraction increases the uncertainty in the H_0 determination by a factor of two over what would be expected for just the statistical noise on shortest baselines.

[4] This error analysis is actually done by fixing the hole scale factor $r_{50} \equiv 1/\sqrt{h_{50}}$ to values 0.1 higher, and 0.1 lower, than the best fit value, by re-fitting the halo, and by then seeing how the χ^2 increases. Extrapolating to where the χ^2 goes up by 1 gives the marginalized error on the scale factor.

Cluster	z	Imager	Exp. Time (sec)	$\varepsilon_X/10^{-63}$ $\left(\frac{\text{counts}}{\text{s Mpc}^2\ \text{cm}^3}\right)$	T_e (keV)	$n_0 h_{50}^{-\frac{1}{2}}$ (10^3m^{-3})	$r_c^{(1)}$	$r_c^{(2)}$	α (°)	RA (B1950)	Dec (B1950)	$\Delta T_{SZ} h_{50}^{-\frac{1}{2}}$ (mK)
A665	0.182	PSPC	38297	2.93	$9.03^{+0.35}_{-0.52}$	5.15	83	72	-30	$8^h26^m24.6^s$	66°01′03″	$-0.89^{+0.06}_{-0.05}$
A665	0.182	HRI	98302	1.24	$9.03^{+0.35}_{-0.52}$	4.73	92	76	-38	$8^h26^m25.6^s$	66°01′06″	$-0.86^{+0.06}_{-0.05}$
A697	0.282	HRI	28127	1.36	$8.0^{+0.9}_{-0.7}$	7.01	59	44	-17	$8^h39^m46.6^s$	32°32′43″	$-1.01^{+0.11}_{-0.10}$
A773	0.217	HRI	16664	1.53	$8.7^{+0.7}_{-0.7}$	6.39	52	45	-13	$09^h14^m23.3^s$	51°56′10″	$-0.91^{+0.07}_{-0.07}$
A1413	0.143	PSPC	7696	3.41	$7.54^{+0.29}_{-0.27}$	13.6	52	35	0	$11^h52^m44.8^s$	23°41′01″	$-0.89^{+0.07}_{-0.07}$
A1413 †	0.143	PSPC	7696	3.41	$8.5^{+1.3}_{-0.8}$	8.79	67	45	0	$11^h52^m44.9^s$	23°41′03″	$-0.86^{+0.13}_{-0.08}$
A1413	0.143	HRI	18858	1.45	$7.54^{+0.29}_{-0.27}$	10.2	78	52	26	$11^h52^m43.7^s$	23°41′09″	$-0.87^{+0.07}_{-0.07}$
A1413 †	0.143	HRI	18858	1.45	$8.5^{+1.3}_{-0.8}$	7.21	101	68	7	$11^h52^m43.8^s$	23°41′12″	$-0.87^{+0.13}_{-0.08}$
A1704	0.220	HRI	41291	1.60	$4.73^{+0.38}_{-0.33}$	20.5	24	16	40	$13^h12^m36.2^s$	64°50′22″	$-0.59^{+0.05}_{-0.04}$
A1704 †	0.220	HRI	41291	1.57	$5.7^{+3.5}_{-1.3}$	8.65	42	30	35	$13^h12^m35.6^s$	64°50′18″	$-0.52^{+0.32}_{-0.12}$
A1914	0.171	PSPC	9036	3.13	$8.56^{+0.65}_{-0.65}$	17.1	51	40	-74	$14^h23^m58.5^s$	38°02′48″	$-1.64^{+0.12}_{-0.12}$
A1914††	0.171	PSPC	9036	3.13	$8.56^{+0.65}_{-0.65}$	14.1	81	64	-77	$14^h23^m58.4^s$	38°02′48″	$-1.54^{+0.11}_{-0.11}$
A2218	0.171	PSPC	43985	3.16	$7.05^{+0.36}_{-0.35}$	7.26	65	59	11	$16^h35^m42.5^s$	66°18′30″	$-0.70^{+0.04}_{-0.04}$
A2218	0.171	HRI	91965	1.34	$7.05^{+0.36}_{-0.35}$	5.39	59	75	6	$16^h35^m41.0^s$	66°18′31″	$-0.60^{+0.03}_{-0.03}$
0016+16	0.546	PSPC	44157	3.17	$7.55^{+0.14}_{-0.12}$	9.88	35	28	36	$00^h15^m58.5^s$	16°09′35″	$-1.16^{+0.20}_{-0.20}$
0016+16	0.546	HRI	70228	1.35	$7.55^{+0.14}_{-0.12}$	7.28	47	35	58	$00^h15^m58.8^s$	16°09′28″	$-1.08^{+0.20}_{-0.20}$

Tab. 2.1: X-ray data relevant for H_0 analysis. Maps are taken from ROSAT satellite detectors [PSPC = Position-Sensitive Proportional Counter; HRI = High Resolution Imager], with on-times and X-ray emission constants ε_X, taking into account absorption by galactic hydrogen, from Kneissl [Kneissl 1999]. Plasma electron temperatures, based on ASCA spectra, are from [Allen & Fabian 1998] and [Miyoshi 1999]; 90% confidence intervals are given. See text for assumed form of ellipsoidal King profile distribution; the table gives central electron density n_0, transverse core radii $r_c^{(1)}$ and $r_c^{(2)}$, position angle α, and fitted cluster centre. The expected S–Z decrement ΔT_{SZ} is calculated along a line-of-sight through the cluster centre. For cooling-flow clusters A1413 and A1704, fits have been obtained both including the cooling-flow region, and excluding the cooling flow region (latter results marked with †). Also, A1914 has been re-fitted with a more appropriate $\beta = 0.91$ (††).

3. THE CLUSTERS

This chapter summarizes the Ryle Telescope's searches for the S–Z shadows of galaxy clusters; the pointing centres for the twenty targets with significant S–Z decrements are listed in in Table 3.4. Before describing the results obtained from the S–Z searches, the radio source environment in these rich clusters is characterized; these results will be particularly useful in understanding source confusion in future radio experiments focusing on galaxy clusters.

3.1 Radio Source Counts in the Cluster Environment

For sources within a few arcminutes of the Ryle Telescope's pointing centre, the fluxes can be accurately corrected for attenuation due to the RT primary beam response, which has been empirically parameterized by beam holography as a power law:

$$B(r) = 1.0 - 2.08 \times 10^{-4} r - 2.61 \times 10^{-5} r^2 + 5.32 \times 10^{-8} r^3, \tag{3.1}$$

where r is the distance from the pointing centre in arcseconds. In practice, the above formula describes the primary beam well for $r < 4$ arcminutes, at which the attenuation is 20%. Beyond this radius, the primary beam response is not very smooth — the first null of the beam occurs at $r \approx 5$ arcminutes — and varies depending on which pairs of aerials are used in the map [Grainge 1996]. The parametrization in eq. (3.1) has been checked, for example, by measuring the fluxes of the three bright (> 1.5 mJy) sources present in the Abell 2218 field-of-view as they appear in six RT pointings offset from the cluster centre by one arcminute; the fluxes are compiled in Table 3.3.

With 80 separate radio sources found in 20 separate cluster fields, a preliminary analysis of the spectra and flux distributions of the sample can be carried out. About half of the observed sources are close enough to the appropriate Ryle pointing centres to allow for proper correction for primary beam attenuation and have clear matches in available 1.4 GHz maps. For these sources, ranges of the spectral index α, defined by $S \propto \nu^{-\alpha}$, allowed by the 1-σ ranges of fluxes S measured at $\nu = 1.4$ GHz and $\nu = 15$ GHz have been computed. All the sources have $\alpha > 0$, i.e., flux falling with frequency, except for one source in Abell 2218, corresponding to source 12 in [Moffet & Birkinshaw 1989], which has a rising spectrum, $\alpha_{1.4}^{15} \approx -0.4$. This unusual source has also been noted in, e.g., [Cooray 1998], and is not included in computing statistics of the spectra.

The mean spectral index of these 42 sources is found to be $\alpha = 0.82 \pm 0.06$, with an r.m.s. of 0.4; the median is 0.77. To get a clean sample with well-defined fluxes, a requirement that source fluxes be at least 400 μJy at 15 GHz, is imposed, effectively cutting out any sources with less than

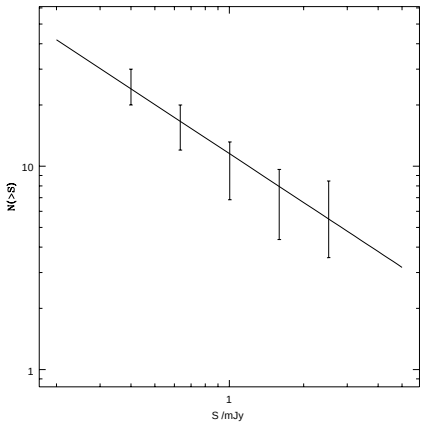

Fig. 3.1: RT counts of radio sources in sixteen regions of radius 4 arcminutes around rich clusters at $z < 0.3$. The line is the power-law fit $N(>S) = 24\,(S/400\,\mu\mathrm{Jy})^{-0.8}$

.

5σ significance; the resulting sample of 22 sources has a barely changed mean of 0.77 ± 0.07, with a smaller r.m.s. of 0.35, and median of 0.82. At this level of statistics, the observed spectral index distribution in rich cluster regions is indistinguishable from the spectra of the corresponding 5 GHz millijansky population in intercluster space, which has a median of 0.75 [Donnelly 1987]. In addition, the spectra values are in good agreement with the statistics of $\alpha_{1.4}^{28.5}$ obtained in a similar analysis of the source environments of rich clusters done at 28.5 GHz by Cooray *et al.*. They find a mean and median of 0.71 ± 0.08 and 0.71 in a sample of 52 radio sources found within $250''$ of 56 rich galaxy cluster.

The flux distributions of the sources also provides useful information on the cluster's radio environment. Figure 3.1 shows the 15 GHz source counts for radio sources observed by the Ryle Telescope. These sources are taken from sixteen observed clusters with $z < 0.3$, since two of the higher-redshift candidates, TEXOXL20 and TEXOXL21, have been selected for having loud radio environments. In addition, the distances of radio sources from the RT pointing centre are required to be greater than 1 arcminute, to avoid contamination from gravitationally lensed and halo-type sources, and less than 4 acminutes, to allow for correction for primary beam attenuation.

With the above selection, the observed distribution of 25 sources with flux $0.4\,\mathrm{mJy} < S_{15} < 3\,\mathrm{mJy}$ is fitted well to $N(>S) \propto S^{-0.8\pm0.2}$. The fitted exponent agrees with the corresponding values of 0.96 ± 0.14, found for millijansky sources near rich clusters at 28.5 GHz [Cooray 1998], and 0.8 for a non-cluster-selected 5 GHz mJy population [Donnelly 1987]. All the exponents describe flatter distributions than those expected in a non-evolving Euclidean universe, where the value would be 1.5.

One outstanding question is how the overall number density of the RT source counts compares to the density in observations of areas without rich galaxy clusters, which are often used to calculate, e.g., the noise due to low-flux source confusion expected in S–Z detections. A 1.4 GHz survey in

areas without rich galaxy clusters finds 354 radio sources with flux greater than 1.5 mJy in a total surveyed area of about $12\,\mathrm{deg}^2$ [Condon 1990]. Using the observed distributions of $\alpha \approx 0.75$ and $N(>S) \propto S^{-0.9}$, the (non-cluster-selected) source counts would predict only 4 or 5 sources to be present with flux greater than $400\,\mu$Jy in the sixteen RT observations of $z < 0.3$ clusters, covering a total area of $0.2\,\mathrm{deg}^2$. The actual number observed is 25, indicating that there are 4 to 6 times as many sources in the rich cluster regions than expected from intercluster source counts. This agrees with the estimate by Cooray *et al.* of an overabundance, by a factor of 4 to 7, of millijansky sources at 28.5 GHz in rich cluster regions.

If the observed overabundance of millijansky radio sources near rich clusters is characteristic of microjansky sources as well, earlier estimates of the error induced in the S–Z analysis by source confusion may need to be revised. For example, the analysis by Grainge, based on the microjansky source counts of Windhorst *et al.*, predicted $\sigma \approx 50\,\mu\mathrm{Jy}(\mathrm{S_c}/100\,\mu\mathrm{Jy})^{0.35}$ to be the r.m.s. in a 2 arcminute FWHM synthesized beam at 15 GHz induced by sources less than a source-subtraction flux limit S_c (generally 150–200 μJy for most of the RT cluster observations) [Grainge 1996]. For most of the RT S–Z detections, the statistical noise on shortest baselines ranges from $70\,\mu$Jy to $120\,\mu$Jy and will thus dominate Grainge's predicted confusion noise. However, if these unsubtracted faint microjansky sources are overabundant by more than a factor of two near rich clusters, as is observed in millijansky sources, then it is possible that the S–Z detections of the RT, as well as those of other interferometer experiments, are dominated by source confusion noise. This point is discussed further in Section 4.1.

3.2 Hubble Constant Clusters

The following section summarizes the analysis of eight clusters using the new, automated point source subtraction and hole/halo separation methods that are the focus of this thesis. An especially detailed summary is given of Abell 2218, for which the most RT data is available, and which has been observed by several other groups in S–Z searches; see, e.g, Birkinshaw's recent review [Birkinshaw 1998]. Then, the H_0 analyses of Abell 665, Abell 697, Abell 773, Abell 1413, Abell 1704, Abell 1914, and CL0016+16 are discussed. The clusters have redshifts ranging from 0.14 to 0.28, with the exception of CL0016+16, at $z = 0.546$. In addition, several clusters which exhibit significant S–Z effects, but for which the X-ray information necessary for H_0 measurements are not yet available, are discussed.

The H_0 estimates reported in this section are given with systematic errors resulting from the halo fit, with the central value giving the H_0 with maximum likelihood, and the error bars marking the 68% (1-σ) confidence interval. Additional uncertainties, due to source confusion, temperature errors, and assumptions related to the cluster geometry will be discussed in detail in Section 4.1, along with quantitative comparisons to other experiments.

Table 2.1 contains information on the gas temperatures and density distributions as measured from X-ray maps and spectra. When quoted in the text, errors on gas temperatures correspond to 90% confidence intervals; when obtaining a combined value of H_0, the temperature errors are appropriately reduced to correspond to 68% 1–σ confidence intervals.

3.2.1 Abell 2218

The cluster Abell 2218 at $z = 0.171$ is historically the best studied cluster for the S–Z effect, with more than a dozen attempts at S–Z detections by various groups published in the literature [Birkinshaw 1998]. Moreover, it is the subject of several deep X-ray and lower-frequency radio observations, discussed below, allowing for a detailed understanding of the cluster source environment; the gas temperature has been constrained to be $7.05^{+0.36}_{-0.35}$ keV [Allen & Fabian 1998]. It is the target cluster for which the Ryle Telescope has taken the most data. In addition to a total of 30×12 hours of RT data taken at the central pointing, 7×12 hours of data at each of six pointings offset at 1 arcmin from centre has been taken, in an attempt to get a "mosaiced" image of the S–Z shadow.

Inital radio source subtraction

There are three bright point sources (> 1.5 mJy) within four arcminutes of the A2218 central pointing centre, at RA $16^h35^m42.0^s$, Dec $66°18^m46^s$ (B1950). The fluxes and locations of each of these sources are fitted by the FLUXFITTER code for the central pointing data set and for each of the six offset pointing data sets separately. Table 3.3 lists the sources and shows that the fluxes seen at each pointing agree well with each other, after correction due to the primary beam attenuation.

After this initial source subtraction, it is instructive to look at the data from each of the pointings separately. Firstly, the central pointing, with the most data, shows a significant decrement on 0–1 kλ baselines of $-460 \pm 110\,\mu$Jy beam^{-1}, shown in the first panel of Figure 3.2, displaced 30 arcseconds east of the RT pointing centre. The location is expected to have a 1-σ variation of approximately the HWHM of the synthesized beam (60 arcseconds) divided by the signal-to-noise, or 14 arcseconds, in this case. As a check on this commonly used estimate of the effects of interferometric noise [see, e.g, [Cooray 1998]], I have carried out simulations of RT visibilities produced by an S–Z decrement having the same King profile parameters as that of Abell 2218, listed in Table 2.1, along with the noise expected after 30×12 hours of data-taking. The locations of the deepest decrements on these maps, shown in the last seven panels of 3.2, are scattered with an r.m.s. of 13 arcsec, in agreement with the HWHM/signal-to-noise estimate.

The S–Z decrement location at the central pointing, however, disagrees by 2.5σ with the X-ray centroid, fitted to be 15 arcseconds south of the RT pointing centre. Including the data from the six offset pointings makes the disagreement worse; the 0–1 kλ maps are shown in the first six panels of Figure 3.3. The deepest decrements in these six maps have an average of $-501\,\mu$Jy beam^{-1}, with an r.m.s. of $170\,\mu$Jy beam^{-1}, which agrees with the 1-σ noise estimate of $160\,\mu$Jy beam^{-1} for each pointing. The locations have an average displacement of (-45,18) arcseconds in (RA, Dec) from the pointing centre, with an r.m.s. of 18 arcseconds, agreeing well with the HWHM/signal-to-noise estimate of 19 arcseconds. The data from all the central and offset pointings can now be combined. For the purpose of making maps, they are simply averaged together; the averaging throws away some of the information obtained by the offset pointings at the periphery of the field-of-view, but properly

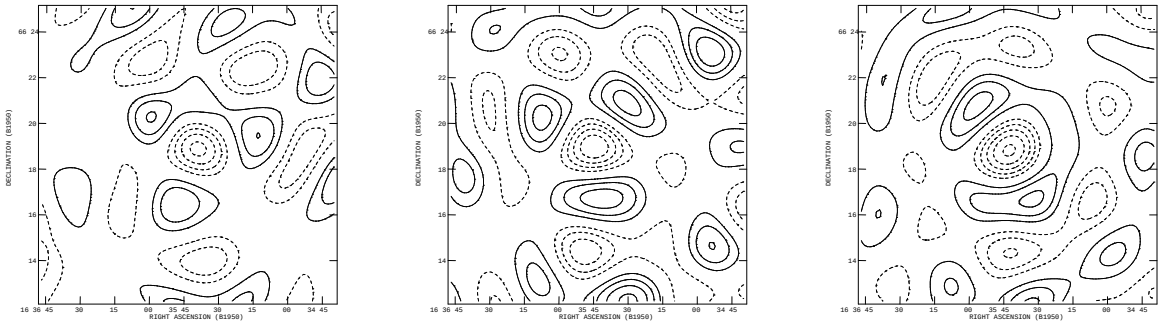

A2218 central pointing | Simulation 1 | Simulation 2

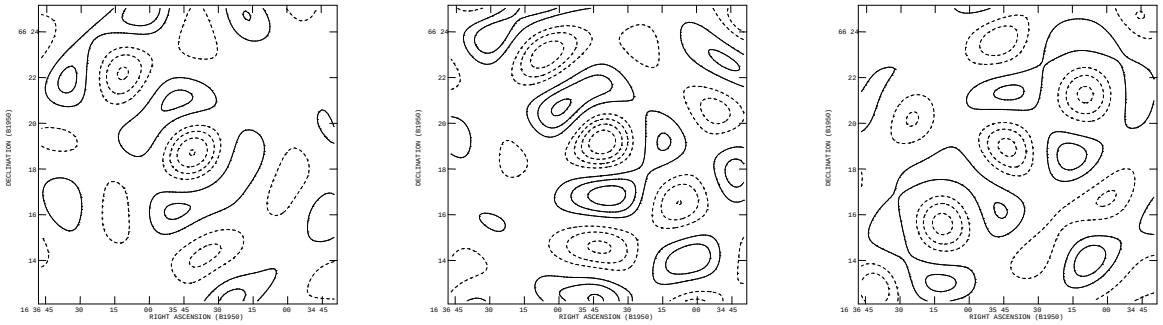

Simulation 3 | Simulation 4 | Simulation 5

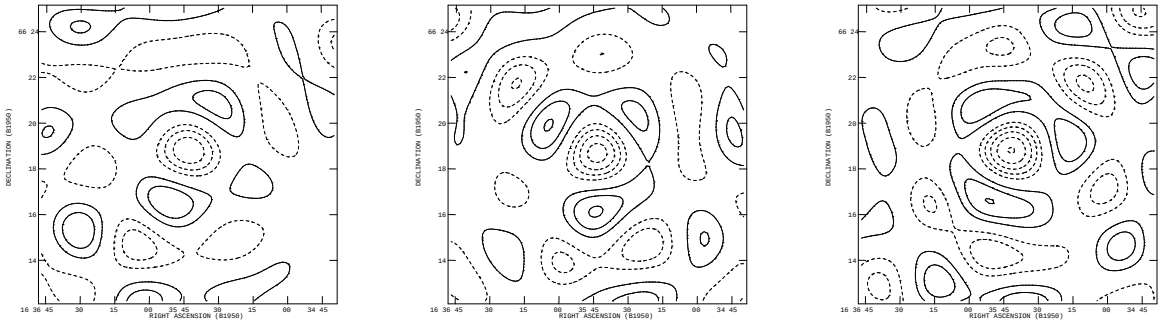

Simulation 6 | Simulation 7 | Simulation 8

Fig. 3.2: The Abell 2218 S–Z decrement at the central pointing, data with three point sources subtracted (first panel) and simulations (other panels) to show the effects of interferometer noise . Maps (not CLEANed) are of 0–1 kλ baselines, and have contour spacings of $100\,\mu$Jy beam^{-1}. The simulated cluster parameters are those from the PSPC fit in Table 2.1, with $H_0 = 50\,\mathrm{km\,s^{-1}Mpc^{-1}}$.

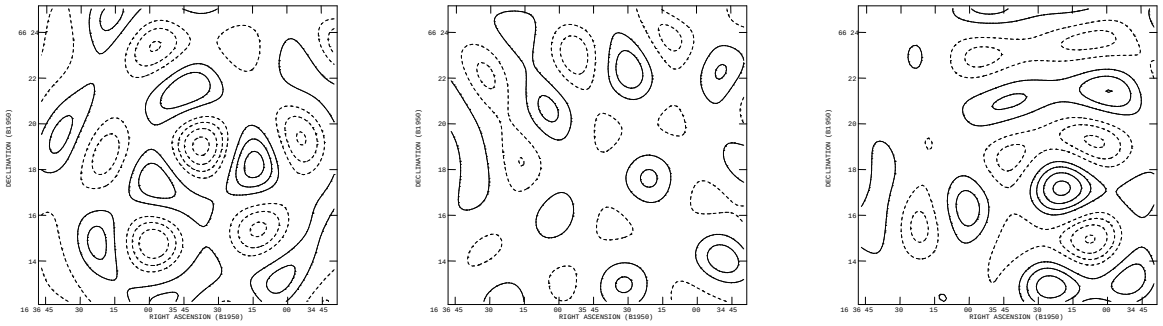

A2218 N pointing | A2218 NW pointing | A2218 SW pointing

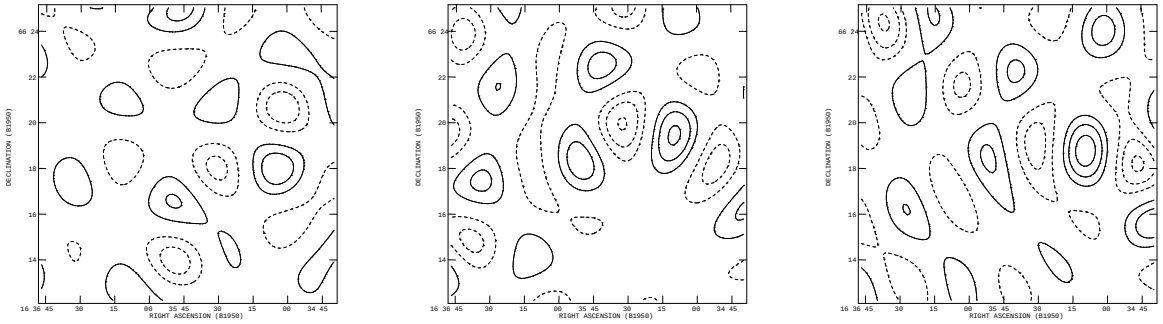

A2218 S pointing | A2218 SE pointing | A2218 NE pointing

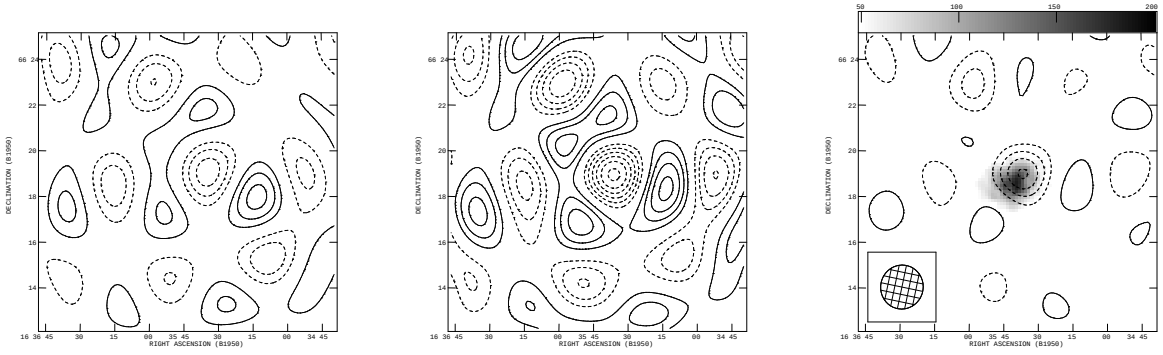

A2218 offset pointings | A2218 all data | A2218 all data, CLEANed

Fig. 3.3: More data on Abell 2218, with three point sources subtracted. The top six panels show maps (not CLEANed, contour spacing: $180\,\mu\mathrm{Jy\,beam^{-1}}$) from six offset pointings displaced in a hexagonal pattern 1-arcminute from the cluster centre. Bottom row: six offset pointings combined (cont. spacing: $100\,\mu\mathrm{Jy\,beam^{-1}}$); all data, from central and from offset pointings, combined (cont. spacing: $60\,\mu\mathrm{Jy\,beam^{-1}}$); and CLEANed map of all data (cont. spacing: $80\,\mu\mathrm{Jy\,beam^{-1}}$) on ROSAT PSPC X-ray image (greyscale). Half-power CLEAN restoring beam is shown as hatched ellipse on map.

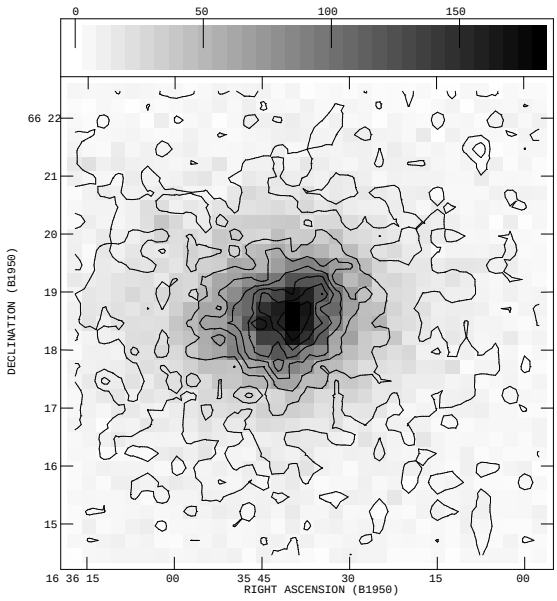

Fig. 3.4: ROSAT HRI image (contours) of Abell 2218 on ROSAT PSPC image (greyscale).

combines the visibilities at the cluster centre.[1] The result is a $-390 \pm 65\,\mu$Jy beam^{-1} decrement[2] on 0–1 kλ baselines displaced by (-48, 16) arcseconds in (RA, Dec) from the pointing centre, with an expected r.m.s. error of 10 arcseconds. This result agrees well with independent analyses of the same RT data sets carried out by Grainge and Jones [Grainge 1996] [Jones 1993]. Note that the decrement location is 6σ off from the predicted X-ray centre at (0, -15) arcseconds from the RT pointing centre.

The discrepancy between the X-ray image of the gas and the location of the S–Z decrement, shown in the last panel of Figure 3.3, makes it imperative to, firstly, check the systematic error on the the astrometry of the X-ray images, and, secondly, to carefully examine whether the source subtraction on the RT data is complete.

X-ray data

Figure 3.4 shows how the X-ray images of Abell 2218 obtained by the ROSAT HRI and ROSAT PSPC detectors agree with each other. The astrometry has been calibrated by matching non-cluster X-ray sources in the maps to known optical counterparts. In particular, the re-calibration of the HRI image,

[1] In particular, note that the offset pointings are only one arcminute from the cluster centre; the primary beam attenuation at the cluster centre in these six data sets is negligible (approximately 7%) compared to statistical noise. In any case, when determining H_0, the primary beam attenuation is included in modelling the visibilities expected at each offset pointing.

[2] The reader might wonder how the decrement in the combined data can be less than the decrements in the various pointings separately. The answer is simply that finding the *deepest* decrements in each separate data set tends to overestimate the actual decrement by approximately 1-σ. This is best understood by thinking about an extreme example: consider an hypothetical field-of-view which contains no actual decrement but only statistical noise. The actual decrement is zero, but, the deepest negative feature on the map will be on the order of 1-σ! To avoid this overestimation in quantitative analyses (like the H_0 determination), it is best to have a specific idea of where to measure the S–Z decrement (e.g., the centroid expected from the X-ray map) before making the short-baseline map.

carried out by matching an X-ray star north-east of the cluster, changes the astrometry by less than five arcseconds; see, e.g., [Markevitch 1997].

How well is the centroid of the X-ray gas constrained? Due to the large number of map pixels containing significant fluxes, the emission-weighted centroids of the X-ray maps is expected to have a statistical error of less than a few arcseconds. The systematic error is checked by comparing the centroids of the PSPC and HRI maps separately; the King profile fits obtained by the PROFILE code give the PSPC centroid to be at RA $16^{\rm h}\,35^{\rm m}\,42.5^{\rm s}$, Dec $66^{\circ}\,18^{\rm m}\,30^{\rm s}$ (B1950); and the HRI centroid to be at RA $16^{\rm h}\,35^{\rm m}\,41.0^{\rm s}$, Dec $66^{\circ}\,18^{\rm m}\,31^{\rm s}$ (B1950). As a further check, Birkinshaw and Hughes [Birkinshaw & Hughes 1994] have used an independent program to fit a smaller sample of the HRI data, and obtain RA $16^{\rm h}\,35^{\rm m}\,41.3^{\rm s}$, Dec $66^{\circ}\,18^{\rm m}\,28^{\rm s}$ (B1950). All these fits agree well with each other; it appears that the X-ray centroid is constrained to within 5 arcseconds of RA $16^{\rm h}\,35^{\rm m}\,42.0^{\rm s}$, Dec $66^{\circ}\,18^{\rm m}\,30^{\rm s}$ (B1950), which is 15 arcseconds below the RT pointing centre. As a final check, Birkinshaw and Hughes have fit the lower-resolution EINSTEIN IPC data [Boynton 1982] and find a centroid of RA $16^{\rm h}\,35^{\rm m}\,42.8^{\rm s}$, Dec $66^{\circ}\,18^{\rm m}\,44.5^{\rm s}$ (B1950), agreeing well within the estimated IPC statistical error of $30''$ of the other centroid fits.

Thus, the X-ray gas fits appears to be well-constrained. But how well should the S–Z effect match the X-ray image? Figure 3.4 clearly shows that Abell 2218 X-ray gas is distorted from a smooth ellipse, and appears to have a maximum of X-ray emission 25 arcseconds east of the gas centroid. Explanations for this distortion have ranged from extra X-ray emission from the cluster's central, dominant galaxy [Boynton 1982], to lensing of a background X-ray source, to actual distortion of the gas by recent cluster merger activity [Markevitch 1997]. The last hypothesis is supported by optical studies of the cluster's redshift distribution [Girardi 1997]; discrepancies between various cluster mass estimates obtained from gravitational strong lensing, gravitational weak lensing, and X-ray analyses [Markevitch 1997]; and the existence of a steep-spectrum cluster-centre "halo" clearly visible at lower-frequencies, which is posisbly induced by a merger [Moffet & Birkinshaw 1989]. Both simulations of cluster mergers [Roettiger 1997] and empirical maps of temperature in nearby hot clusters [Markevitch 1996] show that the cluster may contain strong temperature irregularities (not necessarily tracing the density irregularities that are highlighted by the X-ray map) for at least 1 Gyr after a merger. In particular, if a volume V of the cluster has temperature difference of ΔT_e from the surrounding "isothermal" gas, it will produce an additional S–Z decrement of flux:

$$S_{\rm SZ} \approx 20\mu{\rm Jy} \times \left[\frac{k_{\rm B}\Delta T_e}{10\,{\rm keV}}\right] \left[\frac{n_e}{10^4\,{\rm m}^{-3}}\right] \left[\frac{V}{(100\,{\rm kpc})^3}\right] h_{50}^2, \tag{3.2}$$

using the formulas (1.1) and (1.2). The emission-weighted temperature of Abell 2218 is $k_{\rm B}T_e = 7\,{\rm keV}$, and its central density is fitted to be $n_o h_{50}^{-\frac{1}{2}} = 7\times10^3\,{\rm m}^{-3}$. Off-centre hot/cold regions with $\Delta T_e = \pm 5\,{\rm keV}$, gas densities of $n_e \approx n_0/10 \approx 10^3\,{\rm m}^{-3}$, and volumes of $(400\,{\rm kpc})^3$ [these values are characteristic of temperature irregularities seen in the simulations] will thus produce S–Z flux distortions of approximately $\pm 60\mu$Jy, to be compared to the overall expected decrement on 0–1kλ baselines of $400-500\,\mu{\rm Jy\,beam}^{-1}$. It thus seems marginally possible that several regions of hot and cold spots arranged at distances of a few arcminutes from the cluster centre may produce the observed shift of

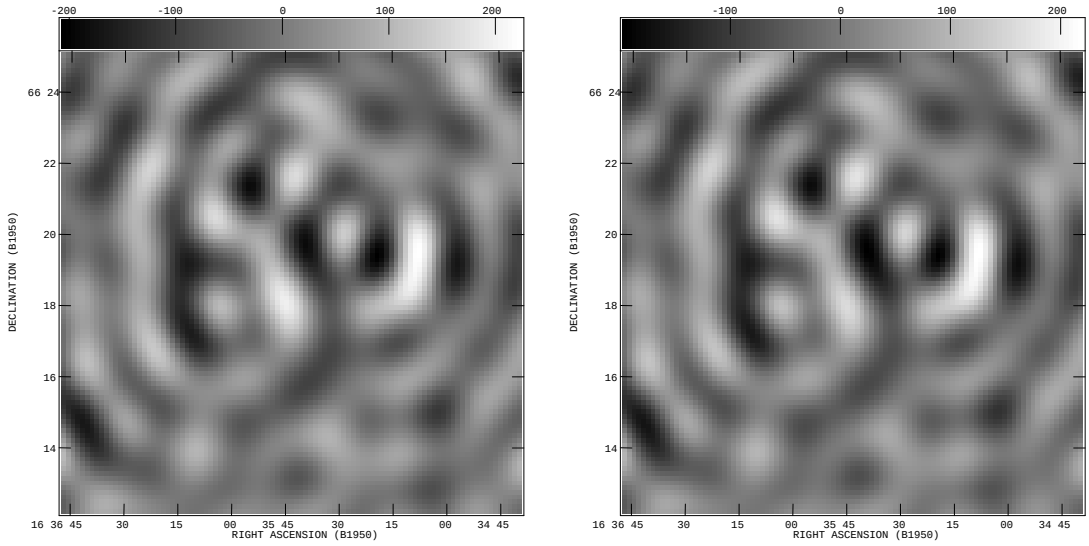

Fig. 3.5: Residual maps of Abell 2218 after initial point source subtraction. Maps (not CLEANed) are of 0–2 kλ baselines; three point sources as well as an X-ray-derived model of the S–Z effect, assuming (a) $H_0 = 50\,\mathrm{km\,s^{-1}Mpc^{-1}}$ and (b) $H_0 = 100\,\mathrm{km\,s^{-1}Mpc^{-1}}$, have been removed from the data.

the S–Z centre by an arcminute from the X-ray centroid. However, it turns out that such a conspiracy is not required; a careful study of the radio environment reveals the existence of residual radio sources which are sufficient to explain the displacement.

Final source subtraction, including "halo source", and H_0 determination

To examine how well the source subtraction has been carried out, a model of the S–Z hole based on a King profile fit to the PSPC X-ray map is subtracted from the RT visibility data, and the 0–2 kλ baselines are mapped. To avoid bias as to the value of H_0, separate maps of these "residuals" are created, one with the subtracted S–Z model made assuming $H_0 = 50\,\mathrm{km\,s^{-1}Mpc^{-1}}$ and the other with the subtracted model made assuming $H_0 = 100\,\mathrm{km\,s^{-1}Mpc^{-1}}$; see Figure 3.5. The residual maps appear to show extended positive flux left near the three subtracted point sources at the periphery of the map, as well as positive flux extended over an arcminute near the centre of the map. Each of these features matches a clear source in the high-sensitivity, high-resolution 5 GHz map of Abell 2218 made with the VLA by Partridge *et al.* [Partridge 1987]. So, apparently the distortion of the S–Z decrement is adequately explained by these residual radio sources, and not by temperature irregularities in the cluster gas, which would manifest themselves as larger, 2-arcminute-scale hot/cold spots in the residual map.

As a further check that the initial source subtraction of three point sources has not somehow produced an artefact in the centre of the map, all-baseline images of the centre and the six offset pointings without any source subtraction have been mapped and then gently CLEANed (20,000 iterations with a gain of 0.01 down to 1.5 times the noise level on each map). The combined map is shown in Figure 3.6a; it is evident that some kind of extended "halo" is filling in the S–Z decrement at the

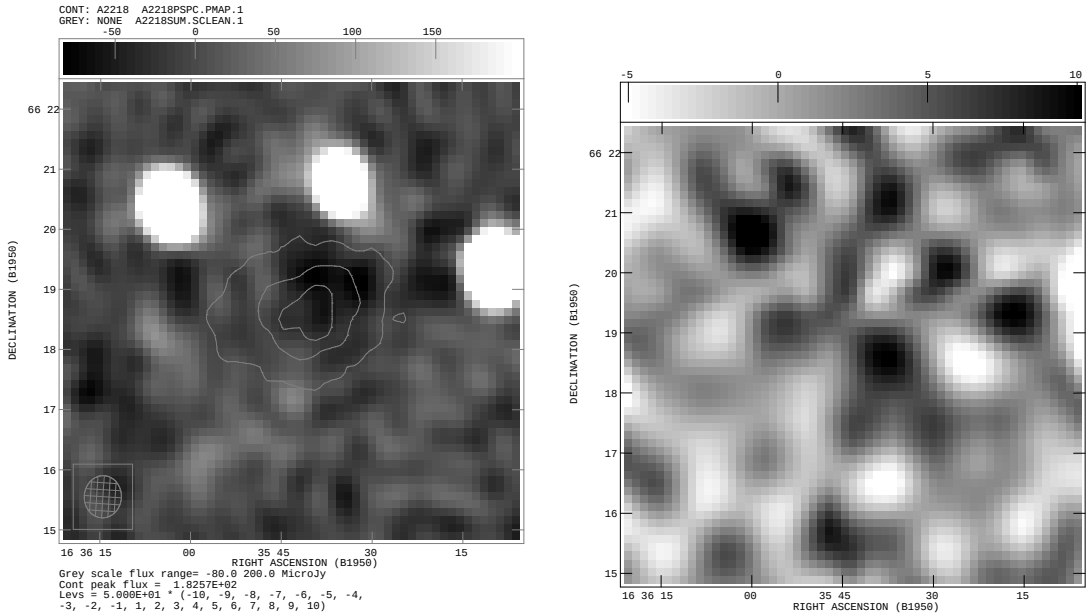

(a) (b)

Fig. 3.6: Further evidence for an extended cluster-centre source in Abell 2218. (a) All-baseline map obtained after carefully CLEANing data from each pointing (no source subtraction attempted), showing the how the S–Z effect (extended black patch near centre of grey-scale map), when compared to ROSAT image (contours) appears contaminated by positive flux. (b) 330 MHz WENSS map showing point sources as well as cluster-centre “halo”.

cluster centre. Further evidence for a complex radio environment around Abell 2218, comes from the 330 MHz WENSS map, Figure 3.6b, which appears to contain a strong radio source extended throughout the cluster centre.

The non-central sources can be modelled as a set of point-like sources along with a set of (circular) Gaussians of FWHM 50" and 70"; see Table 3.4. To avoid bias with respect to H_0, these fluxes and locations have been obtained by fitting two separate sets of residual visibilities corresponding to subtraction of an S–Z model with $H_0 = 50\,\mathrm{km\,s^{-1}Mpc^{-1}}$ and an S–Z model with $H_0 = 100\,\mathrm{km\,s^{-1}Mpc^{-1}}$. The variation in each of the fitted fluxes is less than $10\,\mu$Jy, much smaller than the statistical noise of $35\,\mu$Jy. This insensitivity of the non-central fluxes to the details of the S–Z decrement (also evident in comparison of Figures 3.5a and 3.5b) is due to the sources' large distances (> 2 arcminutes) from the cluster centre. The central extended source, or "halo", is more strongly correlated with the assumed flux of the S–Z hole, however, and must be treated more carefully.

After subtraction of the non-central sources, the decrement on the 0–1 kλ map is reduced to $-150\,\mu\mathrm{Jy\,beam^{-1}}$. This attenuation is, of course, expected: removal of positive point sources at the periphery of the RT field-of-view also removes the negative sidelobes of their un-CLEANed synthesized beams at the map centre. The subtraction of the residuals is not complete until the cluster centre halo is removed as well. This is accomplished by simultaneously fitting the visibilities with a model of the S–Z hole based on the X-ray fits, whose overall scale factor is allowed to vary, combined with a halo, modelled as an elliptical Gaussian with varying widths, position angle, and centre location; see Section 2.4. The result, is a fitted halo flux of $+460 \pm 70\,\mu$Jy and a rescaling of the S–Z King model by $r_{50} \equiv 1/\sqrt{h_{50}} = 0.81 \pm 0.18\,(7.05\,\mathrm{keV}/k_\mathrm{B}T_e)$. Note that the error on the latter parameter has been marginalized over the other fit variables; if only the statistical noise was taken into account, i.e., if the halo model could be removed with no uncertainties, the scale factor would have a smaller error of 0.09. The Hubble constant estimate corresponding to this fit of the S–Z hole is then $H_0 = 77^{+50}_{-25}\,\mathrm{km\,s^{-1}Mpc^{-1}} \times (\mathrm{k_B T_e}/7.05\,\mathrm{keV})^2$. This H_0 value is rather different from the one calculated using the same data set by Grainge and Jones, $H_0 = 38^{+13}_{-8}\,\mathrm{km\,s^{-1}Mpc^{-1}} \times (\mathrm{k_B T_e}/6.7\,\mathrm{keV})^2$ [Grainge 1996] [Jones 1993]. The discrepancy can be traced to two differences in methodology. Firstly, the previous analyses simply averaged the deepest decrements seen in each pointing, rather than averaging the decrements at the same, particular position (e.g., at the X-ray centroid); this produces an overestimate of the S–Z hole depth, and hence significantly underestimates $H_0 \propto \Delta T_{SZ}^{-2}$. Secondly, the previous analyses did not identify the cluster-centre extended halo, and assumed the difference in the X-ray and point-subtracted S–Z images was due to erroneous X-ray astrometry and interferometric noise; taking into account the existence of the halo worsens the systematic error in determining ΔT_{SZ}.

Upon removing the halo, the S–Z decrement is seen to be $-300\,\mu\mathrm{Jy\,beam^{-1}}$ on 0–1 kλ baselines, shown in Figure 3.7. The centroid now also agrees well with that of the X-ray map. Note that, despite the fact that an elliptical King profile was used in the halo/hole separation, the resulting decrement has a rounded triangular shape, agreeing with the shape of the X-ray gas, as well as the dark-matter profile fitted in gravitational lensing studies; see, e.g., [AbdelSalam 1998].

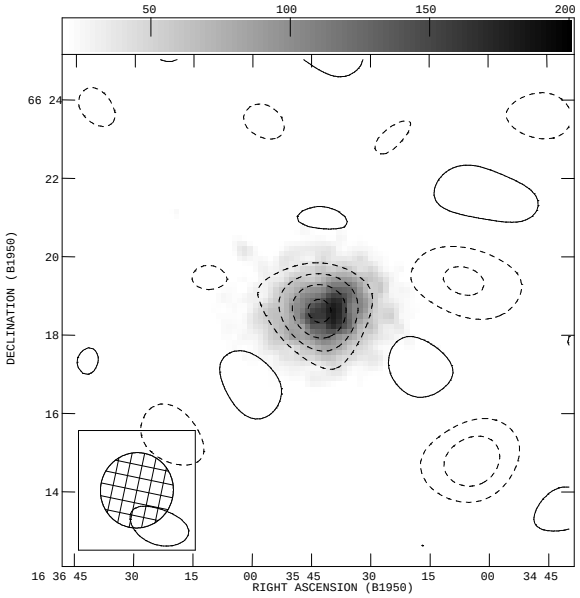

Fig. 3.7: Final CLEANed 0–1 kλ map of Abell 2218 S–Z effect contours, spaced at 65 μJy beam^{-1}) after full source subtraction and halo removal, on ROSAT PSPC image (greyscale).

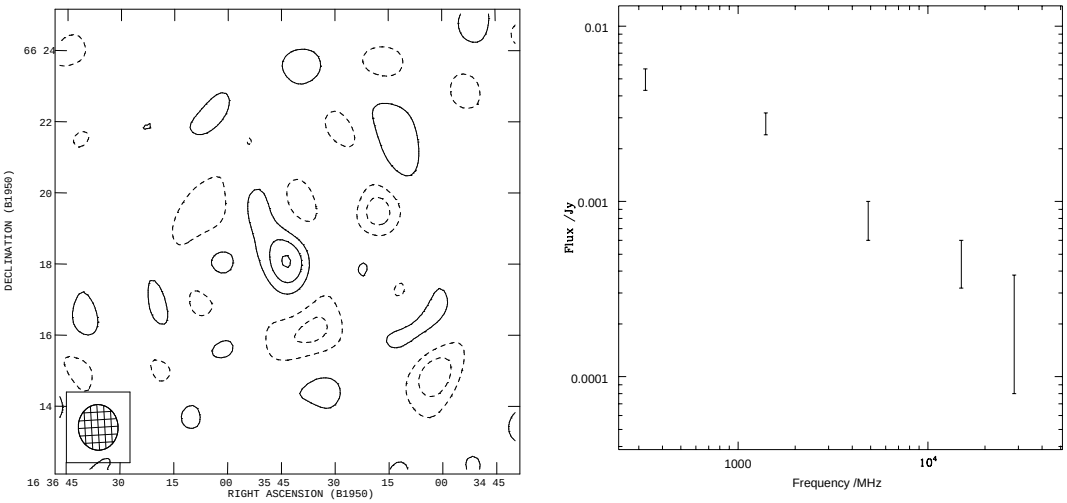

(a) (b)

Fig. 3.8: The Abell 2218 halo. (a) Image (contour spacing: 50 μJy beam^{-1}) obtained by CLEANing 0–2 kλ map of RT data after removing all non-central sources as well as a model of the S–Z hole ($H_0 = 80\,\mathrm{km\,s^{-1}Mpc^{-1}}$); the shape is in agreement with the cluster centre source found in, e.g., [Partridge 1987]. (b) "Spectrum" of the halo source (see text for details).

Several other analyses have apparently ignored the cluster-centre "halo", shown in Figure 3.8a. In particular, Klein *et al.* [Klein 1991] and Birkinshaw *et al.* [Birkinshaw & Hughes 1994] have calculated the spectrum of the source to be steep, $\alpha \approx 1.3 \pm 0.2$, based on the total observed source flux at 1.4 GHz and 5 GHz; extrapolation based on this spectrum would appear to constrain the halo flux to be less than about 200 μJy at frequencies above 10 GHz [Moffet & Birkinshaw 1989]. However, the source is clearly extended, and so different parts of it my have different spectra. Indeed, the halo appears to be present with 500 μJy flux in the 15 GHz RT data, as shown above. In addition, high signal-to-noise OVRO/BIMA images of Abell 2218 at 28.5 GHz show a deconvolved S–Z decrement (before any source subtraction) with a clear crescent shape [Cooray 1998]; this distorted shape would be explained by a +200 μJy halo "eclipsing" the underlying, round S–Z hole.

What is this "halo" object? Figure 3.8b shows the flux of this object plotted as a function of frequency; the fluxes, taken from the WENSS survey, several published VLA observations [Partridge 1987] [Moffet & Birkinshaw 1989], and the OVRO/BIMA map [Cooray 1998], have been approximately corrected to be those appropriate to a beam of FWHM $120'' \times 60''$, at position angle $0°$. If the object is hypothesized to be a merger-induced radio halo, the flux vs. frequency plot should have the "standard" aged synchrotron spectrum [Alex&er 1984]. At low frequencies, the spectrum is expected to have $\alpha \approx 0.5 - 0.7$, while at higher energies, the radiating electrons will have lost much of their energy already, causing the curve to steepen to $\alpha > 1$ after a break frequency $\nu_{\rm break}$ which decreases in inverse proportion to age of the halo. Figure 3.8b may have such a break around 1 GHz, which would correspond a halo age of a few 10^7 years; see [Pacholczyk 1977]. This appears to be rather young, indicating recent re-acceleration of the radiating particles. However, the feature does not appear to be compact enough to be associated with a cluster-merger-induced shock that might provide such acceleration; also it is not associated with a bright point-like radio source, like the one seen in the Coma halo, which could provide fresh, relativistic particles. A more likely scenario may be that the cluster-centre source has two components: a truly steep-spectrum halo which dominates at low frequencies (this appears consistent with the strong, much more extended emission in the WENSS map; see Figure 3.6b), and another underlying extended source, possibly a gravitationally lensed "radio ring" with $\alpha \approx 0.7$, which becomes apparent at higher frequencies.

3.2.2 Abell 665

Abell 665, at $z = 0.182$, is probably the second-best-studied cluster in terms of S–Z analyses, after Abell 2218. Deep VLA data at 1.4 GHz and 5 GHz is available to study the radio source environment [Moffet & Birkinshaw 1989][Grainge 1996][Lefebvre 1994], and show the existence of an extended cluster-centre source; see Figure 3.9a. Comparison to the 330 MHz WENSS map (Figure 3.9b) shows that the cluster-centre emission is dominated by a steep-spectrum component at frequencies below 1 GHz, which seems likely to be a merger-induced radio halo. X-ray temperature measurements with ASCA show the cluster to be quite hot, with $T_e = 9.03^{+0.35}_{-0.32}$ keV [Allen & Fabian 1998]; further low-resolution ASCA measurements shows an unusally sharp temperature drop in the outer periphery (the decrease is to 2 keV at 1 Mpc from cluster centre) [Markevitch 1996], which would be expected in a

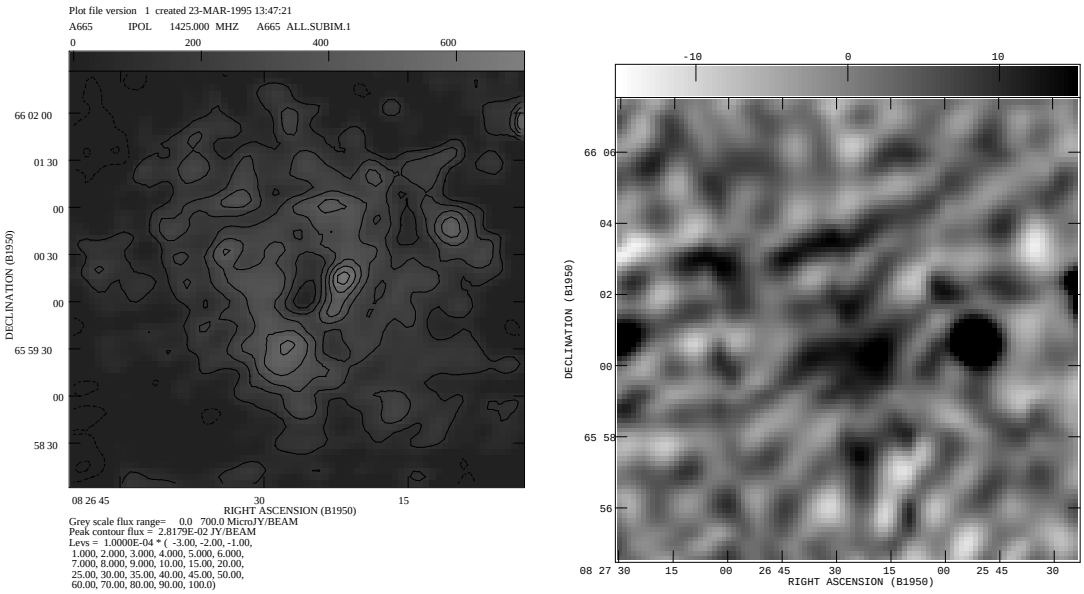

(a) (b)

Fig. 3.9: Lower-frequency maps of the Abell 665 cluster-centre halo. (a) VLA data at 1.4 GHz of central region, from [Grainge 1996]. (b) 330 MHz WENSS map (note: maps on different scales).

recently merged cluster. In addition, the strongly distorted, egg-shaped X-ray map of Abell 665, taken with the ROSAT PSPC detector, advertises recent merger activity. After the initial removal of two radio sources, the 35×12 hours of RT data show a tear-drop-shaped S–Z shadow on 0–1 kλ baselines [deepest decrement: $-450\pm90\,\mu\mathrm{Jy\,beam^{-1}}$], shown in Figure 3.10a. Such a shape would be expected if a merger-induced radio halo has filled in the western side of an initially elliptical S–Z shadow.

The existence of several lower frequency maps allows for more careful source subtraction. Four more non-central sources of flux 200 μJy, match sources in the 1.4 GHz map; their removal deepens the 0–1 kλ decrement to $-600\,\mu\mathrm{Jy\,beam^{-1}}$, but does not change the hole's distorted shape. To finish the radio source subtraction, the cluster-centre halo must be separated from the S–Z hole and removed, as described in Section 2.4.

With the halo subtracted, the S–Z hole re-claims its oval shape, matching the X-ray map, as shown in Figure 3.10b, and has a deepest decrement on $-560\,\mu\mathrm{Jy\,beam^{-1}}$. The scale factor obtained in the halo/hole separation is $r_{50}\equiv1/\sqrt{h_{50}}=1.11\pm0.23\,(9.03\,\mathrm{keV}/k_\mathrm{B}T_e)$, which corresponds to a Hubble constant estimate of $H_0=41^{+10}_{-7}\,\mathrm{km\,s^{-1}Mpc^{-1}}\times(\mathrm{k_BT_e}/9.03\,\mathrm{keV})^2$. Note that the error on the scale factor due to purely statistical noise would be 0.181; the increased error is due to the uncertainty in the separation of the halo and the hole.

The halo, shown in Figure 3.11a is fitted to have flux $520\pm70\,\mu$Jy and FWHM 50 arcsec, and is coincident with a source seen at 5 GHz [Lefebvre 1994]. A plot of the radio flux vs. frequency is shown in Figure 3.11b, with the lower frequency measurements corrected to only include flux in a FWHM 50 arcsec beam. The plot is consistent with a cluster centre source with both a steep spectrum

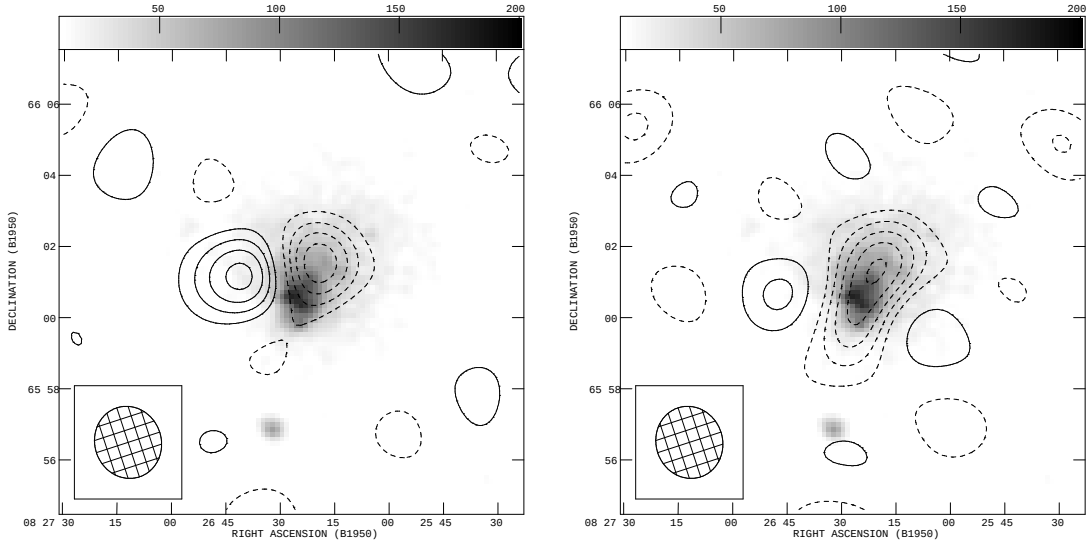

(a) (b)

Fig. 3.10: 0–1 kλ point-source-subtracted and CLEANed maps of Abell 665 S–Z hole (a) before halo removal, and (b) after halo removal. Contour spacing: $100\,\mu\mathrm{Jy\,beam^{-1}}$. Greyscale is the ROSAT PSPC X-ray map.

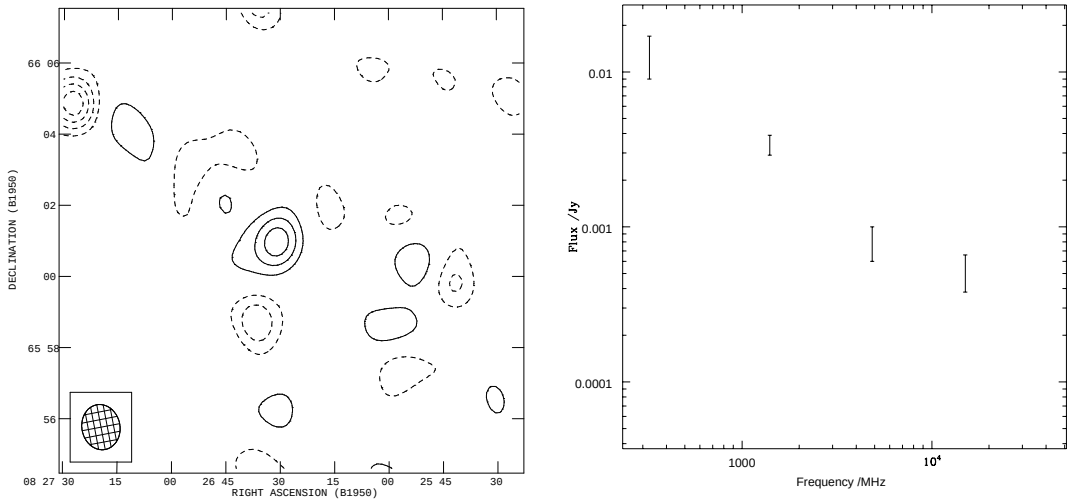

(a) (b)

Fig. 3.11: The Abell 665 halo. (a) Image (contour spacing: $80\,\mu\mathrm{Jy\,beam^{-1}}$) obtained by CLEANing 0–2 kλ map of RT data after removing all non-central sources as well as a model of the S–Z hole ($H_0 = 40\,\mathrm{km\,s^{-1}Mpc^{-1}}$). (b) "Spectrum" of the halo source; the flattening at higher frequencies may indicate the presence of two components (see text for details).

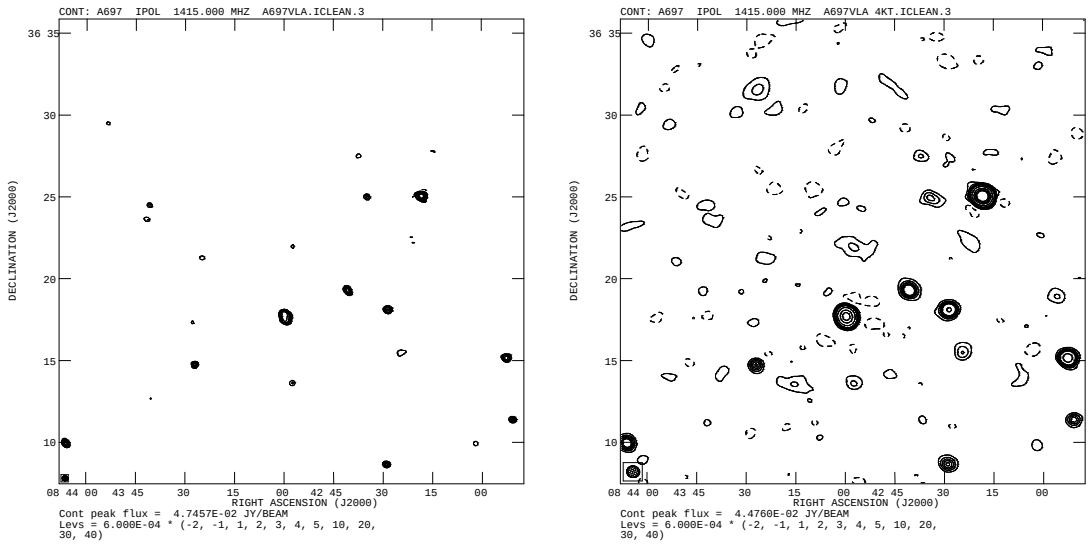

(a) (b)

Fig. 3.12: 1.4 GHz VLA map of the Abell 697 cluster region. (a) all-baseline CLEANed map, and (b) data with exponential *u-v* taper ($1/e$ at $4\,k\lambda$) applied to accent the shorter baselines, revealing the extended source in the cluster centre.

merger-induced halo component, and an extended flatter spectrum ($\alpha < 1$) component that becomes apparent at higher frequencies. The latter appears to have a ring-like structure, as shown in Figure 3.9; it may be a gravitationally lensed radio ring.

3.2.3 Abell 697

A ROSAT HRI map is available for Abell 697 at $z = 0.282$, as well as an ASCA temperature of $8.0^{+0.5}_{-0.4}$keV [Miyoshi 1999]. With 42×12 hours of RT data, the 0–1 kλ map of Abell 697 shows a decrement of $-500 \pm 100\,\mu\mathrm{Jy\,beam^{-1}}$, shown in Figure 3.13a, after subtraction of six point sources, each of which is at least 3 arcminutes away from the pointing centre. However, 1.4 GHz VLA data obtained by the Cavendish group indicate the presence of an extended radio source with total flux of approximately 2.8 ± 0.7 mJy present at the cluster centre, spread over 2 arcminutes in the east-west direction; it is clearly visible when the VLA data is weighted to enhance shorter baselines, as seen in Figure 3.12. A similarly extended source is seen in the 330 MHz WENSS map, with total flux of approximately 20 mJy.

Without attempting a removal of this halo in the RT data, the Hubble constant determination varies depending on which baselines of the RT data are used: $H_0 = 110^{+35}_{-24}\,\mathrm{km\,s^{-1}Mpc^{-1}}$ using the shortest baseline only (640-870 λ), while $H_0 = 66^{+18}_{-11}\,\mathrm{km\,s^{-1}Mpc^{-1}}$ using all baselines up to 10 kλ. The inconsistency derives from the mismatch between the X-ray model of the gas and the shape of the S–Z shadow, which appears to be contaminated with the radio halo.

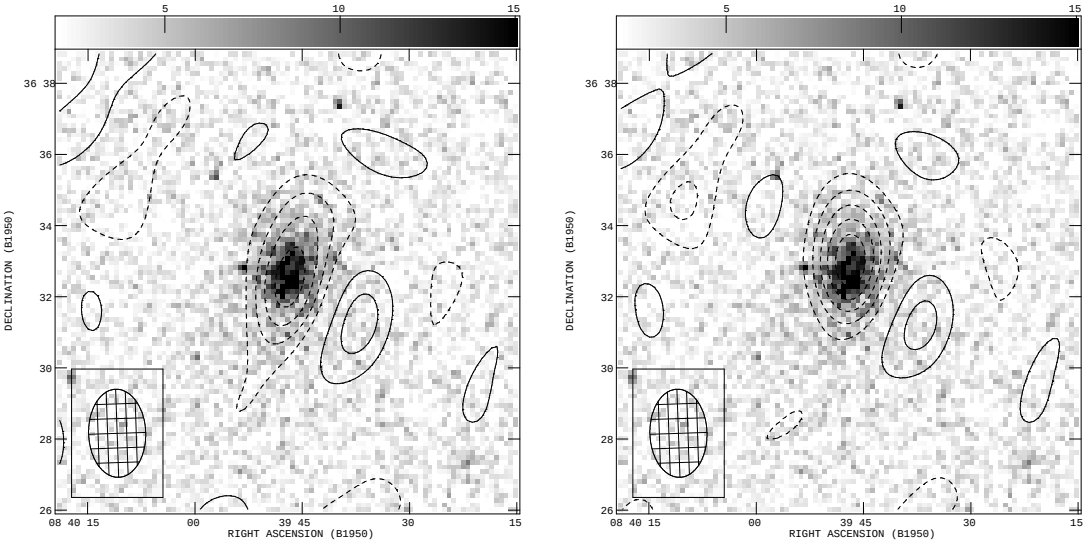

(a) (b)

Fig. 3.13: 0–1 kλ point-source-subtracted and CLEANed maps of Abell 697 S–Z hole (a) before halo removal, and (b) after halo removal. Contour spacing: $100\,\mu\mathrm{Jy\,beam^{-1}}$. Greyscale is the ROSAT HRI X-ray map.

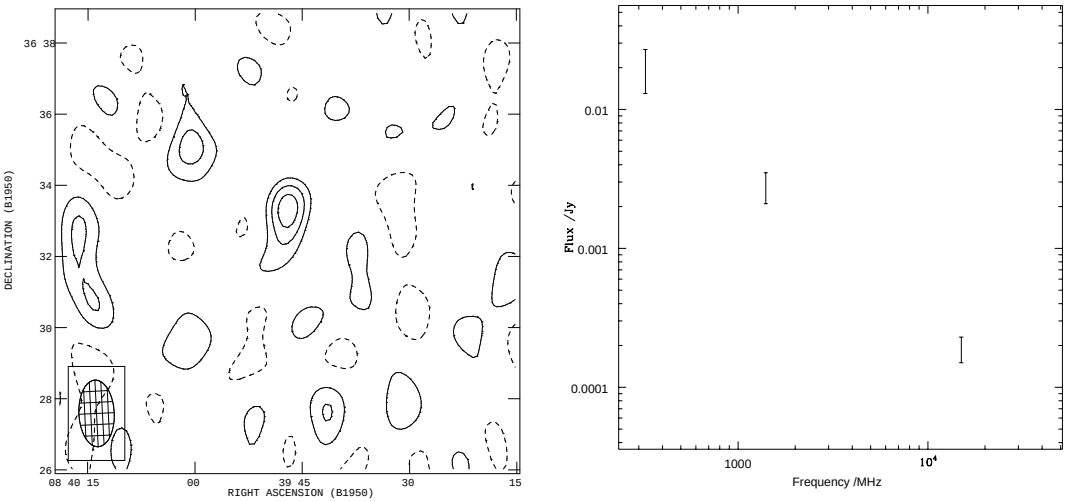

(a) (b)

Fig. 3.14: The Abell 697 halo. (a) Image (contour spacing: $50\,\mu\mathrm{Jy\,beam^{-1}}$) obtained by CLEANing 0–2 kλ map of RT data after removing all non-central sources as well as a model of the S–Z hole ($H_0 = 65\,\mathrm{km\,s^{-1}Mpc^{-1}}$). (b) "Spectrum" of the halo source.

A fit of the RT data for a radio halo yields a roughly circular $190 \pm 40 \mu$Jy source with FWHM 30 arcsec, located half an arcminute north of the cluster centre, in agreement with the source location on the 1.4 GHz VLA map. The halo/hole separation yields the scale factor of the S–Z model to be $r_{50} \equiv 1/\sqrt{h_{50}} = 0.87 \pm 0.13\,(8.0\,\mathrm{keV}/k_B T_e)$, corresponding to $H_0 = 66^{+25}_{-16}\,\mathrm{km\,s^{-1}Mpc^{-1}} \times (\mathrm{k_B T_e}/\,8.0\,\mathrm{keV})^2$. Note that the error on H_0 is larger than the previous estimates, due to the uncertainty in the halo/hole separation. Removal of the halo leads to a $-640\,\mu\mathrm{Jy\,beam^{-1}}$ S–Z hole in the 0–1 kλ map, whose shape agrees with the X-ray gas, as shown in Figure 3.13b.

The presence of the halo, shown in Figure 3.14a, may indicate a recent merger. The ROSAT HRI X-ray map is unfortunately not sensitive enough to show merger activity unequivocally, but the gas shape is strongly elongated, with an axial ratio of 1.4. The total flux values at 330 MHz, 1.4 GHz, and 15 GHz are consistent with a "steep" spectrum of $\alpha = 1.0 - 1.3$, as would be expected in a merger-induced halo; the spectrum is plotted in Figure 3.14b. However, without better information about the width of the halo at the different frequencies, it is difficult to rule out whether part of the halo may have a flatter spectrum.

3.2.4 Abell 773

For the cluster Abell 773 at $z = 0.217$, an HRI ROSAT map is available, as well as an ASCA temperature of 8.7 ± 0.4 keV [Miyoshi 1999]. Deep 1.4 GHz VLA data obtained by the Cavendish group show the radio environment around A773 to have a complex structure, with a ring of sources distributed in a diffuse halo around the cluster centre, as shown in Figure 3.15. With 30×12 hours of data, the 0–1 kλ baselines show a deep $-700 \pm 90\,\mu\mathrm{Jy\,beam^{-1}}$ S–Z decrement as shown in Figure 3.16a, after six point sources near the centre are removed.

A preliminary fit to the Hubble constant, without any attempt at removing any residual extended flux, then yields $H_0 = 61^{+19}_{-13}\,\mathrm{km\,s^{-1}Mpc^{-1}} \times (\mathrm{k_B T_e}/\,8.7\,\mathrm{keV})^2$.

To complete the source subtraction, some of the non-central extended residuals located 2 arcminutes from the cluster centre are modeled as Gaussians and removed (see Table 3.4 for details); this subtraction changes the 0–1 kλ decrement to $-400\,\mu\mathrm{Jy\,beam^{-1}}$. Finally, the extended flux near the centre is fitted simultaneously with the hole, yielding a fitted halo of flux $500 \pm 70 \mu$Jy, FWHM 40 arcsec, located 40 arcseconds southwest of the cluster centre, as shown in Figure 3.16b. With the halo removed, the 0–1 kλ decrement is then $-610\,\mu\mathrm{Jy\,beam^{-1}}$, shown in Figure 3.17. The fitted S–Z scale factor is $r_{50} \equiv 1/\sqrt{h_{50}} = 0.87 \pm 0.13\,(8.7\,\mathrm{keV}/k_B T_e)$, corresponding to $H_0 = 64^{+42}_{-21}\,\mathrm{km\,s^{-1}Mpc^{-1}} \times (\mathrm{k_B T_e}/\,8.0\,\mathrm{keV})^2$. Note that although the hole/halo separation does not dramatically change the H_0 value from the one above, the error bars now properly reflect the uncertainties arising from the removal of the extended radio flux.

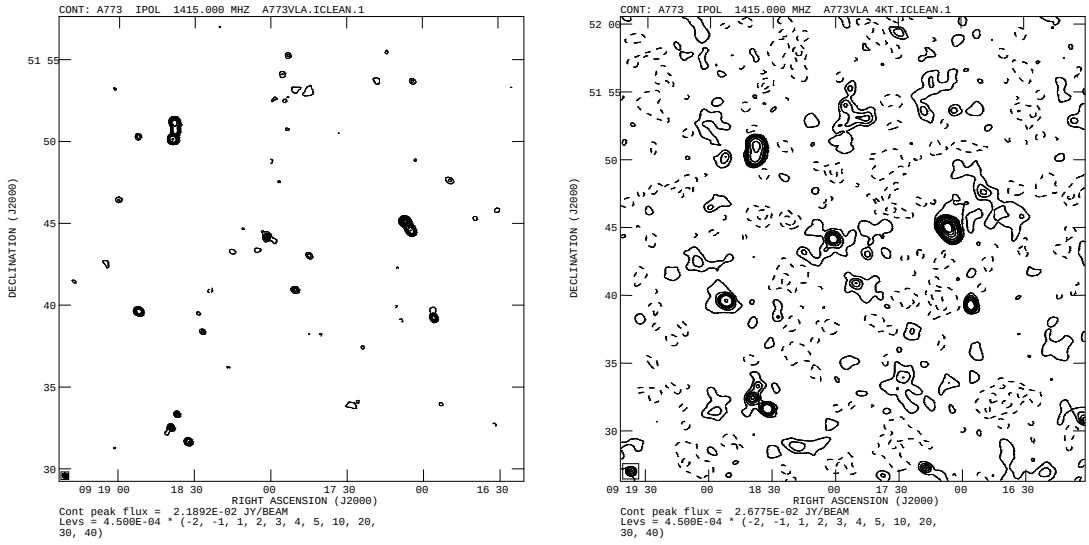

(a) (b)

Fig. 3.15: 1.4 GHz VLA map of the Abell 773 cluster region. (a) all-baseline CLEANed map, and (b) data with exponential *u-v* taper ($1/e$ at $4\,\mathrm{k}\lambda$) applied to accent the shorter baselines, revealing the extended source in the cluster centre.

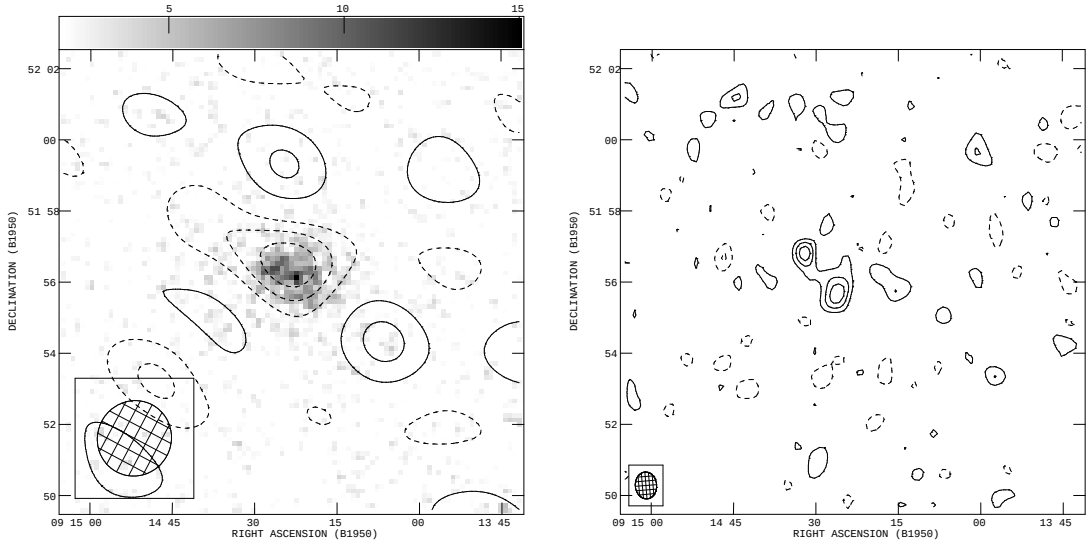

(a) (b)

Fig. 3.16: (a) 0–1 kλ point-source-subtracted and CLEANed map (contour spacing: $85\,\mu\mathrm{Jy\,beam^{-1}}$) of Abell 773 S–Z hole before halo removal, on ROSAT HRI map (greyscale). (b) All-baseline map of Abell 773 RT data before any source subtraction, with a model of the S–Z effect removed, showing the complex cluster-centre source (contour spacing: $50\,\mu\mathrm{Jy\,beam^{-1}}$) .

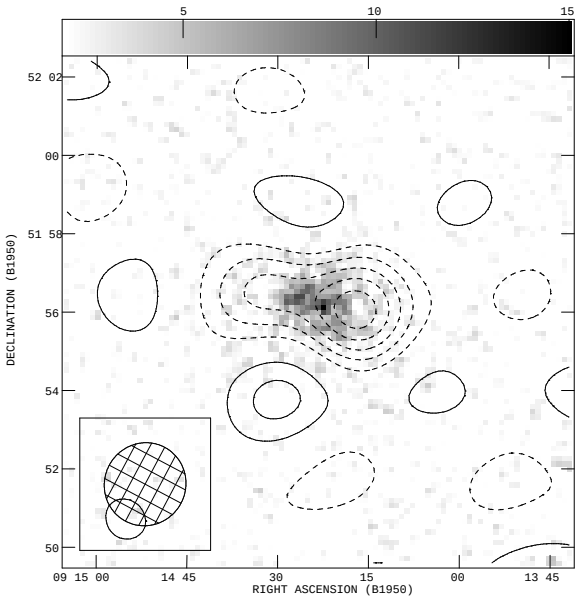

Fig. 3.17: 0–1 kλ point-source-subtracted and CLEANed map of Abell 773 S–Z hole after halo removal (contour spacing: $85\,\mu\mathrm{Jy\,beam^{-1}}$), on ROSAT HRI map (greyscale).

3.2.5 Abell 1413

Both ROSAT PSPC and ROSAT HRI maps are available for Abell 1413, at $z = 0.143$, and show that the cluster gas contains a cooling flow. Allen and Fabian have simultaneously analyzed the ASCA and ROSAT HRI data to determine the A1413 temperature with two models; one model assumes the gas is isothermal, while the other one fits the cool component separately, with the fraction of total emission from the cool gas normalised by the cooling flow's fitted mass deposition rate [Allen & Fabian 1998]. The results are $7.54^{+0.29}_{-0.27}$ keV (isothermal fit including cooling flow) and $8.5^{+1.3}_{-0.8}$ keV (isothermal fit excluding cooling flow) respectively.

After initial subtraction of four radio sources, the 0–1 kλ map of 64×12 hours of RT data of Abell 1413 shows a weak decrement, $-300 \pm 110\,\mu\mathrm{Jy\,beam^{-1}}$. The low signal-to-noise makes CLEANing difficult, as seen in Figure 3.18a. One of the removed point sources is right at the cluster centre, and coincides with the cluster's large central galaxy as well as the cooling-flow seen in the X-rays; there is a good possibility that there is a Perseus-like "mini-halo" at the centre; unfortunately, available VLA maps do not have the sensitivity to check for extended flux at lower frequencies.

An 8.4 GHz VLA map in [Grainge 1996] allows for the subtraction of five more sources; their removal slightly enhances the 0–1 kλ decrement, to $-460\,\mu\mathrm{Jy\,beam^{-1}}$. To complete the source subtraction, the mini-halo must be removed as well. It turns out that the extended emission is compact enough that it can be seen as a group of three central, faint (but significant) point-like sources on longer baselines.[3] After removal of these sources (totaling 210 μJy in flux), an S–Z hole with flux

[3] Simultaneous halo/hole fits were tried first before removing these three central point sources. Rather than finding a

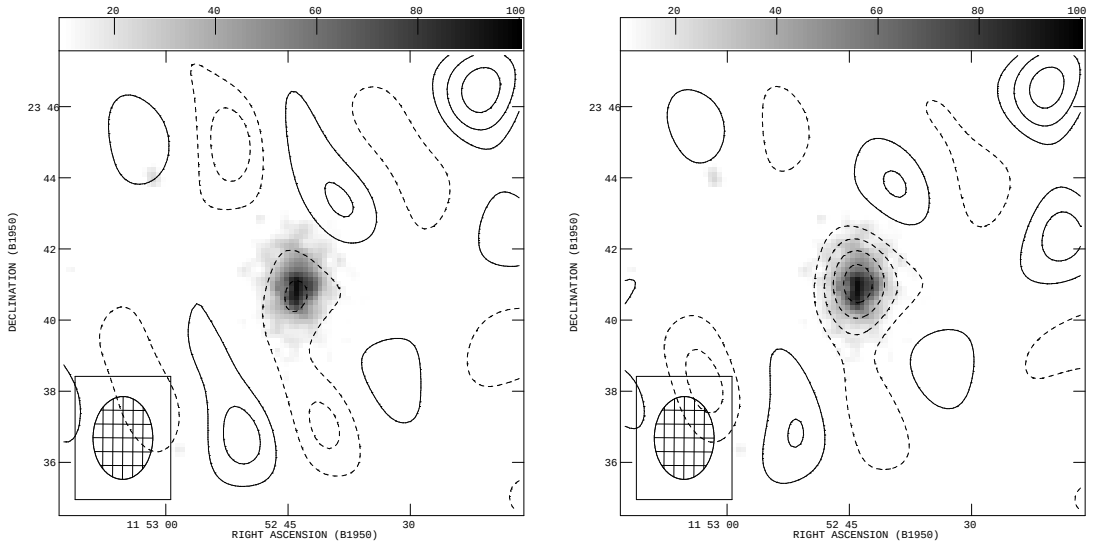

(a) (b)

Fig. 3.18: 0–1 kλ point-source-subtracted and CLEANed maps of Abell 1413 S–Z hole (a) before halo removal, and (b) after removal of halo (modelled as a set of faint central point sources; see text). Contour spacing: $100\,\mu$Jy beam^{-1}. Greyscale is the ROSAT PSPC X-ray map.

$-560\,\mu$Jy beam^{-1} on 0–1 kλ baselines was left, shown in 3.18b. The scale factor of the S–Z model (which is based on a King-profile fit of the X-ray map excluding the cluster's central cooling-flow region) is fitted to be $r_{50} \equiv 1/\sqrt{h_{50}} = 1.14 \pm 0.12\,(8.5\,\mathrm{keV}/k_{\mathrm{B}}T_e)$. This corresponds to an estimate of $H_0 = 39^{+10}_{-7}\ \mathrm{km\,s^{-1}Mpc^{-1}} \times (\mathrm{k_B T_e}/\,8.5\,\mathrm{keV})^2$.

As a systematic check, the fit is re-done with an S–Z model based on a King-profile fit of the X-ray map including the cooling-flow region; this yields $r_{50} \equiv 1/\sqrt{h_{50}} = 0.97 \pm 0.11\,(7.54\,\mathrm{keV}/k_{\mathrm{B}}T_e)$ and $H_0 = 53^{+16}_{-11}\,\mathrm{km\,s^{-1}Mpc^{-1}} \times (\mathrm{k_B T_e}/\,7.54\,\mathrm{keV})^2$, agreeing well with the previous estimate. Note that both of these results also agree within 1-σ errors with the previous analysis of the same RT data set by Grainge *et al.*, which found $H_0 = 57^{+23}_{-16}\,\mathrm{km\,s^{-1}Mpc^{-1}}$ [Grainge 1999]; in that analysis, point source fluxes were obtained with a looser long-baseline cut [> 1.5 kλ, rather than my stricter > 2 kλ cut], and uncertainties due to residual extended halo flux were assessed after a fit of the S–Z data.

3.2.6 Abell 1704

Like Abell 1413, the cluster Abell 1704 ($z = 0.220$) has a cooling-flow. Its ROSAT HRI map and ASCA spectrum were fit by Allen and Fabian [Allen & Fabian 1998] to yield two temperature estimates, $4.73^{+0.38}_{-0.33}$ keV (isothermal fit including cooling flow) and $5.7^{+3.5}_{-1.3}$ keV (isothermal fit excluding cooling flow).

smooth halo extended over 30 arcseconds, the halo fit tended to quickly converge to the point-like compact regions, so it was concluded that simply modelling the halo as a set of point sources was reasonable.

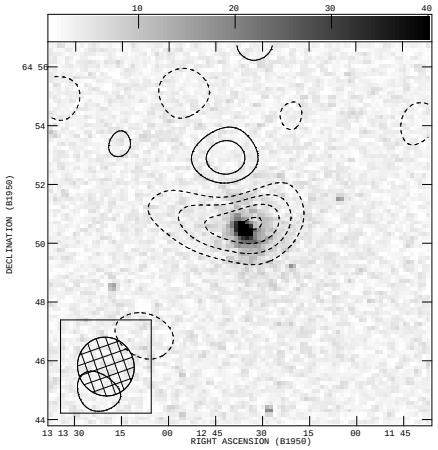

Fig. 3.19: 0–1 kλ point-source-subtracted and CLEANed maps of Abell 1704 (contour spacing: 85 μJy beam^{-1}), on ROSAT HRI X-ray map (greyscale).

The 24×12 hours RT map of Abell 1704 shows a $-430 \pm 85\,\mu$Jy beam^{-1} decrement on 0–1 kλ baselines (see Figure 3.19), after the subtraction of four sources. Two of the sources of flux 100 μJy each are within an arcminute of the cluster centre, and their fluxes are well-constrained by the longer baseline (> 2 kλ) information; there is no evidence for any residual extended emission obscuring the S–Z decrement.

Fitting an isothermal King model, based on a fit to the X-ray map excluding the central cooling-flow region, to the source-subtracted RT visibilities yields a scale factor $r_{50} \equiv 1/\sqrt{h_{50}} = 0.87 \pm 0.22\,(5.7\,\mathrm{keV}/k_\mathrm{B}T_e)$ and $H_0 = 67^{+52}_{-24}$ km s^{-1}Mpc^{-1} $\times$ $(\mathrm{k_B T_e}/\,5.7\,\mathrm{keV})^2$. As a systematic check, the fit is repeated with a King model which was fitted to the full X-ray map, including the cooling-flow, giving a nearly identical result $r_{50} \equiv 1/\sqrt{h_{50}} = 0.86 \pm 0.22\,(4.73\,\mathrm{keV}/k_\mathrm{B}T_e)$, and $H_0 = 68^{+52}_{-24}$ km s^{-1}Mpc^{-1} $\times$ $(\mathrm{k_B T_e}/\,4.73\,\mathrm{keV})^2$..

3.2.7 Abell 1914

A ROSAT PSPC map is available for Abell 1914 ($z = 0.171$), as well as an ASCA temperature estimate of 8.56 ± 0.65 keV [Miyoshi 1999]. Deep 1.4 GHz VLA data, shown in Figure 3.20a, reveals the presence of an extended radio halo with integrated flux of 50 mJy at the cluster centre. The presence of the halo is not surprising; the X-ray image shows the gas to be quite distorted, indicating a recent cluster merger. In addition, the POSS image (Figure 3.20b) shows clearly that Abell 1914 is composed of two merging systems.

Despite the strong presence of a radio halo, the 19×12 hours of data on Abell 1914 provide a tolerable constraint on H_0, not only because the S–Z shadow of this particularly hot (10 keV) cluster is deep, but also because the halo is well-displaced from the cluster gas centroid. After subtraction of nine faint, non-central point sources with matches in the VLA map, there is a deep S–Z decrement of

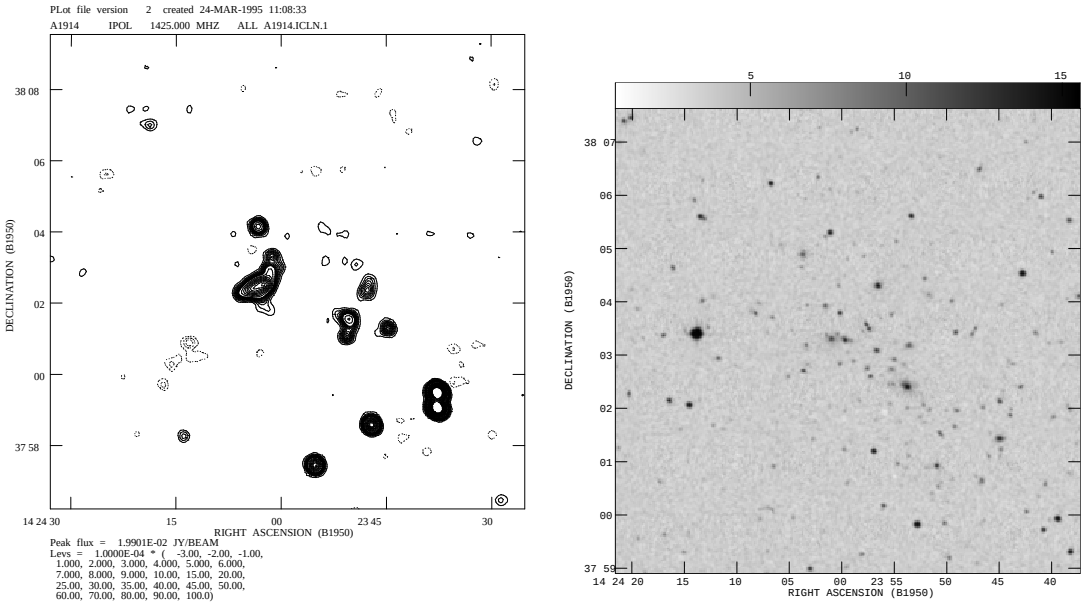

(a) (b)

Fig. 3.20: Indications of a recent merger in Abell 1914. (a) 1.4 GHz VLA map showing extended cluster-centre flux, most probably a merger-induced radio halo. (b) POSS image of A1914, indicating the presence of two merging sub-systems with separate dominant galaxies.

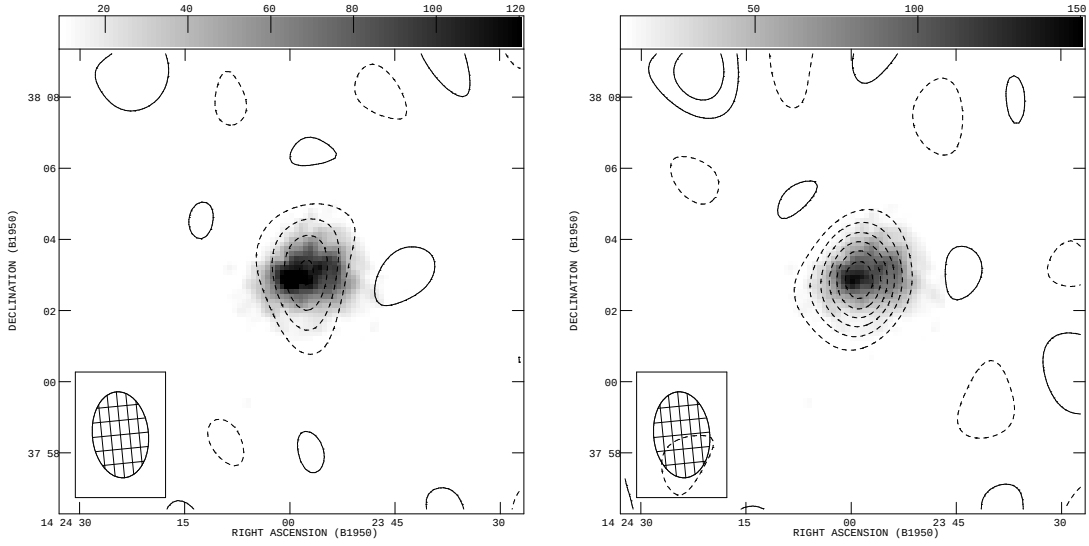

(a) (b)

Fig. 3.21: 0–1 kλ point-source-subtracted and CLEANed maps of Abell 1914 S–Z hole (a) before halo removal, and (b) after halo removal. Contour spacing: 120 μJy beam^{-1}. Greyscale is the ROSAT PSPC X-ray map.

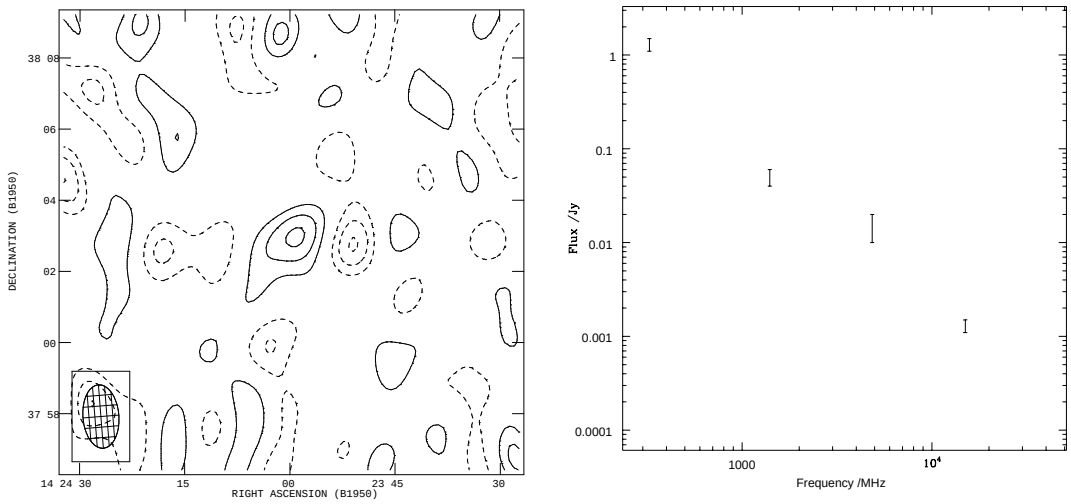

(a) (b)

Fig. 3.22: The Abell 1914 halo. (a) Image (contour spacing: $60\,\mu$Jy beam^{-1}) obtained by CLEANing 0–2 kλ map of RT data after removing all non-central sources as well as a model of the S–Z hole ($H_0 = 70\,\mathrm{km\,s^{-1}Mpc^{-1}}$). (b) "Spectrum" of the halo source (see text for details).

$-740 \pm 120\,\mu$Jy beam^{-1} on 0–1 kλ baselines, displaced east of the X-ray centroid, as shown in Figure 3.21a.

Because the radio halo is so bright, it needs to be treated carefully to properly separate the halo from the S–Z hole. It is extended over two arcminutes south-west of the cluster centre; the off-centre part is modelled as a $340\,\mu$Jy Gaussian with 70 arcsec FWHM located at a displacement of (90,-60) arcsec from the RT pointing centre. The remainder of the halo is correlated with the S–Z hole, so its flux must be fitted simultaneously with a scaled version of the S–Z model obtained from the X-ray data. This fit finds the second, central component of the halo to have flux $1000 \pm 120\mu$Jy source, with FWHM=90 arcsec directly at the pointing centre. The halo, shown in Figure 3.22, has a steep spectrum,as would be expected of a merger-induced radio halo. The total halo flux, taken from 330 MHz WENSS, 1.4 GHz VLA, and 5 GHz Greenbank maps is plotted as a function of frequency in Figure 3.22b. All the data points appear fairly consistent with the halo having a steep spectral index of $\alpha \approx 1.8$.

The halo removal yields a properly centred S–Z shadow, shown in Figure 3.21b with fitted scale factor $r_{50} \equiv 1/\sqrt{h_{50}} = 0.84 \pm 0.21\,(8.56\,\mathrm{keV}/k_\mathrm{B}T_e)$. The corresponding Hubble constant estimate is $H_0 = 71^{+55}_{-25}\,\mathrm{km\,s^{-1}Mpc^{-1}} \times (\mathrm{k_B T_e}/8.56\,\mathrm{keV})^2$; the error on this estimate takes into account the uncertainty in the halo fit, which turns out to double the error due to intrinsic statistical noise. Checks on modifying the X-ray fit have been made, using a King profile model with $\beta = 0.90$ instead of the usual $\beta = 0.65$; the central value of the H_0 estimate barely changes to $H_0 = 70^{+55}_{-25}\,\mathrm{km\,s^{-1}Mpc^{-1}}$, well within statistical error.

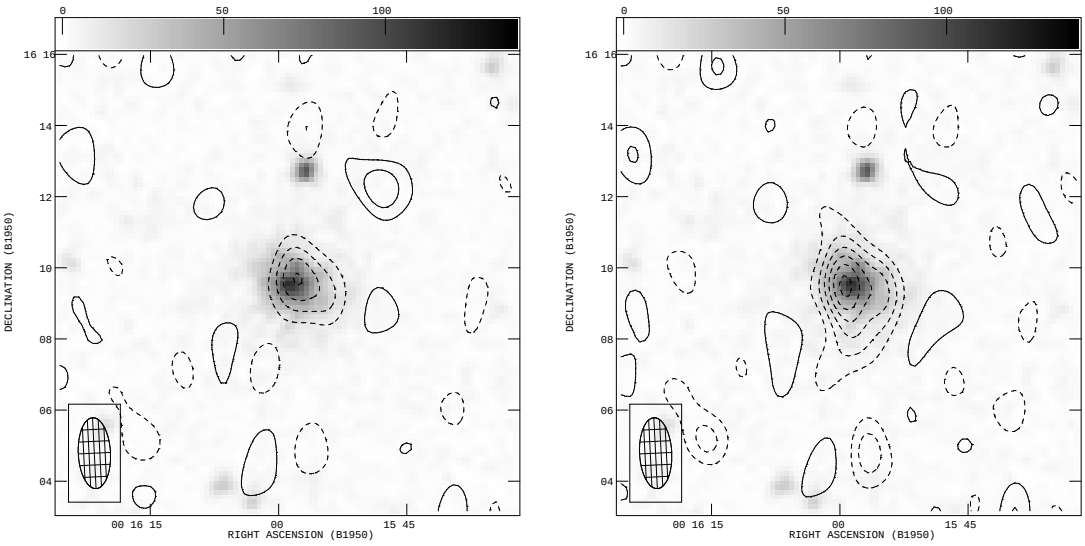

(a) (b)

Fig. 3.23: Point-source-subtracted and CLEANed maps (0–2 kλ) of the S–Z hole in CL0016+16 (a) before halo removal, and (b) after halo removal. Contour spacing: $60\,\mu$Jy beam^{-1}. Greyscale is the ROSAT PSPC X-ray map.

3.2.8 CL0016+16

The high-redshift cluster CL0016+16 at $z = 0.546$ has been well-studied by other groups. Both ROSAT PSPC and ROSAT HRI images are available, and an ASCA temperature of $7.55^{+0.7}_{-0.6}$ keV has been obtained [Hughes & Birkinshaw 1998-2].

The Ryle Telescope has taken 81×12 hours of data at the central pointing of CL0016+16 as well as 7×12 hours each at six pointings offset from the centre by one arcminute. The field-of-view has a fairly clean radio source environment, with two radio sources, matching sources in a deep VLA observation [Grainge 1996], subtracted separately from each pointing's data sets.

The 0–2 kλ baseline map, shown in Figure 3.23a, has good signal-to-noise, and shows a deepest decrement of $-240\pm40\,\mu$Jy beam^{-1}, and an integrated flux of approximately $-540\pm80\,\mu$Jy beam^{-1}. On comparison to the X-ray map, it appears as if some residual positive flux at the western end of the cluster is pushing the S–Z decrement east of the X-ray gas. Indeed, VLA observations at 1.4 GHz show 2.7 ± 0.7 mJy radio emission associated with the cluster centre [Moffet & Birkinshaw 1989]; a correction for a possible halo in the RT data appears to be necessary.

A simultaneous fit of a halo and a scaled S–Z model to source-subtracted data from all pointings with appropriate primary beam corrections for the offset pointings yields an elliptical halo with flux $320\pm100\,\mu$Jy, with width $110'' \times 40''$ FWHM at position angle $50\pm4°$, displaced by $(20\pm6, -22\pm6)$ arcseconds in (RA, Dec) from the cluster centre. This flux is consistent with a spectral index of $\alpha^{15}_{1.4} = 0.9\pm0.1$.

After the halo removal, the 0–2 kλ S–Z decrement, shown in Figure 3.23b, provides an interesting comparison with the X-ray image. There appear to be extensions of the S–Z image towards the north and towards the south, all the way to the edges of the RT primary beam, possibly indicating that CL0016+16 is part of a larger super-structure. Such deviations from a compact, round shape are also seen in the S–Z maps obtained with OVRO/BIMA data [Carlstrom 1996]. The extensions may point to poor clusters, like RXJ0018.3+1618, which is 9 arcminutes south of CL0016+16 and is at redshift $z = 0.541$ [Hughes & Birkinshaw 1998-1], and possibly a structure containing the X-ray source QSO0015+162 at $z = 0.554$, 3 arcminutes north of CL0016+16 [Margon 1983].

The S–Z model scale factor is fitted to be $r_{50} \equiv 1/\sqrt{h_{50}} = 0.94 \pm 0.05\,(7.55\,\mathrm{keV}/k_B T_e)$, corresponding to a Hubble constant estimate $H_0 = 57 \pm 5\,\mathrm{km\,s^{-1}Mpc^{-1}} \times (\mathrm{k_B T_e}/\,7.55\,\mathrm{keV})^2$. It should be remarked here that due to the excellent signal-to-noise in the high-statistics CL0016+16 data set as well as the displacement of the halo from the cluster centre, the uncertainty in the halo/hole separation actually adds less than 10% error to the instrinsic statistical error of the H_0 fit.

3.2.9 Even more clusters: Abell 611, Abell 990, Abell 1246, Abell 1423, Abell 1722, Abell 1995, Abell 2111, Abell 2259, and Zwicky 1883

Application of the point source subtraction methodology to RT data for several more clusters has revealed the presence of their Sunyaev-Zeldovich decrements. See Figures 3.24 for 0–1 λ point-source-subtracted images, overlaid on X-ray maps, where available. Detailed information on the significance of decrements is given in Table 3.2.9.

For several of the deeper images, including Abell 990 and Abell 1722, the presence of radio halos may be distorting the shapes of the S–Z holes. However, for these clusters, deep lower-frequency radio images have not yet been obtained to help constrain the location of any residual extended flux; in addition, X-ray temperatures and the astrometry of the emission maps are not yet finalized. When further radio and X-ray information becomes available, separation of extended cluster centre emission from the S–Z decrements, as well as further measurements of the Hubble constant, will become possible with these RT data sets.

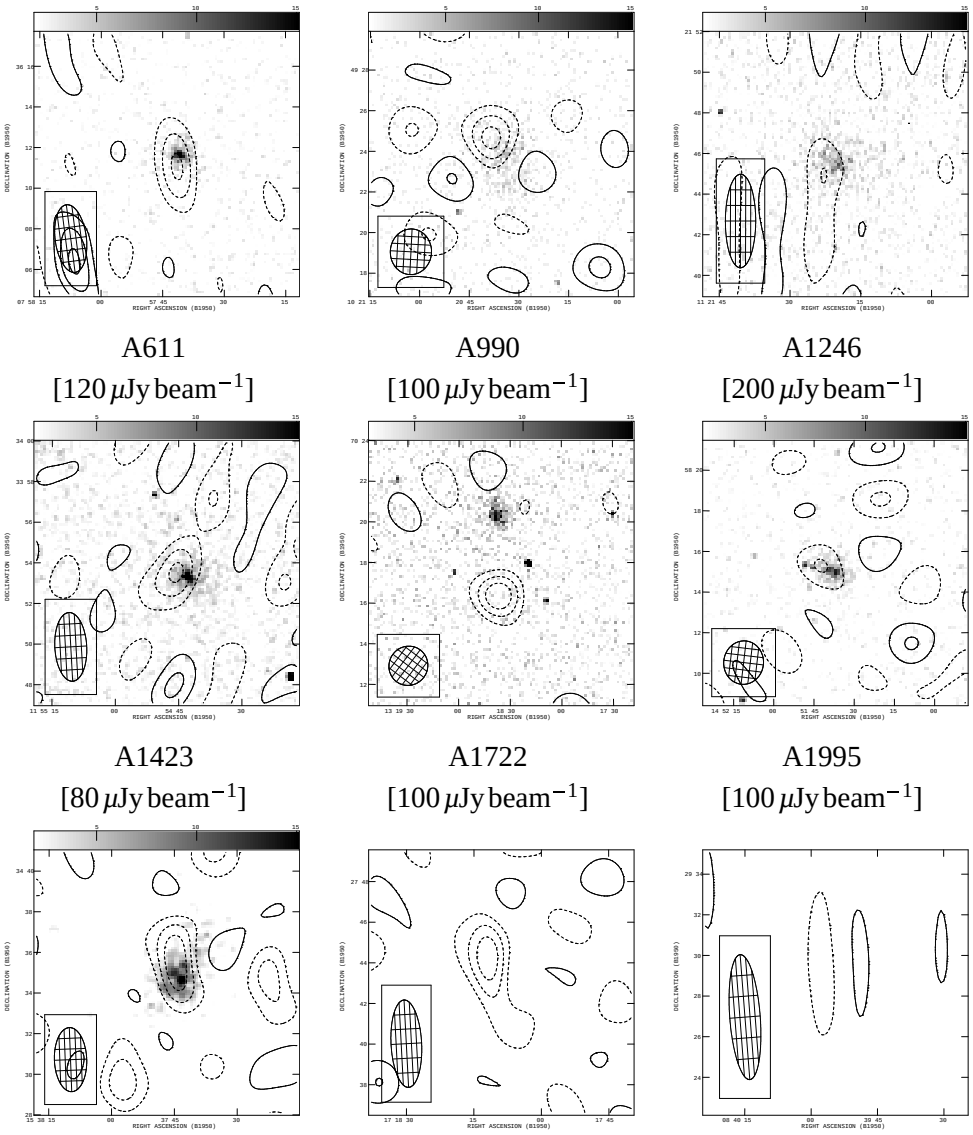

A611 [120 μJy beam^{-1}] | A990 [100 μJy beam^{-1}] | A1246 [200 μJy beam^{-1}]

A1423 [80 μJy beam^{-1}] | A1722 [100 μJy beam^{-1}] | A1995 [100 μJy beam^{-1}]

A2111 [80 μJy beam^{-1}] | A2259 [80 μJy beam^{-1}] | ZW1883 [120 μJy beam^{-1}]

Fig. 3.24: More S–Z holes. Cluster names [contour spacings] given under images, which are CLEANed maps of 0–1 λ baselines after initial point-source subtraction; in some cases, low signal-to-noise has made CLEANing difficult.

Cluster	z	No. days, Ryle data	No. sources subtracted	Short baseline [0–1 $k\lambda$] decrement, μJy
A611	0.288	16	1	-500 ± 140
A990	0.144	25	1	-440 ± 110
A1246	0.216	8	1	-580 ± 220
A1423	0.213	11	3	-400 ± 100
A1722	0.328	16	1	-510 ± 100
A1995	0.318	19	2	-320 ± 140
A2111	0.229	27	0	-360 ± 110
A2259	0.164	20	2	-390 ± 110
Zw1883	0.194	39	3	-400 ± 120

Tab. 3.1: More clusters showing significant S–Z decrements, which are ready for Hubble constant determinations when better lower-frequency radio maps and X-ray data become available.

HST cluster name	N_{gal}	rad ($''$)	m_c	RA ($^\circ$, J2000)	Dec ($^\circ$, J2000)	Ryle obs. time/12 hrs	No. srcs. subtr.	0–1 kλ r.m.s., μJy beam^{-1}
H035528+09435	13	10	22.25	58.86759	9.72577	13	1	300
H072442+60316	15	15	22.50	111.17674	60.52826	5	3	240
H115027+28496	11	10	23.75	177.61418	28.82765	10	5	270
H122332+15518	24	20	22.75	185.88700	15.86494	17	1	200
H123155+14153	47	30	23.75	187.98116	14.27305	16	0	240
H151940+23524	23	25	22.00	229.91835	23.87468	3	1	400
H215137+28590	14	15	22.50	327.90569	28.98339	3	1	400

Tab. 3.2: HST high-redshift candidates. Seven of the candidates for cluster/regions found in the Hubble Space Telescope Medium Deep Survey [see [Ostrander 1998]] have been observed with the Ryle Telescope. N_{gal} is number of galaxies found in a radius (rad, in arcsec); the brightest galaxy in the region is required to be faint, with magnitude $m_c > 22$. No Sunyaev–Zel'dovich shadows have been found; upper limits can be computed as approximately 3σ, from the 0–1 kλ r.m.s. estimates given below (the short-baseline beam has FWHM of 2 arcmin).

3.3 High-Redshift Candidates

The selection methods and the results of S–Z searches for high-*z* clusters are detailed in this section.

3.3.1 Optical Selection: Galaxy Overdensities from the Hubble Space Telescope

The HST Medium Deep Survey Cluster Sample is a list of 92 regions of the sky which have a statistically significant overdensity of optically-selected galaxies within circular radii of 10–30 arcsec [Ostrander 1998]. Seven of these regions have been observed by the Ryle Telescope. These particular regions are the ones in the HST-MDS list which have faint central galaxy magnitudes ($m_c > 22$) as well as large overdensities of neighbouring galaxies at fainter magnitude.

The Ryle Telescope has not been able to find S–Z effects in any of the observed regions; apparently the galaxy clusters/groups do not contain enough hot gas to produce strong S–Z shadows. The RT observations are summarized in Table 3.3. All of them produce 0–1 kλ maps that are consistent with the expected noise, which ranges from 200 μJy to 400 μJy in these observations. Of course, the fact that the newly developed source subtraction methods can yield a null result is a good check on it.

3.3.2 X-ray Selection: Distant X-ray Gas Concentrations

Of the several high-*z* clusters seen as faint but extended sources in the EINSTEIN EMSS list and the public-domain ROSAT detections, two appear to be rich enough and to have high enough declination to yield good S–Z measurements with the RT. One of them is CL0016+16.

The second, MS1137+6625 at z=0.78 [Donahue 1999], has been observed for 28 $\times$ 12hours with

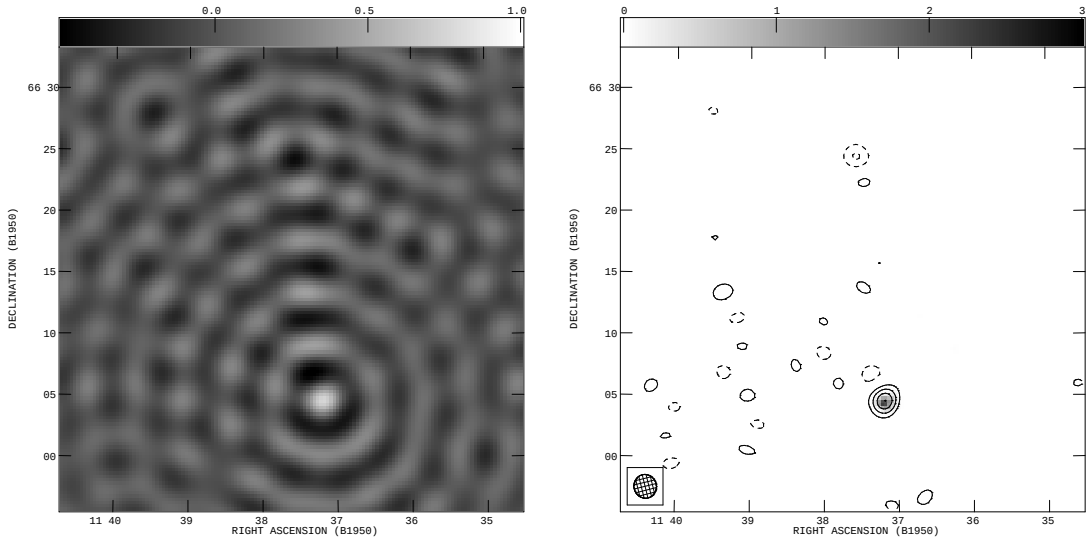

(a) (b)

Fig. 3.25: The S–Z hole of MS1137+6625 and 3C radio source. 0–1 kλ map (a) before CLEANing and (b) after CLEANing. Latter map has contour spacing 150 μJy beam^{-1}; greyscale is NVSS map.

the RT. The field-of-view is atypical; in addition to one easily removed nearby 400 μJy point source, there is an anomalous source 20 arcmin south of the pointing. Usually sources (with typical fluxes less than 2 mJy) so far away would be completely attenuated by the RT primary beam; however, this happens to be 3C263, with flux 3 Jy at 1.4 GHz.

Even without subtracting the 3C source, the S–Z hole is clearly visible on the map, as shown in Figure 3.25. To get a quantitative estimate of the S–Z hole depth, the source's 0–1 kλ flux, 600 μJy, is removed, leaving behind an equivocal -400 ± 80 μJy decrement centred on the X-ray cluster, shown in Figure 3.26a. The 0–2 kλ map, Figure 3.26b, also has very good signal-to-noise and shows the S–Z effect to have extensions leading away from the centre, giving the shadow a triangular shape. Such structure is not visible on the low-sensitivity X-ray map. Is this cluster part of a larger supercluster structure? Further deep S–Z mapping around the centre would surely give a clear answer.

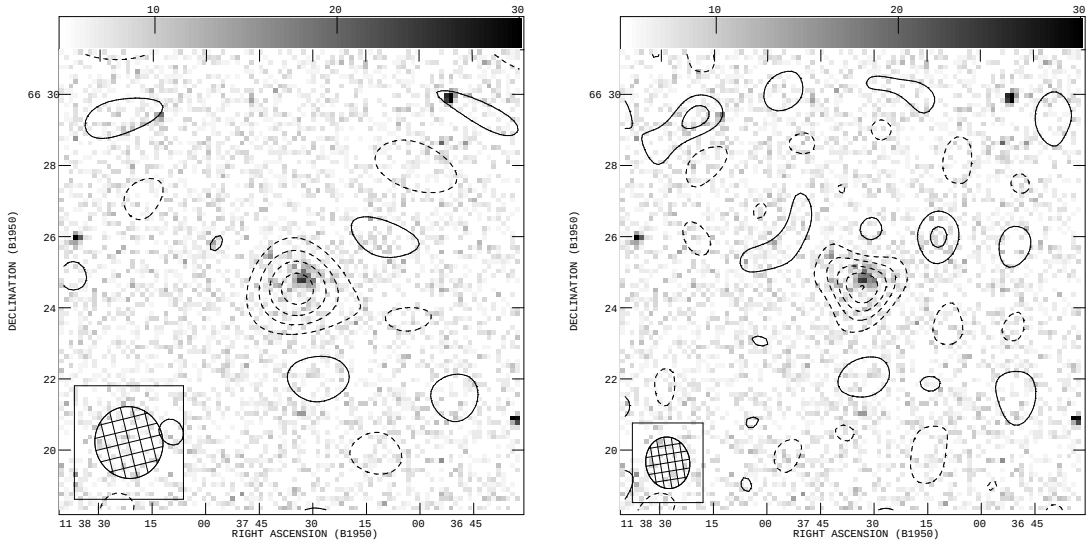

Fig. 3.26: Maps of the MS1137+6625 hole after removal of the 3C source and CLEANing. (a) 0–1 kλ map, with 60 μJy beam^{-1} contour spacing, and (b) 0–2 kλ map, with 60 μJy beam^{-1} contour spacing. Greyscale is ROSAT HRI map.

3.3.3 Radio Selection: Clusters of Radio Sources

The TEXOX list of candidates of possible high-redshift galactic clusters has been compiled by looking for statistically significant aggregates of sources in radio surveys [Rawlings 1999]. The RT has, so far, made maps of two of the TEXOX candidates, TEXOXL20 and TEXOXL21, after subtracting almost a dozen radio sources from each field-of-view. This large number of sources is more than twice the number seen in the other RT clusters' field-of-views, and almost ten times the number expected from source counts in regions free of clusters [Donnelly 1987]. The RT data shows strong S–Z effects in both regions, of $-320 \pm 65\,\mu$Jy and $-640 \pm 80\,\mu$Jy, respectively, indicating the discovery of new galactic clusters. See Figure 3.27 for the 0–1 kλ maps.

The 0–2 kλ maps of the two regions, shown in Figure 3.28, both appear to have odd double-structures. Any residual extended flux not removed in the source subtraction would lead to such distortions. However, without some model of the shape of the expected S–Z hole (as is available for the H_0 clusters), it is difficult to separate the S–Z effect from these extended sources. In any case, the extended sources required to produce the distortions appear to be located inside the S–Z hole itself. Removal of the source fluxes (estimated to be less than $150\,\mu Jy$ from the size of the distortions) would appear to enhance the hole, so the S–Z depths presented above should probably be considered slight underestimates.

Optical followup is being carried out by Rawlings to constrain the redshifts of the TEXOXL clusters [Rawlings 1999]. At present, an optical match to one of the radio sources in the TEXOXL20 region has been found with a redshift of $z \approx 0.8$. In addition, further TEXOX candidates are being observed by the Ryle Telescope, with promising results.

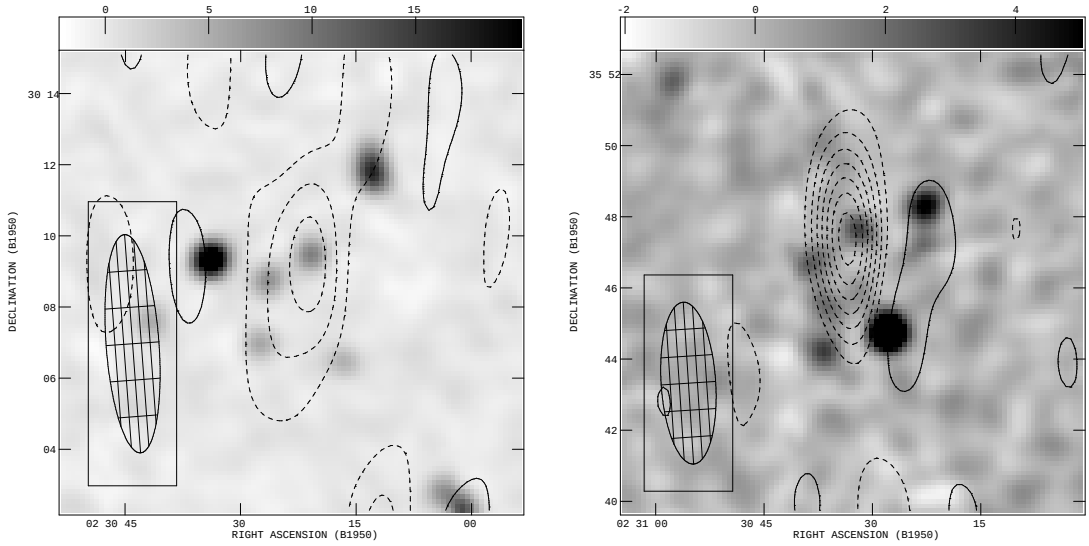

(a) (b)

Fig. 3.27: The S–Z effects in TEXOXL20 and TEXOXL21 regions. Shown are the CLEANed 0–1 kλ maps after point source subtraction.

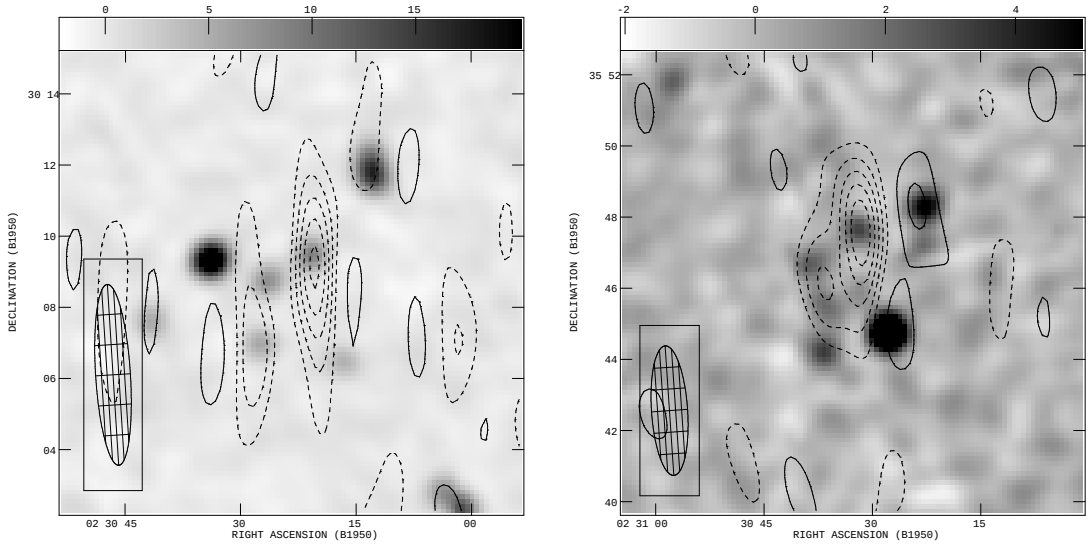

(a) (b)

Fig. 3.28: The S–Z effects in TEXOXL20 and TEXOXL21 regions. Shown are the CLEANed 0–2 kλ maps after point source subtraction.

Tab. 3.3: Initial point source subtraction in Abell 2218 at central and at six offset pointings. Locations are given relative to nominal cluster centre. When, a point source's distance from the actual pointing centre (also given) is less than four arcminutes, its flux can be accurately corrected for the primary beam attenuation.

Cluster	Src. No.	Location ($''$)	RA(1950)	Dec(1950)	Dist. ($''$)	Fitted Flux (μJy)	Corr. Flux (μJy)
A2218(C)	1	(-39 , 119)	$16^h35^m35.4^s$	$66°20^m46^s$	126	1080 ± 35	1617 ± 52
A2218(C)	2a	(128 , 97)	$16^h36^m3.3^s$	$66°20^m24^s$	161	1657 ± 35	3225 ± 68
A2218(C)	2b	(117 , 80)	$16^h36^m1.4^s$	$66°20^m7^s$	142	178 ± 35	298 ± 59
A2218(C)	3a	(-192 , 34)	$16^h35^m10.0^s$	$66°19^m21^s$	196	1790 ± 35	5010 ± 98
A2218(C)	3b	(-177 , 49)	$16^h35^m12.4^s$	$66°19^m36^s$	185	135 ± 35	332 ± 86
A2218(C)	3c	(-201 , 12)	$16^h35^m8.5^s$	$66°18^m59^s$	202	173 ± 35	524 ± 106
A2218(N)	1	(-37 , 120)	$16^h35^m35.7^s$	$66°20^m47^s$	155	1809 ± 106	3355 ± 197
A2218(N)	2	(130 , 97)	$16^h36^m3.6^s$	$66°20^m24^s$	120	2300 ± 106	3320 ± 153
A2218(N)	3	(-192 , 36)	$16^h35^m10.0^s$	$66°19^m23^s$	256	2017 ± 106	
A2218(NW)	1	(-38 , 120)	$16^h35^m35.5^s$	$66°20^m47^s$	128	1291 ± 105	1964 ± 160
A2218(NW)	2a	(130 , 97)	$16^h36^m3.6^s$	$66°20^m24^s$	103	2545 ± 105	3347 ± 138
A2218(NW)	2b	(-139 , 52)	$16^h35^m18.8^s$	$66°19^m39^s$	193	345 ± 105	935 ± 285
A2218(NW)	3	(-191 , 32)	$16^h35^m10.1^s$	$66°19^m19^s$	244	1143 ± 105	
A2218(SW)	1	(-39 , 117)	$16^h35^m35.4^s$	$66°20^m44^s$	173	997 ± 89	2184 ± 195
A2218(SW)	2	(130 , 97)	$16^h36^m3.6^s$	$66°20^m24^s$	149	2096 ± 89	3707 ± 157
A2218(SW)	3	(-192 , 33)	$16^h35^m10.0^s$	$66°19^m20^s$	253	1035 ± 89	
A2218(S)	1	(-38 , 119)	$16^h35^m35.5^s$	$66°20^m46^s$	183	730 ± 100	1767 ± 242
A2218(S)	2	(127 , 97)	$16^h36^m3.1^s$	$66°20^m24^s$	202	1092 ± 100	3291 ± 301
A2218(S)	3	(-192 , 35)	$16^h35^m10.0^s$	$66°19^m22^s$	215	1530 ± 100	5522 ± 361

continued on next page

continued from previous page

Cluster	Src. No.	Location ($''$)	RA(1950)	Dec(1950)	Dist. ($''$)	Fitted Flux (μJy)	Corr. Flux (μJy)
A2218(SE)	1	(-39 , 121)	$16^h35^m35.4^s$	$66°20^m48^s$	153	1144 ± 101	2094 ± 185
A2218(SE)	2	(128 , 99)	$16^h36^m3.3^s$	$66°20^m26^s$	221	917 ± 101	3618 ± 398
A2218(SE)	3	(-192 , 34)	$16^h35^m10.0^s$	$66°19^m21^s$	157	2623 ± 101	4971 ± 191
A2218(NE)	1	(-40 , 119)	$16^h35^m35.2^s$	$66°20^m46^s$	87	1604 ± 100	1962 ± 122
A2218(NE)	2	(127 , 97)	$16^h36^m3.1^s$	$66°20^m24^s$	189	1588 ± 100	4077 ± 257
A2218(NE)	3	(-192 , 35)	$16^h35^m10.0^s$	$66°19^m22^s$	143	2814 ± 100	4754 ± 169

Tab. 3.4: Source subtraction for all the clusters for which S–Z effects have been detected. Locations are given relative to nominal cluster centre. When, a point source's distance from the actual pointing centre (also given) is less than four arcminutes, its flux can be accurately corrected for the primary beam attenuation. Also, if a clear match to a source at 1.4 GHz is available, a range of spectral indices consistent with the RT 1–σ errors is computed. In a few cases, the sources were not modelled as point-like but as circular Gaussians; the 1–σ widths (HWHM $\equiv 1.4\sigma$) are noted as superscripts in the third column. Note that for some clusters, data has been taken in different RT aerial configurations (A1914, A1413, CL0016+16) or with different offset pointing centres (A2218, CL0016+16). In these cases, the source subtraction has been done for each configuration and pointing separately; the table, however, simply shows the average flux.

Cluster	Src. No.	Location ($''$)	RA(1950)	Dec(1950)	Dist. ($''$)	Fitted Flux (μJy)	Corr. Flux (μJy)	Flux,1.4GHz (mJy)	α_{min}	α_{max}
A611	1	(-30 , 23)	$7^h57^m40.8^s$	$36°11^m43^s$	39	230 ± 80	241 ± 84	1.40	0.62	0.92
A611	2	(0 , -430)	$7^h57^m43.4^s$	$36°4^m9^s$	431	167 ± 80		8.40		
A665	1a	(194 , 92)	$8^h26^m57.5^s$	$66°2^m41^s$	215	262 ± 55	940 ± 197	25.00	1.10	1.31
A665	1b	(180 , 71)	$8^h26^m55.1^s$	$66°2^m20^s$	193	198 ± 55	538 ± 149			
A665	2	(-202 , -20)	$8^h25^m52.3^s$	$66°0^m48^s$	204	430 ± 55	1333 ± 170	13.00	0.91	1.02
A665	3a	(-173 , 42)	$8^h25^m57.0^s$	$66°1^m51^s$	179	183 ± 55	424 ± 127	1.70	0.25	0.52
A665	3b	(-141 , 48)	$8^h26^m2.3^s$	$66°1^m57^s$	150	169 ± 55	301 ± 98			
A665	4	(362 , 216)	$8^h27^m25.1^s$	$66°4^m45^s$	422	253 ± 55		1.20		
A665	5	(66 , 390)	$8^h26^m36.5^s$	$66°7^m39^s$	396	241 ± 55		3.40		

continued on next page

continued from previous page

Cluster	Src. No.	Location (″)	RA(1950)	Dec(1950)	Dist. (″)	Fitted Flux (μJy)	Corr. Flux (μJy)	Flux,1.4GHz (mJy)	α_{min}	α_{max}
A665	6	(158 , -278)	$8^h26^m51.4^s$	$65°56^m30^s$	321	217 ± 55		1.20		
A697	1	(29 , -235)	$8^h39^m48.8^s$	$36°28^m38^s$	238	560 ± 85	2946 ± 447	34.50	0.98	1.11
A697	2	(-470 , 198)	$8^h39^m7.3^s$	$36°35^m52^s$	511	444 ± 85		55.60		
A697	3	(-211 , -142)	$8^h39^m28.8^s$	$36°30^m11^s$	256	176 ± 85		5.80		
A697	4	(448 , 10)	$8^h40^m23.6^s$	$36°32^m44^s$	448	101 ± 85		1.20		
A697	5	(-151 , -154)	$8^h39^m33.8^s$	$36°29^m59^s$	217	110 ± 85	409 ± 316			
A697	6	(-194 , -188)	$8^h39^m30.2^s$	$36°29^m25^s$	272	103 ± 85				
A773	1	(89 , 42)	$9^h14^m32.1^s$	$51°56^m51^s$	98	320 ± 55	412 ± 71	1.80	0.56	0.70
A773	2	(-411 , 85)	$9^h13^m37.9^s$	$51°57^m34^s$	421	127 ± 55		47.40		
A773	3	(33 , -31)	$9^h14^m26.0^s$	$51°55^m37^s$	46	170 ± 55	181 ± 58	0.90	0.56	0.84
A773	4	(-33 , 10)	$9^h14^m18.8^s$	$51°56^m19^s$	35	153 ± 55	159 ± 57			
A773	5	(-6 , -158)	$9^h14^m21.7^s$	$51°53^m30^s$	159	117 ± 55	225 ± 106			
A773	6	(54 , 84)	$9^h14^m28.3^s$	$51°57^m33^s$	100	170 ± 55	220 ± 71			
A773	7	(72 , -127)	$9^h14^m30.2^s$	$51°54^m1^s$	147	154 ± 55	268 ± 96			
A773	8	(-21 , 72)	$9^h14^m20.1^s$	$51°57^m21^s$	75	139 ± 55	162 ± 64			
A773	9	$(150 , -10)^{20''}$	$9^h14^m38.7^s$	$51°55^m58^s$	150	218 ± 55	390 ± 98			
A773	10	$(148 , -18)^{20''}$	$9^h14^m38.4^s$	$51°55^m50^s$	149	328 ± 55	581 ± 97			
A773	11	$(-82 , -55)^{20''}$	$9^h14^m13.5^s$	$51°55^m13^s$	100	265 ± 55	344 ± 71			
A773	12	$(-76 , -38)^{20''}$	$9^h14^m14.1^s$	$51°55^m30^s$	86	360 ± 55	438 ± 67			
A990	1	(216 , -86)	$10^h20^m56.6^s$	$49°22^m4^s$	233	551 ± 65	2648 ± 312	39.00	1.09	1.19
A1246	1	(-221 , 33)	$11^h21^m3.9^s$	$21°46^m10^s$	224	153 ± 130	637 ± 542	5.10	0.62	1.68
A1246	2	(169 , -184)	$11^h21^m31.9^s$	$21°42^m32^s$	251	235 ± 130		48.40		
A1246	3	(-24 , -9)	$11^h21^m18.0^s$	$21°45^m27^s$	27	2533 ± 130	2594 ± 133	24.00	0.92	0.96
A1413	1a	(-131 , 110)	$11^h52^m34.4^s$	$23°43^m0^s$	172	1294 ± 40	2791 ± 86	29.00	0.94	0.98

continued on next page

continued from previous page

Cluster	Src. No.	Location (″)	RA(1950)	Dec(1950)	Dist. (″)	Fitted Flux (μJy)	Corr. Flux (μJy)	Flux,1.4GHz (mJy)	α_{min}	α_{max}
A1413	1b	(-141 , 92)	$11^h52^m33.7^s$	$23°42^m42^s$	169	89 ± 40	187 ± 84			
A1413	2	(-46 , -26)	$11^h52^m40.6^s$	$23°40^m43^s$	54	547 ± 40	594 ± 43	1.30	0.30	0.36
A1413	3a	(0 , -9)	$11^h52^m44.0^s$	$23°41^m0^s$	10	267 ± 40	268 ± 40	2.70	0.60	0.90
A1413	3b	(10 , 14)	$11^h52^m44.7^s$	$23°41^m24^s$	17	80 ± 40	81 ± 40			
A1413	3c	(-14 , 4)	$11^h52^m42.9^s$	$23°41^m14^s$	16	69 ± 40	70 ± 40			
A1413	3d	(33 , 3)	$11^h52^m46.4^s$	$23°41^m13^s$	33	60 ± 40	62 ± 41			
A1413	4	(244 , -601)	$11^h53^m1.7^s$	$23°31^m8^s$	650	211 ± 40		47.10		
A1413	5	(32 , -277)	$11^h52^m46.3^s$	$23°36^m32^s$	280	132 ± 40		0.90		
A1413	6	(-6 , 220)	$11^h52^m43.5^s$	$23°44^m50^s$	220	117 ± 40	455 ± 156	1.50	0.38	0.68
A1413	7	(-14 , 299)	$11^h52^m42.9^s$	$23°46^m9^s$	299	82 ± 40				
A1413	8	(297 , 158)	$11^h53^m5.6^s$	$23°43^m48^s$	336	97 ± 40		1.30		
A1413	9	(-23 , -135)	$11^h52^m42.3^s$	$23°38^m54^s$	138	92 ± 40	150 ± 65	0.70	0.50	0.89
A1413	10	(-43 , 76)	$11^h52^m40.8^s$	$23°42^m26^s$	88	113 ± 40	138 ± 49	0.50	0.41	0.73
A1413	11a	(10 , 14)	$11^h52^m44.7^s$	$23°41^m24^s$	17	80 ± 40	81 ± 40		3.32	3.88
A1413	11b	(-15 , 4)	$11^h52^m42.8^s$	$23°41^m14^s$	16	69 ± 40	70 ± 40			
A1413	11c	(33 , 3)	$11^h52^m46.4^s$	$23°41^m13^s$	33	60 ± 40	62 ± 41			
A1423	1	(-60 , -16)	$11^h54^m42.3^s$	$33°53^m21^s$	63	429 ± 85	479 ± 95	8.30	1.13	1.30
A1423	2a	(-59 , -26)	$11^h54^m42.4^s$	$33°53^m11^s$	66	351 ± 85	395 ± 96	8.00	0.58	0.69
A1423	2b	(85 , -80)	$11^h54^m54.0^s$	$33°52^m17^s$	117	974 ± 85	1388 ± 121			
A1704	1	(-49 , 47)	$13^h12^m28.2^s$	$64°51^m15^s$	69	221 ± 55	251 ± 62	1.70	0.71	0.93
A1704	2	(174 , 199)	$13^h13^m3.3^s$	$64°53^m47^s$	264	209 ± 55		8.00		
A1722	1	(60 , 144)	$13^h18^m45.5^s$	$70°20^m2^s$	156	193 ± 70	361 ± 131	9.70	1.26	1.58
A1914	1	(-167 , -99)	$14^h23^m44.9^s$	$38°1^m17^s$	196	430 ± 65	1197 ± 181	1.70	0.09	0.22
A1914	2	(-99 , -83)	$14^h23^m50.6^s$	$38°1^m33^s$	131	221 ± 65	342 ± 101	1.50	0.51	0.77

continued on next page

continued from previous page

Cluster	Src. No.	Location (″)	RA(1950)	Dec(1950)	Dist. (″)	Fitted Flux (μJy)	Corr. Flux (μJy)	Flux,1.4GHz (mJy)	α_{min}	α_{max}
A1914	3	(-104 , -41)	$14^h23^m50.2^s$	$38°2^m15^s$	113	156 ± 65	217 ± 90	1.00	0.50	0.87
A1914	4	(16 , 757)	$14^h24^m0.5^s$	$38°15^m34^s$	757	189 ± 65		51.00		
A1914	5	(317 , 207)	$14^h24^m26.0^s$	$38°6^m24^s$	379	171 ± 65		0.30		
A1914	6	(395 , 85)	$14^h24^m32.5^s$	$38°4^m22^s$	404	236 ± 65				
A1914	7	(35 , -185)	$14^h24^m2.1^s$	$37°59^m51^s$	189	229 ± 65	593 ± 168			
A1914	8	(-108 , 200)	$14^h23^m49.9^s$	$38°6^m17^s$	228	194 ± 65	854 ± 286			
A1914	9	(-161 , 194)	$14^h23^m45.4^s$	$38°6^m11^s$	253	144 ± 65				
A1914	10	(-5 , 193)$^{30″}$	$14^h23^m58.6^s$	$38°6^m10^s$	193	370 ± 65	1001 ± 176			
A1914	11	(87 , -58)$^{30″}$	$14^h24^m6.5^s$	$38°1^m58^s$	105	335 ± 65	446 ± 86			
A1995	1	(-76 , 59)	$14^h51^m26.2^s$	$58°16^m4^s$	97	464 ± 80	593 ± 102	5.40	0.86	1.01
A1995	2	(31 , 26)	$14^h51^m39.9^s$	$58°15^m31^s$	40	684 ± 80	718 ± 84	8.90	1.01	1.11
A2111	1	(155 , -286)	$15^h37^m58.7^s$	$34°29^m52^s$	326	168 ± 65		14.00		
A2218	1a	(-39 , 119)	$16^h35^m35.4^s$	$66°20^m46^s$	126	1298 ± 35	1944 ± 52	8.10	0.40	0.47
A2218	1b	(-71 , 82)$^{30″}$	$16^h35^m30.0^s$	$66°20^m9^s$	109	162 ± 35	220 ± 48			
A2218	1c	(-13 , 184)$^{30″}$	$16^h35^m39.7^s$	$66°21^m51^s$	185	244 ± 35	599 ± 86			
A2218	1d	(-71 , 78)$^{20″}$	$16^h35^m30.0^s$	$66°20^m5^s$	106	90 ± 35	120 ± 47			
A2218	2a	(128 , 97)	$16^h36^m3.3^s$	$66°20^m24^s$	161	1657 ± 35	3225 ± 68	7.60	0.27	0.31
A2218	2b	(118 , 77)	$16^h36^m1.6^s$	$66°20^m4^s$	141	165 ± 35	274 ± 58			
A2218	2c	(135 , 111)	$16^h36^m4.4^s$	$66°20^m38^s$	175	152 ± 35	337 ± 78			
A2218	3a	(-192 , 34)	$16^h35^m10.0^s$	$66°19^m21^s$	196	1790 ± 35	5010 ± 98	2.40	-0.47	-0.40
A2218	3b	(-196 , 10)	$16^h35^m9.3^s$	$66°18^m57^s$	197	129 ± 35	367 ± 100			
A2218	3c	(-187 , 57)	$16^h35^m10.8^s$	$66°19^m44^s$	196	117 ± 35	329 ± 99			
A2218	3d	(-210 , 72)$^{20″}$	$16^h35^m7.0^s$	$66°19^m59^s$	223	138 ± 35	561 ± 142			
A2218	3e	(-167 , -42)$^{20″}$	$16^h35^m14.1^s$	$66°18^m4^s$	173	211 ± 35	462 ± 77			

continued on next page

continued from previous page

Cluster	Src. No.	Location (″)	RA(1950)	Dec(1950)	Dist. (″)	Fitted Flux (μJy)	Corr. Flux (μJy)	Flux,1.4GHz (mJy)	α_{min}	α_{max}
A2259	1	(-243 , -139)	$17^h17^m49.9^s$	$27°40^m50^s$	281	367 ± 60				
A2259	2	(119 , -134)	$17^h18^m17.3^s$	$27°40^m55^s$	180	328 ± 60	768 ± 140			
Zw1883	1	(-58 , 26)	$8^h39^m49.4^s$	$29°29^m14^s$	64	624 ± 75	699 ± 84	4.20	0.71	0.81
Zw1883	2a	(-6 , -31)	$8^h39^m53.4^s$	$29°28^m16^s$	33	2141 ± 75	2214 ± 78	25.20	0.85	0.91
Zw1883	2b	(168 , 10)	$8^h40^m6.8^s$	$29°28^m58^s$	168	451 ± 75	941 ± 156			
CL0016+16	1	(-122 , 29)	$0^h15^m49.9^s$	$16°10^m11^s$	126	224 ± 35	337 ± 53	0.71	0.25	0.39
CL0016+16	2	(-33 , -338)	$0^h15^m56.0^s$	$16°4^m3^s$	341	587 ± 35		267.00		
CL0016+16	3	(-159 , 157)$^{40''}$	$0^h15^m47.3^s$	$16°12^m19^s$	224	451 ± 35	1870 ± 145			
CL0016+16	4	(-20 , -111)$^{40''}$	$0^h15^m56.9^s$	$16°7^m50^s$	114	241 ± 35	337 ± 49			
MS1137+662	1	(1 , 33)	$11^h37^m34.8^s$	$66°25^m25^s$	33	408 ± 70	422 ± 72			
MS1137+662	2	(-149 ,-1229)	$11^h37^m10.0^s$	$66°4^m22^s$	1239	800 ± 70				
TEXOXL20	1a	(-122 , 80)	$2^h30^m13.3^s$	$30°10^m9^s$	147	882 ± 65	1532 ± 113	26.50	0.86	0.95
TEXOXL20	1b	(-109 , 185)	$2^h30^m14.3^s$	$30°11^m54^s$	215	436 ± 65	1576 ± 235			
TEXOXL20	2	(-79 , -142)	$2^h30^m16.6^s$	$30°6^m26^s$	164	452 ± 65	905 ± 130	5.50	0.70	0.83
TEXOXL20	3a	(-31 , 39)	$2^h30^m20.3^s$	$30°9^m28^s$	50	1866 ± 65	2007 ± 70	9.90	0.58	0.63
TEXOXL20	3b	(-19 , -44)	$2^h30^m21.2^s$	$30°8^m4^s$	49	346 ± 65	371 ± 70			
TEXOXL20	4	(41 , -2)	$2^h30^m25.9^s$	$30°8^m46^s$	41	866 ± 65	911 ± 68	8.70	0.92	0.98
TEXOXL20	5a	(56 , -108)	$2^h30^m27.1^s$	$30°7^m0^s$	123	1795 ± 65	2638 ± 96	6.20	0.26	0.31
TEXOXL20	5b	(73 , -106)	$2^h30^m28.4^s$	$30°7^m2^s$	130	333 ± 65	512 ± 100			
TEXOXL20	6a	(136 , 35)	$2^h30^m33.3^s$	$30°9^m24^s$	140	995 ± 65	1649 ± 108	33.50	1.14	1.24
TEXOXL20	6b	(151 , 22)	$2^h30^m34.4^s$	$30°9^m11^s$	153	195 ± 65	355 ± 118			
TEXOXL20	7	(238 , -67)	$2^h30^m41.1^s$	$30°7^m41^s$	248	178 ± 65		6.20		
TEXOXL21	1a	(-109 , 126)	$2^h30^m23.0^s$	$35°48^m23^s$	167	156 ± 70	322 ± 145	9.30	0.99	1.33
TEXOXL21	1b	(-109 , 56)	$2^h30^m23.0^s$	$35°47^m13^s$	123	216 ± 70	319 ± 103			

continued on next page

continued from previous page

Cluster	Src. No.	Location (″)	RA(1950)	Dec(1950)	Dist. (″)	Fitted Flux (μJy)	Corr. Flux (μJy)	Flux,1.4GHz (mJy)	α_{min}	α_{max}
TEXOXL21	2	(-57 , -86)	$2^h30^m27.3^s$	$35°44^m50^s$	105	288 ± 70	382 ± 93	15.70	1.48	1.68
TEXOXL21	3a	(6 , 85)	$2^h30^m32.6^s$	$35°47^m42^s$	85	992 ± 70	1201 ± 85	3.50	0.16	0.23
TEXOXL21	3b	(-8 , 82)	$2^h30^m31.3^s$	$35°47^m39^s$	82	846 ± 70	1013 ± 84			
TEXOXL21	4a	(43 , -39)	$2^h30^m35.6^s$	$35°45^m37^s$	59	260 ± 70	286 ± 77	2.60	0.38	0.52
TEXOXL21	4b	(59 , -32)	$2^h30^m36.9^s$	$35°45^m44^s$	68	552 ± 70	625 ± 79			
TEXOXL21	5	(52 , -113)	$2^h30^m36.3^s$	$35°44^m23^s$	125	71 ± 70	106 ± 105	4.10	1.25	3.34
TEXOXL21	6	(67 , 29)	$2^h30^m37.6^s$	$35°46^m46^s$	73	224 ± 70	259 ± 81	3.20	0.95	1.22

4. DISCUSSION

The source subtraction methods presented in this dissertation have allowed for the systematic analysis of Ryle Telescope data from thirty cluster candidates. Images of twenty significant S–Z decrements, compiled in Figure 4.1, have been revealed.

4.1 Combined Value of the S–Z Hubble Constant

Table 4.2 summarizes the measured scale factors $r_{50} = 1/\sqrt{h_{50}}$, as well as the corresponding H_0 estimates and angular distances, of the eight H_0 clusters. In addition, the central S–Z temperature decrement for each cluster, predicted from the X-ray fit, both with the assumption $H_0 = 50$ km s^{-1}Mpc^{-1} and with the correction obtained by fitting to the RT dat are computed there; these decrements can be directly compared to values obtained from other experiments, also listed in the table. There is good consistency, especially considering that most of the other experiments either do not include spectral/temporal uncertainties in source subtraction in their estimates, or do not attempt source subtraction at all [Carlstrom 1996].

Before combining the H_0 estimates, it is very important to clarify the possible systematic errors in this method, based on the comparison of X-ray and radio S–Z data. Earlier estimates of the Hubble constant from S–Z effect measurements appeared to fall in a "low range", from 40 to 60 km s^{-1}Mpc^{-1}, prompting much speculation as to what might cause such a systematic "underestimation" [Birkinshaw 1998]. A wild range of effects have been proposed: clumping of the intracluster gas; gravitational lensing of background sources [Loeb 1997]; asphericity of the gas geometry; cooling flows; and non-isothermality, possibly due to merger shocks [Roettiger 1997].

4.1.1 Intracluster gas clumping

Even in the most extreme cases of gas clumping, where half of the cluster volume contains $5/6$ of the gas, the H_0 value would be underestimated by only 15% [Maggi 1997]. However, X-ray imaging of nearby large-angular-scale clusters clearly exclude such a level of fractionation in intracluster gas [Fabian et al. 1994]. Indeed, initial simulations produce gas clumping that would lead to an underestimate of only 2% in H_0 [Grainge 1999].

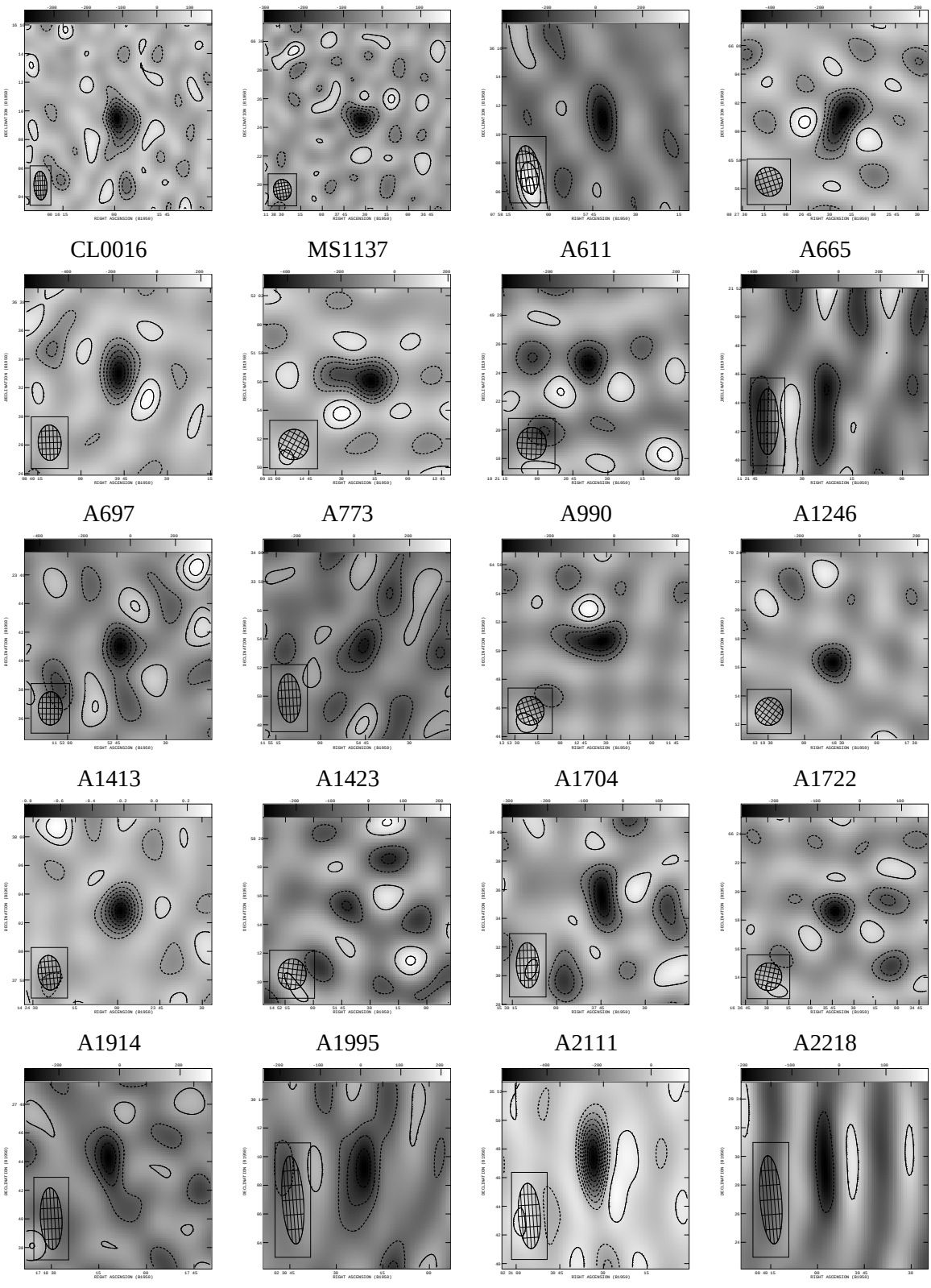

Fig. 4.1: A rogue's gallery of the cluster S–Z effects discussed in this dissertation.

4.1.2 Background radio sources

The effects of lensing of background radio sources by the cluster's gravitational potential have been calculated by Loeb and Refregier [Loeb 1997]. With a source-subtraction flux limit of $100\,\mu$Jy, this lensing effect leads to slight underestimate of H_0 of 1% in a typical massive cluster, like Abell 2218.

A stronger effect of these unsubtracted faint (microjansky) radio sources may be the confusion noise they induce on the RT shorter baselines. The source confusion noise was originally expected to be $50-70\,\mu\mathrm{Jy\,beam}^{-1}$ on 0–1 kλ baselines, negligible compared to the intrinsic statistical noise [Grainge 1996]; that estimate does not take into account the possible overabundance of faint sources near rich clusters. However, the scatter in the H_0 values obtained below appears consistent with ignoring source confusion noise.

4.1.3 Asphericity of gas geomety

Assumptions about the three-dimensional gas geometry are expected to induce an important error in estimates of H_0 based on individual clusters. In particular, the three-dimensional models of the gas density assume that the core radius along the line-of-sight is the geometric mean of the core radii transverse to the line-of-sight. For a cluster with true line-of-sight depth $l_\perp$ and assumed line-of-sight depth $l_\parallel$, the calculated value H_0^{calc} is found to be related to the true value H_0^{true} by

$$H_0^{\mathrm{calc}} = H_0^{\mathrm{true}} \frac{l_\perp}{l_\parallel}. \tag{4.1}$$

X-ray images show that the ratio of transverse core radii in this sample range from 1.1 (in the case of Abell 2218) up to 1.5 (in A1704). Assuming the actual line-of-sight depth could be any value between the two transverse diameters, this introduces an uncertainty of up to $\pm 25\%$ in H_0, with the sign depending on how the cluster's major axis is oriented relative to the line of sight. By averaging H_0's from a few clusters, with different orientations, the asphericity error is easily eliminated [Sulkanen 1999]. Since the eight clusters presented here were selected for their X-ray luminosities and temperatures (which are independent of cluster orientation), they form such an orientation-unbiased sample.

4.1.4 Intracluster gas temperature

Gas temperature uncertainties (which are usually of order 5–10%) produce a random error, of order 10–20% in H_0. In addition, there is a good possibility that using the X-ray-emission-weighted temperatures produces a systematic underestimate of H_0, for merging clusters (like Abell 2218, Abell 665, and Abell 1914) and cooling-flow clusters (like Abell 1413 and Abell 1704).

For recently merged clusters, both cluster merger simulations [Roettiger 1997] and ASCA observations of nearby hot clusters [Markevitch 1998] suggest the presence of hot regions of gas which are not in the cluster centre. Since the X-ray emission is proportional to n_e^2, an X-ray-emission-weighted temperature will tend to over-sample the centre of the cluster, producing a temperature estimate that

is lower than that appropriate for the S–Z effect. Simulations indicate that the H_0 values determined from merging clusters can be underestimated by as much as 30%, due to this temperature mismatch.[1]

For the cooling-flow (CF) clusters, a simultaneous analysis of the ROSAT HRI maps and ASCA spectra allows for the cluster temperature to be fitted with the colder contribution of the CF-region removed [Allen & Fabian 1998]; these higher temperatures have been used in the present H_0 analyses of Abell 1413 and Abell 1704. However, a comparison of the temperature vs. bolometric luminosity curves of CF and non-CF clusters, even after the correction to remove the cooling flows, indicates that the CF cluster temperatures still appear to be underestimated by 10–20%; see Figure 2 of [Allen & Fabian 1998]. The H_0 values estimated from these clusters may then be drastic underestimations, by 20–40%, of the true Hubble constant.

4.1.5 *Statistical/systematic error in ΔT_{SZ}*

The largest errors on measurements of H_0 from individual clusters are still due to the uncertainties in determining the depth of the cluster's S–Z shadow. In particular, seven of the eight clusters here have complex radio environments with positive, extended radio emission — possibly due to cluster-merger-halos, to gravitationally lensed radio sources, and to cooling-flow mini-halos — contaminating the S–Z effect. The separation of these clustre-centre halos from the S–Z effect generally increases (by as little as 10%, in CL0016+16, and by as much as 100%, in Abell 1914) the intrinsic error on the S–Z measurement due to statistical noise only.

4.1.6 *Other sources of error*

Other sources of error, including contamination from the kinetic S–Z effect, the existence of cold haloes, and the primary flux calibration of the Ryle Telescope have been shown to each produce less than 5% uncertainty in H_0, much less than the statistical error on the Ryle data; see, e.g., [Grainge 1999].

In summary, the largest errors in the individual cluster H_0 values derive from statistical uncertainties in measuring the S–Z hole depth; systematic uncertainties in removing contamination of the S–Z hole by extended cluster-centre radio sources; mismatch between the line-of-sight cluster depth and the observed cluster diameter; and the errors in the intracluster gas temperature taken from the emission-weighted X-ray spectra. These uncertainties are summarized for the eight H_0 clusters in Table 4.2. When H_0 estimates from this orientation-unbiased sample of clusters are combined, all of the uncertainties will be reduced, except for the temperature uncertainty, which is expected to cause a systematic underestimation of up to 30% in recently-merged clusters and cooling-flow clusters.

[1] ASCA measurements indicate that the temperature structure of *relaxed* clusters appear to follow a fairly universal smooth profile that slowly decreases with radius, when scaled to $r_{180} = 2.8 h_{70}^{-1}\mathrm{Mpc}\,(T_e/10\,\mathrm{keV})^{1/2}$. For numbers typical of the RT target clusters, $T_e = 7$keV and $z = 0.2$, the temperature drops to 80% of its maximum value at radii of about 2 arcmin [Markevitch 1998]. The X-ray-emission-weighted temperature for these clusters would then be expected to agree, to well within 5%, with the temperature appropriate for the S–Z effect. If the S–Z effect of these (generally cool) relaxed clusters can be detected, the resulting H_0 estimate would then be underestimated by less than 10% [Maggi 1997].

By combining the measured scale factor $1/\sqrt{h_{50}}$ for all the clusters, a value of $1/\sqrt{h_{50}} = 0.95 \pm 0.05$, corresponding to $H_0 = 56^{+7}_{-6}(\text{random errors only})\,\text{km s}^{-1}\text{Mpc}^{-1}$ is finally obtained. Taking into account the possible systematic effects of the gas temperature structure — which may produce an underestimate by as much as 30% in these rich clusters — the allowed range of H_0 increases to 56–$72\,\text{km s}^{-1}\text{Mpc}^{-1}$, with a random error of 11%.

The value agrees well with other S–Z/X-ray-based estimates, like the combined value of $H_0 = 47 \pm 7(\text{statistical})^{+19}_{-5}(\text{systematic})$, obtained in [Hughes & Birkinshaw 1998-2] by averaging over eight measurements from four S–Z experiments. In addition, the H_0 estimate obtained here is consistent with the values found with completely different methods, like the results from graviational lens time-delay measurements, $72 \pm 7(\text{statistical}) \pm 15\%(\text{systematic})\,\text{km s}^{-1}\text{Mpc}^{-1}$ [], and distance-ladder calibration in the HST Key Project, $72 \pm 5(\text{statistical}) \pm 7(\text{systematic})\,\text{km s}^{-1}\text{Mpc}^{-1}$; see, e.g, the review in [Freedman 1999]. It will be interesting to see how well these values converge to the "true" Hubble constant as their systematic errors are better understood, and the statistical error is reduced with future experiments.

In the above S–Z/X-ray based H_0 result, a value of the deceleration parameter $q_0 = 0.5$ is assumed for the deceleration parameter, which enters into the form of the angular-distance vs. redshift relation. However, for the redshifts $z < 1$ considered here, it turns out that changing q_0 has very little effect. On one hand, this fact explains why S–Z effect measurements cannot constrain q_0; on the other hand, it makes the measured value of H_0 quite robust to uncertainty in q_0. For example, if a different value $q_0 = 0$ is assumed, the central value of H_0 decreases by 5%, a very small perturbation indeed.

4.2 Searching for High-Redshift Clusters

In terms of future physical insights, the Sunyaev-Zeldovich effect may be most valuable in its ability to probe very distant, primal large-scale structure. In the last few years, the discoveries of high-z (proto)clusters, through S–Z detections in fields containing double-quasars [Jones et al. 1997], as well as through serendipitous detection of extended X-ray sources (see, e.g., [Rosati 1999]) have revealed the early ($z > 0.5$) universe to have a rich large-scale structure, which, in fact, implies an upper bound the universe's mass density of approximately $\Omega_m < 0.6$; see [Bahcall 1997]. Energized further by the discovery of the high-z clusters TEXOXL20 and TEXOXL21 presented here, the search for clusters correlated with aggregates of radio sources is continuing.

The S–Z shadows of the distant clusters CL0016+16 and MS1137+625 are also tantalizing. The remarkable structures in both of their 0–$2\,\text{k}\lambda$ RT maps [see Figure 3.26 and 3.23] with extensions leading away from the cluster centre may be evidence that the clusters are parts of superstructures. Such extensions are not visible on the low-sensitivity X-ray maps of either region, demonstrating that for high-z clusters, measurements of the distance-independent S–Z effect can provide images superior to X-ray observations.

Cluster	z	Scale Factor $(1/\sqrt{h_{50}})$	H_0, $\mathrm{km\,s^{-1}Mpc^{-1}}$	D_θ, Mpc	$\Delta T_{SZ}\, h_{50}^{-\frac{1}{2}}$, mK, X-rays	ΔT_{SZ}, mK,Ryle	ΔT_{SZ}, mK, others	
A665	0.182	$1.11 \pm 0.23 \pm 0.04$	41^{+25}_{-13}	1003^{+467}_{-378}	-1.00	-1.11 ± 0.23	-0.79 ± 0.13	[Birkinshaw 1998]
A697	0.282	$0.87 \pm 0.13 \pm 0.05$	66^{+27}_{-17}	827^{+285}_{-243}	-1.01	-0.88 ± 0.14		
A773	0.217	$0.89 \pm 0.20 \pm 0.04$	63^{+43}_{-21}	730^{+374}_{-297}	-0.91	-0.81 ± 0.19	-0.67 ± 0.09	[Carlstrom 1996]
A1413	0.143	$1.14 \pm 0.12 \pm 0.07$	38^{+11}_{-8}	882^{+228}_{-202}	-0.86	-0.98 ± 0.10		
A1704	0.220	$0.87 \pm 0.22 \pm 0.04$	66^{+54}_{-24}	704^{+409}_{-316}	-0.59	-0.51 ± 0.13	> -0.3	[Carlstrom 1996]
A1914	0.171	$0.84 \pm 0.21 \pm 0.06$	71^{+59}_{-26}	548^{+324}_{-249}	-1.64	-1.38 ± 0.36		
A2218	0.171	$0.81 \pm 0.18 \pm 0.02$	76^{+50}_{-25}	510^{+255}_{-203}	-0.70	-0.57 ± 0.13	-3.2 ± 1.2	[Klein 1991]
							-0.88 ± 0.26	[Uyaniker 1997]
							-0.62 ± 0.08	[Birkinshaw 1998]
							-0.68 ± 0.19	[Tsuboi 1998]
CL0016	0.546	$0.94 \pm 0.05 \pm 0.08$	57^{+13}_{-10}	1342^{+285}_{-258}	-1.16	-1.09 ± 0.11	-0.72 ± 0.07	[Carlstrom 1996]
							-1.48 ± 0.24	[Birkinshaw 1998]

Tab. 4.1: Summary of Hubble Constant determination. The scale factors and Hubble constants are computed for $q_0 = 0.5$; for the relevant redshifts, however, the H_0 values are insensitive at the level of 5% to changes in the deceleration parameter [see text]. The first error on the scale factor $1/\sqrt{h_{50}}$ is due to uncertainty in measuring the S–Z hole depth; the second error is due to the uncertainty in the X-ray-measured gas temperature. The angular distances D_θ are independent of q_0. To calculate central CMB temperature decrements due to the S–Z effect, an X-ray constrained gas model is used. Measurements from other experiments are compiled in [Birkinshaw 1998]; the conversions of individual experimental results to a central ΔT_{SZ} are done in [Birkinshaw 1998] and [Carlstrom 1996].

5. CONCLUSIONS

A newly developed method which systematically fits and removes point-like radio sources in visibility data has been applied to galaxy cluster observations by the Ryle Telescope, resulting in the images of twenty S–Z shadows at 15 GHz.

While the spectra and normalized flux distributions of these radio sources are similar to those in non-cluster regions, there appears to be a strong overabundance (by a factor of 4 to 6) of sources in the rich-cluster regions compared to non-cluster regions, requiring extra care in removing these point sources from S–Z maps. c

In addition, the RT observations, as well as lower-frequency radio maps, indicate that the central regions of hot clusters contain *extended* radio flux — possibly due to gravitationally lensed radio rings, merger-induced radio halos, and/or cooling-flow "mini-halos" — which contaminate the S–Z shadow. A method to separate these extended "radio halo" sources from scaled models of the S–Z effect, based on X–ray information, has been developed and applied to eight clusters. Uncertainties in the halo/hole separation can increase the error by up to a factor of two on the measurement of ΔT_{SZ}. In particular, the existence of such a (previously ignored) "halo" source in S–Z measurements of cluster Abell 2218 dominates the error on the detection.

Combining X-ray and S–Z images of eight clusters allows for a measurement of the Hubble constant. The allowed range of H_0 is 56–72 $\mathrm{km\,s^{-1}Mpc^{-1}}$, with a random error of 11%. The dominant source of error on this combined value is not the statistical uncertainty in the S–Z measurements, but instead the poorly understood large-scale temperature gradients in these hot, dynamic clusters. Spatially resolved X-ray spectral measurements by the new satellites XMM and Chandra AXAF should allow this particular systematic error to be significantly reduced in the near future. In addition, next-generation S–Z telescopes may be able to obtain images of cooler, relaxed clusters which are less likely to have the strong temperature gradients — or, for that matter, "halo" sources or aspherical gas profiles — that currently limit the accuracy of the S–Z/X-ray-based determination of H_0 to the 30% level.

Four of the S–Z detections presented here are for clusters at redshift greater than 0.3. Two of them, TEXOXL20 and TEXOXL21, have been targeted by looking for aggregates of radio sources, and thus provide a good challenge for the new source-subtraction techniques. The RT data reveals the presence of strong S–Z effects in both regions, after point source subtraction; deep optical images and spectra are now being obtained to constrain these clusters' redshifts. Finally, S–Z maps of two more X-ray-selected high-z clusters, CL0016+16 (at $z = 0.55$) and MS1137+6625 (at $z = 0.78$) appear to

show extended structure that is not visible on the low-sensitivity X-ray maps. Further S–Z imaging may reveal additional super-structure around these distant, rich clusters.

6. ACKNOWLEDGMENTS

My stay at Cambridge University has been supported through a British Marshall scholarship. I would like to thank Garret Cotter, Will Grainger, Mike Jones, Ruediger Kneissl, Guy Pooley, and especially Keith Grainge for the RT/X-ray data and for the discussions and tutorials which guided me through my first year of AIPS, of Sunyaev–Zel'dovich imaging, and, indeed, of astrophysics/cosmology. Most of all, I thank Richard Saunders, whose boundless energy, whose continuous availability, and whose creative ideas have made him a superb supervisor; from him, I have gained many valuable insights into the intricacies of radio astronomy, and of radio astronomers.

BIBLIOGRAPHY

[AbdelSalam 1998] AbdelSalam, H., Saha, P., & Williams, L., AJ, **116**, 1541, 1998.

[Abell 1989] Abell, G.O., Corwin, H.G., & Olowin, R.P., ApJ suppl., **70**,1,1989.

[AIPS 1999] Full documentation & installation notes for AIPS are available on-line at http://www.cv.nrao.edu/aips/.

[Alex&er 1984] Alexander, P. & Leahy, P., MNRAS, **225**, 1, 1984.

[Allen & Fabian 1998] Allen, S. W., Fabian, A. C., 1998, MNRAS, **297**, L57.

[Bahcall 1997] Bahcall, N., Fan, X., & Cen, R., ApJL, **485**, L53, 1997.

[Birkinshaw 1984] Birkinshaw, M., Gull, S., & Hardebeck, H., Nature, **309**, 34, 1984.

[Birkinshaw 1998] Birkinshaw, M., Phys. Rept., **310**,97, 1999.

[Birkinshaw & Hughes 1994] Birkinshaw, M. & Hughes, J., ApJ, **420**, 33, 1994.

[Boynton 1982] Boynton, P., Radford, S., Schommer, R., & Murray, S., ApJ, **257**, 473, 1982.

[Burns 1990] Burns, J., ApJ, **99**, 14, 1990.

[Burns 1992] Burns, J. O., Sulkanen, M.E., Gisler, G.R., & Perley, R.A., et al., Ap J, **388**,L49, 1992.

[Carlstrom 1996] Carlstrom, J.E., Joy, M. & Grego, L., ApJ, **456**, L75, 1996.

[Carlstrom 1999] Carlstrom *et al.*, "Imaging the Sunyaev-Zel'dovich Effect", Proceedings of the Nobel Symposium "Particle Physics & the Universe", Physica Scripta & World Scientific, eds. Bergrstom, Carlson, & Fransson; see astro-ph/9905255.

[Cavaliere 1979] Cavaliere, A., Danese, L., DeZotti, G., A&A, **75**, 322,1979.

[Clusters 1994] "Clusters of Galaxies", ed. Duret, F., Mazure, A., & Tran Thanh Van, J., Proceedings of the XXIXth Rencontre de Moriond, 1994. In particular, see articles by Gavazzi and by Thomas *et al.*.

[Condon 1990] Condon, J., Dickey, J., & Salpeter, E., AJ, **99**, 1071, 1996.

[Condon 1998] Condon, J. J., Cotton, W. D., Greisen, E. W., Yin, Q. F., Perley, R. A., Taylor, G. B., & Broderick, J. J., AJ, 115, 1693, 1998; VLA NVSS catalogue is searchable on-line at *http://www.cv.nrao.edu/NVSS/*.

[Cooray 1998] Cooray, A., Grego, L., Holzapfel, W., Joy, M., & Carlstrom, J., AJ, **115**, 1388, 1988.

[Cress 1996] Cress, C., Helfand, M., Becker, R., Gregg, M., & White, R., ApJ, **473**, 7, 1996.

[Deiss 1997] Deiss, B., Reich, W., Lesch, H., Wielebinski, R., A&A, **321**, 55, 1997.

[Donahue 1999] Donahue, et al., to appear in ApJ; see astro-ph/990625.

[Donnelly 1987] Donnelly, R., Partridge, R., & Windhorst, R., ApJ, **321**,94, 1987.

[Fabian 1994] Fabian, A.C.,*Annu. Rev. Astron. Astrophys.* **32**, 277, 1994.

[Fabian et al. 1994] Fabian, A.C., Crawford, C.S., Edge, A.C., & Mushotzsky, R.F., 1994, MNRAS, **267**, 779, 1994.

[Freedman 1999] Freedman, W.,"Determination of Cosmological Parameters", Proceedings of the Nobel Symposium "Particle Physics & the Universe", Physica Scripta & World Scientific, eds. Bergrstom, Carlson, & Fransson; see astro-ph/9905222.

[Giovannini 1999] Giovannini, G., Tordi, M., & Feretti, L., New A., **4**, 141; astro-ph/9904210.

[Girardi 1997] Girardi, M., Fadda, D., Escalera, E., Giuricin, G., Mardirossian, F & Mezzetti, M, ApJ, **490**, 56, 1997.

[Grainge 1996] Grainge, K., "Measuring the Hubble Constant via the Sunyaev–Zel'dovich Effect", Cambridge Ph.D. Thesis, 1996.

[Grainge 1999] Grainge, K., Jones, M.E., Pooley, G., Saunders, R., Edge, A., Kneissl, R., submitted to MNRAS, 1999; see astro-ph/9904165.

[Hughes & Birkinshaw 1998-1] Hughes, J., & Birkinshaw, M., ApJ, **497**, 645, 1998.

[Hughes & Birkinshaw 1998-2] Hughes, J. & Birkinshaw, M., ApJ, 501, 1, 1998.

[Jones 1990] Jones, M., Ph. D. thesis, Cambridge University, Aperture Synthesis Observations of the S-Z Effect, 1990.

[Jones 1995] Jones, M.,*Astro. Lett. & Comms.* 32, 347, 1995.

[Jones 1993] Jones, M. *et al.*, Nature, 365, 320, 1993.

[Jones et al. 1997] Jones, M., Saunders, R., Baker, J., Cotter, G., Edge, A., Grainge, K., Haynes, T., Lasenby, A., Pooley, G., & Roettgering, H., ApJL, 479, L1.

[Jones & Forman 1984] Jones, C. & Forman,W., 1984, ApJ, 276, 38.

[Klein 1991] Klein, U., Rephaeli, Y., Schlickeiser, R. & Wielebinski, R., A&A, 244, 43, 1991.

[Kneissl 1999] Kneissl, R., private communication, 1999.

[Lefebvre 1994] Lefebvre, D. C., "Microwave Background Anisotropies from Clusters of Galaxies", Cambridge Ph.D. Thesis,1994.

[Loeb 1997] Refregier, A. & Loeb, A., 1997, Ap J, 478, 476.

[Maggi 1997] Maggi, A., "Constraining the Hubble Constant via the Sunyaev–Zel'dovich Route", Cambridge Part III Thesis, 1997; see also Jones, M., Saunders, R., Grainge, K., Grainger, W., & Maggi, A., Amer. Astro. Soc. Meeting 194, 58.05.

[Margon 1983] Margon, B., Downs, R., & Spinrad, H., Nature, 301, 221, 1983.

[Markevitch 1996] Markevitch, M.,ApJL, 465, 1, 1996.

[Markevitch 1997] Markevitch, M., ApJLett 483, L17, 1997.

[Markevitch 1998] Markevitch, M., Forman, W. R., Sarazin, C.L. & Vikhlinin, A., ApJ, 1998, 503, 77.

[Minnesota 1988] "The Minnesota Lectures on Clusters of Galaxies & Large Scale Structure", ed. Dickey, J., Astronomical Society of the Pacific, 1988.

[Miyoshi 1999] Miyoshi, S., private communication, 1999.

[Moffet & Birkinshaw 1989] Moffet, A.T. & Birkinshaw, M., AJ, 98,1148,1989.

[Num. Recipes 1992] Press, W.H., et al., "Numerical Recipes in Fortran" CUP, 2nd ed., 1992.

[Ostrander 1998] Ostrander, E.J., Nichol, R.C., Ratnatunga, L.U., & Griffiths, R.E., AJ, 116,2644,1998.

[Pacholczyk 1977] Pacholczyk, A.G., "Radio Galaxies", Pergamon Press, 1977.

[Partridge 1987] Partridge, R.B., Perley, R.A., Mandolesi, N., & Delpino, F., ApJ, 317, 112, 1987.

[Pooley 1999] Pooley, G., private communication, 1999.

[Rawlings 1999] Rawlings, S., private communication, 1999.

[Rengelink 1997] Rengelink, R., Tang, Y., de Bruyn, A., Miley, G., Bremer, M., Roettgering, H., Bremer, M., A&A Suppl. Ser.,124, 259, 1997; WENSS catalogue is searchable on-line at *http://www.strw.LeidenUniv.nl/%7Edpf/wenss/*.

[Roettiger 1997] Roettiger K., Stone, J.M. & Mushotzky, R.F., Ap J, 482,588, 1997.

[Rosati 1999] Rosati, P., Stanford, S., Eisenhardt, P., Elstron, R., Spinrad, H., Stern, D., & Dey, A., AJ, 118, 76, 1999.

[Ryle 1972] Ryle, M, Nature, 239, 435, 1972.

[Sarazin 1986] Sarazin, C. L., Rev. Mod. Phys., 58,1, 1986.

[Saunders 1999] Saunders, R., Kneissl, R., Grainge, K., Jones M., Maggi, A., Das, R., Edge, A., Lasenby, A., Pooley, G., Miyoshi, S., Tsuruta, T., Yamashita, K., Tawara, Y., Furuzawa, A., Harada, A., Hatsukade, I. submitted to MNRAS, 1999; see astro-ph/9904168.

[Sulkanen 1999] Sulkanen, M., ApJ, 522, 59, 1999.

[Sunyaev & Zel'dovich 1972] Sunyaev, R.A. & Zel'dovich, Ya. B., Comm. Astrophys. Sp. Phys., 173, 1972.

[Thomson 1986] Thomson, A.R., Moran, J.M., Swenson, G.W., Malabar, Florida, Kreiger Publishing Company, Interferometry & Synthesis in Radio Astronomy, 1986.

[Tribble 1993] Tribble, P.C., MNRAS, 263,31, 1993.

[Tsuboi 1998] Tsubio, M., Miyazaki, A., Kasuga, T., Matsuo, H. & Kuno, N., PASJ, 50, 169, 1998.

[Turner & Tyson 1999] Turner, M.S. & Tyson, J.A., Rev. Mod. Phys., 71, 145, 1999.

[Uson 1984] Uson, J.M. & Wilkinson, D.T., ApJ, L1, 277,1984.

[Uyaniker 1997] Uyaniker, B., Reich, W., Schlickeiser, R., Wielebinski, R., A&A, 325, 516, 1997.

[Weinberg 1972] Weinberg, S., "Gravitation & Cosmology", John Wiley & Sons, New York, 1972.

[White 1993] White, S.D.M., Navarro, J.F., Evrard, A.E. & Frenk, C.S., Nature, 366, 429, 1993.

[White 1997] White, R. L., Becker, R. H., Helfand, D. J., & Gregg, M. D., ApJ, 475, 479, 1997; VLA FIRST catalogue is searchable on-line at *http://sundog.stsci.edu/*.

[Windhorst 1993] Windhorst, R., Fomalont, E., Partridge, R., & Lowenthal, J, ApJ, 405, 498, 1993.

[Zwicky 1961] Zwicky, F., Herzog, E., Wild, P., & Karpowicz, M. & Kowal, C.T., Pasadena, Caltech, Catalogues of Galaxies & Clusters of Galaxies, 1961.